DEPARTMENT OF INFORMATICS

TECHNISCHE UNIVERSITÄT MÜNCHEN

Bachelor's Thesis in Informatics: Games Engineering

Implementation and Characterization of Commercial off-the-shelf Sensors for the Attitude Determination System of the MOVE-III CubeSat

Natalia Piotrowski

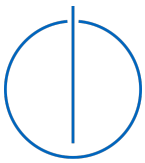

DEPARTMENT OF INFORMATICS

TECHNISCHE UNIVERSITÄT MÜNCHEN

Bachelor's Thesis in Informatics: Games Engineering

Implementation and Characterization of Commercial off-the-shelf Sensors for the Attitude Determination System of the MOVE-III CubeSat

Implementierung und Charaktierisierung von Commercial off-the-shelf Sensoren für das Lagebestimmungssystem des MOVE-III CubeSats

Author:	Natalia Piotrowski
Supervisor:	Prof. Gudrun Klinker
Advisor:	M.Sc. David Meßmann and M.Sc. Sandro Weber
Submission Date:	15.02.2022

I confirm that this bachelor's thesis in informatics: games engineering is my own work and I have documented all sources and material used.

Munich, 15.02.2022 Natalia Piotrowski

Acknowledgments

I would like to thank my two advisors, David Meßmann, and Sandro Weber. Both helped me on both the technical as well as the organizational side and were always quick to support me once an issue arose. I appreciate the time they put into meeting with me as well as giving me hints in case I got stuck.

Next, I would also like to thank the MOVE team for showing me the fascination behind developing a satellite, which started this work. I am thankful for everything I have learned from everyone in this amazing project.

I would then also like to thank every one of my friends, that took their time out of the day to both listen to issues regarding my thesis as well as proofreading this document.

I also want to thank my mother for supporting me throughout the months leading up to this work. She has been an incredible source of support and motivation, for which I am extremely thankful. This thesis would not have been possible without her.

Abstract

This thesis determines a suitable Inertial Measurement Unit (IMU) for the Attitude Determination and Control System (ADCS) for the third satellite of the Munich Orbital Verification Experiment (MOVE).

The thesis first explains the requirements and constraints for an IMU. In the context of this work, three IMUs, the BNO055, ICM20948 and LSM9DS1, the LIS3MDL magnetometer, and the BMI088 gyroscope are selected and analyzed.

The sensors are implemented using the DOSIS software platform and analyzed using MATLAB. The simulation was implemented using Simulink.

The error coefficients of each sensor measurement are initially calculated through the Allan variance. These are then verified through Welch's power spectral density estimate, simulations, and additional sensor measurements. This estimate is calculated using the pwelch method implemented by Mathworks. The BNO055 was also flown on a high altitude balloon, as well as submitted to a Thermal Vacuum Chamber (TVAC) test. These experiments are then evaluated, and further temperature experiments are performed to characterize the behavior of the sensor in changing temperatures. Finally, two calibration methods, magcal developed by Matlab and the TWOSTEP algorithm, are analyzed through simulated data.

The evaluation of the most accurate error coefficients found the BNO055 gyroscope to be the least affected by the white noise compared to the remaining gyroscopes. Among the magnetometers, the LSM9DS1 appears to be the sensor least influenced by the most accurate random walk and white noise term.

The temperature experiments determined the BMI088 gyroscope as the sensor least influenced by temperature drift. Among the magnetometers, the BNO055 is the least affected by temperature changes, while the BMI088 appears the most stable amongst the gyroscopes.

This concluded that as an overall sensor, the BNO055 IMU is recommended to the ADCS.

Kurzfassung

Diese Arbeit beschäftigt sich mit der Auswahl eines geeigneten IMUs für die Lagebestimmung des dritten Satelliten des MOVE Projektes.

Die Anforderungen an diesen Sensor werden beschrieben, bevor die drei IMUs BNO055, LSM9DS1 und ICM20948 selektiert werden. Zusätzlich wird auch der Magnetometer LIS3MDL sowie das Gyroskop des BMI088 zum Abgleich charakterisiert.

Die Sensoren wurden mittels der Software platform DOSIS implementiert, während die Charakterisierung mittels MATLAB erfolgte. Simulink wurde für Simulationen benutzt.

Die Bestimmung der Fehlerwerte der Sensoren erfolgt mittels der Allan Variance. Die Verifikation dieser erfolgte mittels der Welch's Methode, Simulationen sowie zusätzliche Sensormessungen. Der BNO055 wurde zudem auf einem Stratospärenballon geflogen, sowie einem TVAC Test unterzogen. Es wurden weitere Temperaturexperimete für alle Sensoren durchgeführt und ausgewertet.Zudem wurden die zwei Kalibrierungsmethoden magcal von MATLAB sowie TWOSTEP mithilfe von simulierten Daten analysiert.

Die Auswertung der Experimente führt zu der Beobachtung, dass das unter den Gyroskopen der BNO055 am wenigsten vom weißen Rauschen beeinflusst ist. Unter den Magnetometern ist der LSM9DS1 am wenigsten vom random walk und weißen Rauschen beeinflusst.

Die Temperaturergebnisse ergaben, dass alle drei Achsen des BMI088 Gyroskopes am wenigsten von Temperaturänderungen beeinflusst wird. Unter den Magnetometern besitzt der BNO055 den geringsten temperaturebedingten Drift, während der BMI088 den geringsten Drift unter den Gyroskopen aufwies.

Die oben beschriebenen Experimente führten zur einer Empfehlung des BNO055 als geeigneter Sensor für die Lagebestimmung.

Glossary

ADCS Attitude Determination and Control System. iv, 2–4, 23, 124, 126–128

CVG Coriolis Vibrating Gyros. 6

DLR Deutsches Zentrum für Luft- und Raumfahrt. 3

DOSIS Distributed Operating System Initiative for Satellites. 4, 5, 18, 116

I^2C Inter-integrated circuit. 18, 30

IMU Inertial Measurement Unit. iv, v, 13, 18, 23, 28, 29, 124

ISS International Space Station. 1

LEO Low Earth Orbit. 1

MEMS Micro-Electro-Mechanical Systems. 5, 6

MOVE Munich Orbital Verification Experiment. iv, v, 1–5, 29, 124, 126

PSD Power Spectral Density. viii, ix, 9–11, 13, 19, 21, 40–46, 55–61, 65–68, 72–75, 79–82, 104, 129–132

RODOS Real time Onboard Dependable Operating System. 4

SVD Single Value Decomposition. 17

TUM Technical University of Munich. 1

TVAC Thermal Vacuum Chamber. iv, v, 21, 82–84, 124, 132

WARR Scientific Workgroup for Rocketry and Spaceflight. 1

Nomenclature

$\bar{\mu}_k$	Auxilary variable for the centered solution of the noise term
$\bar{L}_k$	Auxilary variable for the centered solution of the auxilary variable
$\bar{z}_k$	Auxilary variable for the centered solution of the effective measurements
ϵ_k	Noise vector
η_i	Stop condition for algorithm
μ_k	Mean of the noise term
$\Omega(t)$	Output rate of the sensor
$\overline{\Omega}_k(T)$	Average of the output rate per cluster
$\overline{\Omega}_{next}(T)$	Average of the output rate of the subsequent cluster
$\phi(\theta')$	Auxilary 7-element vector variable
$\sigma^2(T)$	Allan variance
σ^2	Variance of the error
$\theta(t)$	Integration over the output rate of the sensor
θ	Estimation vector
$\widetilde{\mu}_k$	Centered solution for the mean of the noise term
$\widetilde{\theta}'$	Centered solution for the estimation vector
$\widetilde{F}_{\theta',\theta'}$	Centered Fischer information matrix
$\widetilde{P}_{\theta',\theta'}$	Covariance matrix
$\widetilde{P}^{-1}_{\theta',\theta'}$	Centered solution for the covariance matrix
$\widetilde{z}_k$	Centered solution for the effective measurements

A_k^{true}	Unknown attitude matrix
B	Error coefficient of the flicker noise calculated by the allan variance
b	Bias vector for the magcal measurement model
b^{true}	Bias of the magnetometer measurements
B_k	Magnetometer measurements at time t_k
c	Auxilary 3x1 vector variable
C_i	Cosine-integrated function
D	Symmetric 3x3 matrix
D^{true}	Scale factor matrix
E	Auxilary 3x3 matrix variable
$F[\cdot]$	Fourier transform
$f_{i=1:n\_nf}$	frequencies at which overall Power Spectral Density (PSD) slope is close to -3
$f_{i=1:n\_qn}$	frequencies at which overall PSD levels
$f_{i=1:n\_rw}$	frequencies at which overall PSD slope is close to -4
$f_{i=1:n\_wn}$	frequencies at which overall PSD slope is close to -2
h	Bias vector for the TWOSTEP measurement model
I_3	Identity matrix $3x3$
L_k	Auxilary variable
m_k	Magnetic field vector
N	Number of datapoints for the allan variance
n	Number of consecutive datapoints for the allan variance
O	Unknown orthogonal matrix
Q	Error coefficient of the white noise calculated by the allan variance
Q_z	Error coefficient of the quantization noise calculated by the allan variance

R 3x3 matrix

R Error coefficient of the random walk calculated by the allan variance

R_k Magnetic field strength vector

$R_{xx}(\tau)$ Autocorrelation of process x

S Auxilary matrix variable

S_k Auxillary variable

$S_\Omega(f)$ PSD for the random process $\Omega(f)$

$S_x(jw)$ Power spectral density of process x

T Cluster time for the allan variance

U Auxilary matrix variable

v Auxilary variable

W Diagonal matrix

x Recorded magnetometer data

X_{isolFN} PSD estimate of isolated flicker noise

X_{isolQN} PSD estimate of isolated quantization noise

X_{isolRW} PSD estimate of isolated random walk

X_{isolWN} PSD estimate of isolated white noise

$X_{totalnoise}$ PSD estimate of the total noise

y_k Recorded Magnetometer measurements

z_k Effective sensor measurements

Contents

1 Introduction

On the 15th of November 2021, Russia carried out an anti-satellite test by destroying one of their satellites in-orbit, which caused over 1,500 new particles to orbit the Earth [Val21]. This endangered other spacecraft, such as satellites and the International Space Station (ISS) orbiting the Earth and added to the existing problem of space debris [Val21].

Over 60 years before, the Soviet Union launched Sputnik I, the world's first artificial satellite, into orbit, beginning the space race [NASb]. Since then, a multitude of satellites has been launched into orbit, resulting in over 4,550 operational satellites as of September 2021 [Con]. Many uncontrollable satellites and other discarded debris can be found orbiting the Earth alongside the operational spacecraft [Che11].

Tracking these particles is essential as their kinetic energy can cause substantial damage to a functional spacecraft [NASa]. Ground stations can usually track debris larger than 1 cm, which is impossible for smaller particles [GKL12]. Nonetheless, impacts with submillimeter debris can also lead to substantial damage to any spacecraft [GKL12].

A solution to the lack of tracking ability can be tracking through the usage of satellites.

1.1 Munich Orbital Verification Experiment (MOVE)

The Munich Orbital Verification Experiment (MOVE) is a student project and the satellite division of the Scientific Workgroup for Rocketry and Spaceflight (WARR) at the Technical University of Munich (TUM), which aims to provide students with hands-on experience in the space industry through the development of CubeSats. A CubeSat is a satellite consisting of several standardized cubes, which each have an edge length of 10 cm. One standardized cube is referred to as 1U [Vil+19].

After the successful launches of the 1U MOVE-II and MOVE-IIb cube satellites in 2018 [Rüc+19], the project aims to develop the 6U CubeSat MOVE-III. The scientific mission of this new satellite is to detect and analyze sub-millimeter space debris in Low Earth Orbit (LEO).

To accurately determine the detected debris's position, the CubeSat's overall attitude determination is crucial to the mission success and is here required to provide the attitude with $< 1^\circ$ accuracy.

1.2 The Attitude Determination and Control System (ADCS)

The ADCS is one of the vital systems of a satellite [Bol+12]. Its goal is to determine the attitude of the satellite through its sensors as well as actively change it through actuators [MC14].

Because an accurate attitude determination is crucial for possible scientific missions and precise control, multiple sensors get used.

A limited selection of sensors is listed below [MC14].

- **Gyroscopes**: measure the angular velocity
- **Magnetometers**: measure the magnetic field vector
- **Sun Sensors**: measure incoming sunlight and can be used to determine the sun position relative to the spacecraft
- **Star tracker**: compute the attitude of the spacecraft based on star positions

The accurate selection and implementation of these sensors are crucial for a useful attitude determination. As testing in the natural space environment before launch is impossible, simulations following a thorough characterization of all used sensors and actuators are crucial for testing the ADCS before launch.

A limited selection of actuators is listed below [MC14].

- **Reaction Wheels**: consists of a flywheel that can store rotational energy
- **Magnetic Torquers**: control a spacecraft by generating a magnetic dipole

1.3 Similar Mission Concepts

Two CubeSat mission concepts with a similar scientific mission as MOVE-III give an overview of similar missions and their ADCS.

1.3.1 AsteroidFinder

AsteroidFinder, a standard satellite bus developed by the Deutsches Zentrum für Luft- und Raumfahrt (DLR), aims to detect and identify inner Earth objects using a telescope. A star tracker and four gyroscopes were chosen to perform accurate attitude determination [Hei+09].

These are integrated into the attitude determination algorithm to define the respective deviations. For the star tracker, they observed a deviation of 9 arcsec. The gyroscopes have a deviation of 8.6 $''/s$ or $4.2 \cdot 10^{-5}$ rad/s [Hei+09]. Further simulations then prove the sufficient accuracy for the AsteroidFinder mission [Hei+09].

1.3.2 Armadillo

Students of the University of Texas developed the 3U CubeSat ARMADILLO, launched in 2019 [Dir]. Similar to MOVE-III, its scientific mission is to detect and characterize sub-millimeter dust particles. Its selected sensors are two Sinclair Interplanetary digital 2-axis sun-sensors, the Honeywell HMR2300 magnetometer, and an unquantified number of gyroscopes from Analog Devices [Dir]. Concrete analysis of these sensors and the overall performance of the ADCS could not be found.

1.4 Goal of this Thesis

First, this thesis introduces possible sensors for the ADCS of the MOVE-III CubeSat. The selected sensors are then implemented and later characterized through various experiments.

This characterization ensures that the best possible option of the considered sensors is recommended for the ADCS.

Additionally, two simulation approaches are used to prepare the sensors for later integration into an overall simulation of the whole ADCS.

Then, possible calibration methods are discussed. These could be used for further analysis of the sensors.

Finally, this thesis concludes with a recommendation on the sensor which should be used for the ADCS of the MOVE-III CubeSat.

2 Theoretical Background

2.1 Frameworks

2.1.1 Distributed Operating System Initiative for Satellites (DOSIS)

The software implementation team of the MOVE-III project uses the software platform Distributed Operating System Initiative for Satellites (DOSIS), based on the Real time Onboard Dependable Operating System (RODOS) [MD09] and is responsible for the development of DOSIS which is used by all other subteams within the MOVE-III project.

DOSIS offers two components: drivers for abstracting hardware and daemons for abstracting logic [Rüc+21]. To access registers from a sensor, a DOSIS driver must be operated by a DOSIS daemon. The hardware abstraction layer offered by RODOS handles the actual hardware access.

The microcontroller used by the MOVE-III team is the STM32L4-microcontroller [20b]. The Nucleo development boards from STMicroelectronics [20a] are used throughout this thesis.

2.1.2 MATLAB and Simulink

MATLAB [MAT21] and Simulink [Mata] is often used for simulation purposes. As a spacecraft cannot be tested in a space environment before the actual launch, these simulations ensure that the spacecraft stays nominal after deployment. Simulations are especially significant for the ADCS, which is directly dependent on the spacecraft's environment.

Algorithms for attitude determination and control are therefore heavily reliant on the accuracy of simulations before the actual launch. Additionally to the testing aspect of simulations, MATLAB also offers a variety of mathematical procedures which are often used to characterize sensors. In this thesis, the MATLAB version r2021a is used [MAT21].

2.2 Sensors for Attitude Determination

Several constraints heavily influence the amount of feasible sensors for the MOVE-III mission:

- **Accuracy**: The overall attitude determination needs to be accurate to under 1° for the MOVE-III mission, which indicates that the selected sensors need to be able to achieve this accuracy.
- **Availability**: Due to the semiconductor shortage caused by the COVID-19 pandemic in 2020 [WZD21], many sensors that might be of use are simply not available on the market.
- **Cost**: As of writing, the MOVE project has limited financial funds.
- **Documentation**: Due to a general high turnover rate within the MOVE project, documentation is essential for future developers. The documentation given by the manufacturers of a sensor has to include register mapping to enable implementation in DOSIS.

Time constraints limited this thesis to focus on only the Inertial Measurement Unit (IMU) rather than on other sensors.

2.2.1 Inertial Measurement Unit

The Inertial Measurement Unit (IMU) is a combination of multiple sensors. A common combination is a gyroscope for measuring angular velocity, a magnetometer for measuring the magnetic field, and an accelerometer for measuring linear acceleration.

As of writing this, there is no orbit control planned for the MOVE-III satellite. This means, that there will be no drastic change to the linear velocity of the satellite, which is why accelerometer readings are considered irrelevant in this context. The only relevant velocity change of the satellite is the angular velocity, e.g. after deployment from the launch vehicle.

Micro-Electro-Mechanical Systems (MEMS) sensors are relatively cheap, have low mass, and only require low power compared to other technologies. However, they also have a relatively low performance as well as lifetime, as described in [MC14].

Due to its low-cost characteristic, MEMS sensors are the focus of this thesis.

Gyroscope

MEMS gyroscopes are Coriolis Vibrating Gyros (CVG), which measure rotation using the coriolis force [MC14]. The measured values can be given in °/s or rad/s. To convert between the two units, the following equation is used:

$$1\,\mathrm{rad/s} = \pi/180 \cdot °/\mathrm{s} \tag{2.1}$$

Gyroscopes are characterised in this thesis using the following terms:

- **Range**: in °/s
- **Sensitivity**: describes the gain of the gyroscope [15] in Least Significant Bit (LSB)/°/s
- **Offset of a resting gyroscope (zero offset)**: in °/s
- **Temperature sensitivity drift**: influence of different temperature on the readings of the sensor in %/K or %/°C
- **Offset of a resting gyroscope (zero offset) over temperature**: in °/s/K or °/s/°C
- **Scale**: Multiplier to converse input angle rate to voltage, given in mV/°/s [EMC]
- **Nonlinearity**: Deviation from the straight line definition of the relationship between the in- and output [Tec] given in %

Most of these values can be extracted from the datasheet but may have varying titles, in which case a specific definition should be found in the datasheet.

Gyroscopes are susceptible to internal noise. Possible noise factors are described in List 2.2.1, alongside their causes, as described in [EHN08] and [Vec]:

- **Quantization noise**: converting analog measurements to digital output
- **Angle random walk**: integration over a noisy angular rate signal
- **Bias instability**: the random flickering of internal electronics
- **Rate random walk**: random error with uncertain origin
- **Drift rate ramp**: deterministic error

The concrete values can be sometimes found in the datasheet but can also be evaluated using the allan variance as done in Subsection 2.3.2.

Magnetometer

Magnetometers measure the ambient magnetic field. To determine the attitude of a spacecraft, the Earth's magnetic field is measured by the magnetometer.

Typical units can be either T for Tesla or G for Gauss. The conversion is 1 T = 10.000 G. Magnetometers can be characterized using the following terms:

- **Range**: in T or G
- **Sensitivity**: describes the gain of the sensor [15] in LSB/T or LSB/G
- **Offset of a resting magnetometer (zero offset)**: in T or G
- **Temperature sensitivity drift**: influence of different temperature on the readings of the sensor in %/K or %/°C

Similar to the gyroscope, magnetometer measurements are often affected by noise. Magnetometer measurements are directly influenced by their environment, as nearby magnetic fields influence the sensor reading, referred to as hard iron distortion [Mih+16]. This characteristic is of immense importance, especially in small spacecraft, such as satellites, as electronic components are integrated into a limited space. This limited space means that nearby generated magnetic fields have a stronger influence on the magnetometer readings than integration with more physical space.

Magnetic fields generated by nearby and internal electronics can disturb magnetometer measurements. Knowledge of the exact location and position of the magnetometer is essential, as this allows for calibration, which counteracts the disturbances.

Internal noise can be divided into four different noise sources as described in [Dra+14]:

- **Quantization noise**
- **Random walk or white noise**
- **Flicker noise**
- **Random walk**

The concrete values can sometimes be found in the datasheet but can also be evaluated using the allan variance as described in Section 2.3.2.

2.3 Error Coefficients

As described in Section 2.2, the measurements of both gyroscopes and magnetometers are generally affected by a certain amount of noise.

It can be differentiated between stochastic with a random origin, and deterministic errors, such as biases, caused during manufacturing [Qui+13]. The stochastic noise has a random origin, which cannot be estimated easily by onboard calibration software. This missing estimation raises the need to evaluate these error coefficients on the ground to improve the overall accuracy of sensor measurements. These error coefficients can be evaluated through models in either the frequency or time domain. The first approach is straightforward, however, it can be hard to understand for non-system analysts [Lam+03].

As described in Section 2.2.1, the error coefficients for the gyroscope and magnetometer differ in in literature. To avoid confusion, a uniform naming is introduced for this thesis and gathered in Table 2.1.

Introduced name	**Equivalent gyroscope after [EHN08]**	**Equivalent magnetometer after [Dra+14]**
Quantization noise	Quantization noise	White or quantization noise
White noise	Angle random walk	Random walk or white noise
Flicker noise	Bias Instability	Flicker noise
Random walk	Rate random walk	Random walk

Table 2.1: Introduced Error coefficient names

Table 2.1 does not include the drift rate ramp discussed for the gyroscope in List 2.2.1. This noise factor is neglected, which is explained in Section 2.3.3.

2.3.1 Power Spectral Density (PSD)

The Power Spectral Density (PSD) describes how the variance of a time series is distributed over a frequency [Lam+03]. Mathematically it is defined as a Fourier transformation and can be described as in [Qui+12] :

$$S_x(jw) = F[R_{xx}(\tau)] = \int_{-\infty}^{\infty} R_{xx}(\tau) e^{-\mathrm{jwt}} d\tau \tag{2.2}$$

with

- $S_x(jw)$: Power spectral density of process x

- $F[\cdot]$: Fourier transform
- $R_{xx}(\tau)$: autocorrelation of process x

The autocorrelation is necessary here, as the possible errors are not expected to be isolated from each other, but rather dependent on each other [HL06].

Plotting the result in a log-log graph enables the readout of the respective error coefficients using lines of different slopes fitted to the plotted graph.

The following sections explain each of the error coefficients as noted in Table 2.1. The equations are taken from [Lam+03], with adjusted variable names to adhere to the used naming in this thesis.

Quantization Noise

The quantization noise is quantified after [Lam+03] using:

$$X_{isolQN} = X_{totalnoise}(f_{i=1:n\_qn}) \tag{2.3}$$

with

- X_{isolQN}: PSD estimate for the isolated quantization noise
- $X_{totalnoise}$: PSD of all noise sources
- $f_{i=1:n\_qn}$: frequencies at which overall PSD levels

The quantization noise can be represented by a line with a slope of $+2$ fitted against the log-log plot. The error coefficient can be read out at frequency $f = 1$ [Lam+03].

White Noise

The error coefficient of the white noise can be described after [Lam+03] as:

$$X_{isolWN} = \frac{X_{totalnoise}(f_{i=1:n\_wn})}{2\pi {f_{i=1:n\_wn}}^2} \tag{2.4}$$

with

- X_{isolWN}: PSD estimate for the isolated white noise
- $X_{totalnoise}$: PSD of all noise sources
- $f_{i=1:n\_wn}$: frequencies at which overall PSD slope is close to -2

This can be represented by a line with a slope of 0 fitted against the log-log plot. The error coefficient can be read out at frequency $f = 1$ [Lam+03].

Flicker Noise

The flicker noise is described after [Lam+03] using:

$$X_{isolFN} = \frac{X_{totalnoise}(f_{i=1:n\_fn})}{2\pi {f_{i=1:n\_fn}}^3} \tag{2.5}$$

with

- X_{isolFN}: PSD estimate for the isolated flicker noise
- $X_{totalnoise}$: PSD of all noise sources
- $f_{i=1:n\_fn}$: frequencies at which overall PSD slope is close to -3

A line with a slope of -1 fitted against the log-log plot will allow the readout of the coefficient at frequency $f = 1$[Lam+03].

Random Walk

The random walk is described after [Lam+03] using:

$$X_{isolRW} = \frac{X_{totalnoise}(f_{i=1:n\_rw})}{2\pi {f_{i=1:n\_rw}}^4} \tag{2.6}$$

with

- X_{isolRW}: PSD estimate for the isolated random walk
- $X_{totalnoise}$: PSD of all noise sources
- $f_{i=1:n\_rw}$: frequencies at which overall PSD slope is close to -4

A line with a slope of -2 fitted against the log-log plot will allow the readout of the coefficient at frequency $f = 1$ [Lam+03].

2.3.2 Allan Variance

The allan variance can be used to evaluate the random noise sources corrupting sensor measurements [EHN08], [NAR08].

Unlike the previously described model, this technology is applied within the time domain [Qui+12].

This section describes the allan variance as explained in [EHN08] for a gyroscope; however, the terms are analogous for a magnetometer.

The allan variance can be estimated after [EHN08] using:

$$\sigma^2(T) = \frac{1}{2 \cdot (N - 2n)} \sum_{k=1}^{N-2n} (\overline{\Omega}_{next}(T) - \overline{\Omega}_k(T))^2 \tag{2.7}$$

with

- T: cluster time
- N: number of data points
- n: number of consecutive data points (with $n < N/2$)
- $\overline{\Omega}_k(T)$: average of the output rate per cluster
- $\overline{\Omega}_{next}(T)$: average of the subsequent cluster.

A data point taken at a specific sample time can be seen as a cluster [EHN08].

The average rates can also be described using:

$$\overline{\Omega}_k(T) = \frac{1}{T} \int_{t_k}^{t_k+T} \Omega(t)dt \tag{2.8}$$

and

$$\overline{\Omega}_{next}(T) = \frac{1}{T} \int_{t_{k+1}}^{t_{k+1}+T} \Omega(t)dt \tag{2.9}$$

$\Omega(t)$ is here the output rate of the sensor.

The following equation defines the allan variance dependent on the measurements of the sensor:

$$\theta(t) = \int^t \Omega(t)dt \tag{2.10}$$

Inserting Equation 2.10 into both Equations 2.8 and 2.9 and in turn into Equation 2.3.2 results in this estimation of the Allan Variance:

$$\sigma^2(T) = \frac{1}{2T^2 \cdot (N - 2n)} \sum_{k=1}^{N-2n} (\theta_{k+2n} - 2\theta_{k+n} + \theta_k)^2 \tag{2.11}$$

The relationship between the allan variance and the PSD can be described after [EHN08] using:

$$\sigma^2(T) = 4 \int_0^\infty df \cdot S_\Omega(f) \cdot \frac{sin^4(\pi f T)}{(\pi f T)^2} \tag{2.12}$$

With $S_\Omega(f)$ denoting the PSD of the random process $\Omega(T)$. A similar approach as described in Section 2.3.1 is taken to determine the error coefficients. Lines with specific slopes are fitted against the log-log plot of the allan variance and read out at specific values [EHN08].

Quantization Noise

The error coefficient Q_z can be read out using the formula after [EHN08]:

$$\sigma^2(T) = \frac{3Q_z^2}{T^2} \tag{2.13}$$

Graphically, this is achieved by fitting a line with a slope of -1 to the graph. The error coefficient is read out at time $x = \sqrt{3}$ [EHN08].

White Noise

The error coefficient can be read out using the formula after [EHN08]:

$$\sigma^2(T) = \frac{Q^2}{T^2} \tag{2.14}$$

This error equals a fitted line with a slope of $-1/2$ against the log-log plot. The coefficient can be read out at time $x = 1$ [EHN08].

Flicker Noise

The error coefficient can be read out using the formula after [EHN08]:

$$\sigma^2(T) = \frac{2 \cdot B^2}{\pi} \cdot [\ln 2 - \frac{\sin^3 x}{2x^2}(\sin x + 4x \cos x) + C_i(2x) - C_i(4x)] \tag{2.15}$$

with

- x: described as $\pi f_0 T$
- C_i: cosine-integrated function

This error is represented by a fitted line with a slope of 0 against the log-log plot. The coefficient can be read out at $y = \sqrt{2ln2/x}$ [EHN08].

Random Walk

The error coefficient can be read out using the formula after [EHN08]:

$$\sigma^2(T) = \frac{R^2 T}{3} \tag{2.16}$$

This error equals a fitted line with a slope of 1 against the log-log plot. The coefficient can be read out at time $x = \sqrt{2}$ [EHN08].

2.3.3 Summary

Table 2.2 serves as a summary of the previously introduced error coefficient and how to evaluate them with the help of a log-log graph. The "slope" values in the Table refer to the slope a fitted line against the log-log graph has to visualize the error source. The "readout" values refer to the respective x- or y- coordinate to read out the error coefficient.

Error coefficient	Slope allan variance	Read out allan variance	Slope PSD	Read out PSD
Quantization noise	-1	$x = \sqrt{3}$	$+2$	$x = 1$
White noise	$-1/2$	$x = 1$	0	$x = 1$
Flicker noise	0	$y = \sqrt{2ln2/x}$	-1	$x = 1$
Random walk	$1/2$	$x = 3$	-2	$x = 1$

Table 2.2: Summary of described slopes for allan variance and PSD

Table 2.2 does not include the drift rate ramp as an error source for the gyroscope as described in List 2.2.1. This error source is neglected for the remainder of this thesis, as no literature could be found with a definition of this error through the PSD. While some literature for the allan variance defines this error, such as [EHN08], others do not note this. [Lam+03], which was used here to explain the PSD in Section 2.3.1, refers each discussed error term in PSD to its equivalent calculated through the Allan Variance. The paper does, however, omit the drift rate ramp . As no literature could be found evaluating the drift rate ramp with PSD, and some papers, like [Lam+03], seemed to omit the error source, it is neglected for the remainder of this thesis.

2.4 Calibration

Internal as well as external influences corrupt IMU measurements, as previously described in Section 2.2.1. Calibration is employed to counteract these influences, which allows for a more accurate sensor measurement [PNS21].

For this thesis, a feasible calibration method needs to be selected. For this, two calibration algorithms are considered in the following subsections.

2.4.1 TWOSTEP Algorithm

The TWOSTEP algorithm first centers the sensor data analytically and then improves the calculated values numerically. Alonso et al. proposed this algorithm in [AS03], one of the most popular calibration methods [PNS21]. This algorithm does not require

any previous knowledge or any additional sensors or other additional measurement equipment [PNS21].

Measurement model

Before calibrating a magnetometer, its measurements must be modeled to fully grasp each influencing factor's importance. In [MC14] the magnetometer measurements are modelled as

$$B_k = (\mathbf{I_3} + \mathbf{D}^{true})^{-1}(\mathbf{O}^T \mathbf{A_k}^{true} R_k + b^{true} + \epsilon_k), k = 1, 2, ...N \tag{2.17}$$

where the variables have the following meaning [MC14]:

- B_k: denotes the measurement of the magnetometer at time t_k
- $\mathbf{D}^{true}$: scale factor matrix
- $\mathbf{O}$: unknown orthogonal matrix
- $\mathbf{A}_k^{true}$: unknown attitude matrix
- R_k: magnetic field strength vector
- b^{true}: bias of the magnetometer measurements
- ϵ_k: noise vector
- $\mathbf{I_3}$: $3x3$ identity matrix

The following paragraphs follow the description of the algorithm as shown in [PNS21].

Calculate the effective measurement

First, the TWOSTEP after Alonso calculates the effective sensor measurement z_k and defines the auxillary variable L_k:

$$z_k = ||y_k||^2 - ||m_k||^2 \tag{2.18}$$

and

$$S_k = [y_{k,1}^2 \quad y_{k,2}^2 \quad y_{k,3}^2 \quad 2y_{k,1}y_{k,2} \quad 2y_{k,1}y_{k,3} \quad 2y_{k,2}y_{k,3}] \tag{2.19}$$

$$L_k = [2y_k^T - S_k] \tag{2.20}$$

with y_k denoting the sensor measurements and m_k referring to the magnetic field vector. The notation $|| \cdot ||$ denotes the Euclidian norm [PNS21]. S_k is an axuxillary variable[PNS21].

Calculation of the centered solution

With these first variables calculated in Paragraph 2.4.1, the centered solution for the TWOSTEP algorithm is determined.

First, the centered solution is calculated. $\widetilde{z}$ represents the centered solution for the effective measurements, while $\widetilde{L}$ is an auxillary variable [PNS21]:

$$\bar{z} = \bar{\sigma}^2 \sum_{k=1}^{N} \frac{1}{\sigma_k^2} z_k \,,\, \widetilde{z}_k = z_k - \bar{z} \tag{2.21}$$

$$\bar{L} = \bar{\sigma}^2 \sum_{k=1}^{N} \frac{1}{\sigma_k^2} L_k \,,\, \widetilde{L}_k = L_k - \bar{L} \tag{2.22}$$

with

$$\bar{\sigma}^2 = (\sum_{k=1}^{N} \frac{1}{\sigma_k^2})^{-1} \tag{2.23}$$

The variable σ_k^2 describes the variance of the measurement noise, while σ^2 is the variance of the error in the output. The variable $\widetilde{\mu}$ represents the centered solution for the noise and is calculated in the following equation [PNS21]:

$$\bar{\mu} = \bar{\sigma}^2 \sum_{k=1}^{N} \frac{1}{\sigma_k^2} \mu_k \,,\, \widetilde{\mu}_k = \mu_k - \bar{\mu} \tag{2.24}$$

μ_k is the mean of the noise term of the sensor. It can be described as [PNS21]:

$$\mu_k = -3\sigma^2 \tag{2.25}$$

The centered estimate of $\widetilde{\theta}'$ and the covariance matrix $\widetilde{P}_{\theta',\theta'}$ are calculated after [PNS21]:

$$\widetilde{\theta}' = \widetilde{\mathbf{P}}_{\theta',\theta'} \sum_{k=1}^{N} \frac{1}{\sigma_k^2} (\widetilde{z}_k - \widetilde{\mu}_k) \widetilde{L}_k^T \tag{2.26}$$

$$\widetilde{\mathbf{P}}_{\theta',\theta'}^{-1} = \sum_{k=1}^{N} \frac{1}{\sigma_k^2} \widetilde{L}_k^T \widetilde{L}_k \tag{2.27}$$

Extraction of c and E

The auxillary variables for the $3x1$ vector c and the $3x3$ matrix E are defined as [PNS21]:

$$c = [\theta_1' \theta_2' \theta_3']^T \tag{2.28}$$

$$\mathbf{E} = \begin{bmatrix} \theta_4' & \theta_7' & \theta_8' \\ \theta_7' & \theta_5' & \theta_9' \\ \theta_8' & \theta_9' & \theta_6' \end{bmatrix} \tag{2.29}$$

Calculate g and ϕ

As an auxillary variable, v is introduced [PNS21]:

$$v = (\mathbf{I_3} + \mathbf{E})^{-1} c \tag{2.30}$$

This variable is then used to calculate $\phi(\theta')$ which is defined as [PNS21]:

$$\phi(\theta') = \begin{bmatrix} 2v \\ -v_1^2 \\ -v_2^2 \\ -v_3^2 \\ -2v_1v_2 \\ -2v_1v_3 \\ -2v_2v_3 \end{bmatrix} \tag{2.31}$$

and

$$g(\theta') = \widetilde{\mathbf{P}}^{-1}_{\theta',\theta'}(\theta' - \widetilde{\theta'} - \frac{1}{\bar{\sigma}^2}(\bar{z} - \bar{L}\theta' + c^{\mathrm{T}}v - \bar{\mu})(\bar{L}^{\mathrm{T}} - \phi(\theta')) \tag{2.32}$$

Update θ'

θ' is updated using [PNS21]:

$$\theta'_{i+1} = \theta'_i - [\widetilde{\mathbf{F}}_{\theta',\theta'} + \frac{1}{\bar{\sigma}^2}(\bar{L} - \phi(\theta'_i))^T(L - \phi(\theta'_i))]^T g(\theta'_i) \tag{2.33}$$

The variable $\widetilde{F}_{\theta',\theta'}$ is the centered Fischer information matrix [PNS21].

Calculate η

The variable η serves as a stop condition for the algorithm. It is calculated using [PNS21]:

$$\eta_i = (\theta'_{i+1} - \theta'_i)^T[\widetilde{\mathbf{F}}_{\theta',\theta'} + \frac{1}{\bar{\sigma}^2}(\bar{L} - \phi(\theta'_i))^T(\bar{L} - \phi(\theta'_i))](\theta'_{i+1} - \theta'_i) \tag{2.34}$$

Unless this value is smaller than a given threshold, the algorithm repeats the calculation, starting from Section 2.4.1.

Determination of values

After η has reached an arbitrarily small amount, the final values for the symmetric matrix $\mathbf{D}$ and the bias vector h are calculated. This calculation is achieved by first

performing a Single Value Decomposition (SVD) on the final **E** matrix calculated by the previously explained points [PNS21]. This calculation is defined as [PNS21]:

$$\mathbf{E} = \mathbf{U}\mathbf{S}\mathbf{U}^T \tag{2.35}$$

The matrix **E** is decomposed into the matrices **U** and **S**, a diagonal matrix and **U** a unitary matrix [PNS21]. The matrix **D** is then defined as [PNS21]:

$$\mathbf{D} = \mathbf{U}\mathbf{W}\mathbf{U}^T \tag{2.36}$$

The matrix **W** is defined as a diagonal matrix with the entries being calculated with [PNS21]:

$$w_j = -1 + \sqrt{1 + s_j}\,,\ j = 1, 2, 3 \tag{2.37}$$

The vector h is then calculated after [PNS21] using:

$$h = (\mathbf{I_3} + \mathbf{D})^{-1} c \tag{2.38}$$

2.4.2 Magcal- MATLAB Implementation

MATLAB offers its implementation of a magnetometer calibration through the method called **magcal**. The method follows a geometric approach by fitting recorded data to a central sphere with the radius of the magnetic field strength [Matf]. This function returns the values b and A, the first one being a correction of the bias of the uncalibrated measurements, the latter correcting soft-iron influences [Matf].

Measurement model

The magcal implementation of MATLAB assumes the data is distributed in the room on an ellipsoid [Matg] and models uncalibrated magnetometer data after [Matg] using:

$$(x - b)\mathbf{R}(x - b)^T = \beta^2 \tag{2.39}$$

with

- **R**: 3x3 matrix
- x: 3 value vector of uncalibrated magnetometer data
- b: 3 value vector, indicating the offset
- β: scalar, indicating the magnetic field strength

3 Practical Approach

3.1 Sensor Selection

Using an IMU rather than individual sensors has the advantage of reducing the size and synchronizing the sensor measurements, as they are integrated into one unit, rather than spread out physically. However, the available IMUs are limited, and not all possible configurations of individual sensors are being produced.

In order to give a better comparison of possible sensor options, both IMUs and separate sensors were selected and characterized.

3.2 Implementation

3.2.1 Implementation in DOSIS

The sensors were implemented in DOSIS. The sensor data was read out for each sensor, directly alongside temperature data from the sensors.

Communication with all sensors was implemented using the Inter-integrated circuit (I^2C) protocol.

Each sensor offers a variety of user-defined settings for each sensor. The following Table 3.1 shows the exact configuration of each sensor.

Sensor	Settings
BNO055 [21d]	Operating mode: "maggyro", Ranges set to maximum
LSM9DS1 [15]	Ranges set to maximum, Filtering disabled, Compensation enabled magnetometer Continuous conversion mode
ICM20948 [17a]	Range set to maximum
LIS3MDL [17b]	Range set to maximum, Continuos mode, High performance enabled on all three axes
BMI088 [21c]	Range set to maximum

Table 3.1: Sensor settings

It has to be noted that the modifiable sensor's settings vary. This is why more settings were listed for some sensors than others; the general approach was to ensure a homogeneous configuration across the sensors.

3.3 Methodology

This section describes all conducted experiments.

3.3.1 Evaluation of Error Coefficients

In order to evaluate the error coefficients of the sensor, the allan variance, as described in Subsection 2.3.2 is utilized. The allan variance of the recorded data is evaluated using the method `allanvar`, as implemented in MATLAB [Matb]. Additionally, Welch's power spectral density is implemented in MATLAB through the `pwelch` method. It is used to determine the error coefficients using the PSD as described in Section 2.3.1.

Both approaches require undisturbed data recorded over a long period.

For this, every sensor is connected to a Nucleo development-board [20a], which is connected to a laptop, to power the sensor and the microcontroller, and log the data. Each sensor is recorded for at least four hours in an undisturbed room with a constant room temperature. This setup can be seen in Figure 3.1.

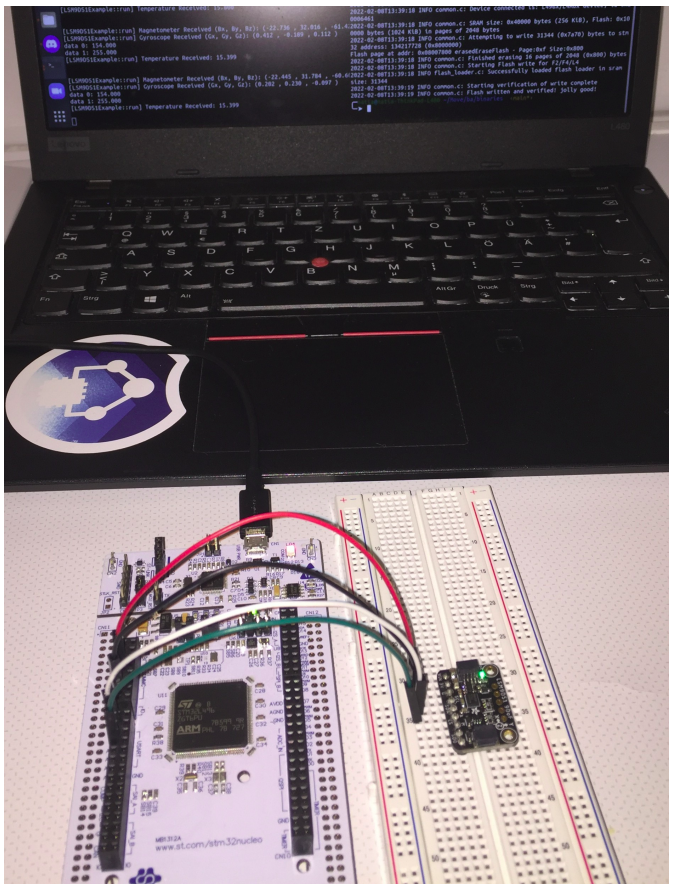

Figure 3.1: Setup longterm experiments

To ensure that measurements were reproducible, all measurements were also conducted using another new sensor of the same model.

The difference between the calculated error coefficients of the original and the new sensor using Equation 3.3.1:

$$\Delta_{TwoSensors} = \frac{E_{new} - E_{original}}{E_{original}} \cdot 100 \tag{3.1}$$

with E denoting the respective error coefficients calculated through the allan variance. This difference can be used to verify whether either sensor was behaving according to its standards or not. A small deviation indicates that the sensor measurements can be considered consistent, while a bigger deviation indicates a fault of one of the sensors. This fault may have arisen during the production of one of the sensors or throughout the testing process.

The lines fitted against the graph were generated using the code given in [Mate]. While the underlying mathematical concept is the allan variance, the Allan deviation has to be examined to extract the error coefficients. The code used for the allan variance plots is also used to evaluate the error coefficients for the PSD. As this method requires different slopes, the code must be adjusted appropriately. This implementation could be achieved for all slopes except a level slope. This circumstance is why such a slope had to be excluded from further visual analysis. The concrete percentual deviation between the error coefficient calculated by the PSD and the allan variance is determined using:

$$\Delta_{TwoMethods} = \frac{E_{PSD} - E_{AllanVariance}}{E_{AllanVariance}} \cdot 100 \tag{3.2}$$

with E denoting the error coefficient calculated by the respective method.

For the PSD calculation and the allan variance, the same dataset is used, which is the first one recorded of the respective original sensor.

3.3.2 Temperature Experiments

Several temperature experiments were undertaken to characterize the influence of temperature on sensor measurements.

Thermal Vaccum Chamber Test (TVAC)

Three days prior to the launch of a high-altitude balloon on the 16th of October 2021, a Thermal Vaccum Chamber Test (TVAC) test was conducted.

This test lasted five hours, and the system experienced temperatures between 40 °C and -20 °C.

Due to an issue with the data logging, only partial data could be retrieved. This missing data complicated the analysis of the experiment.

The recorded measurements of the BNO055 were analyzed against the temperature. The BME680 sensor, a temperature, pressure, and humidity sensor [21a] recorded this data and was used on the balloon flight.

The logs selected for the analysis have to be recordings from within the TVAC and contain multiple data points. The drift is the slope of a straight line fitted to the graph.

Repeated Heat Experiments

Further temperature experiments were executed with a heat lamp. The observed temperature ranges lay between 25 °C and around 60 °C.

The setup of this experiment can be seen in Figure 3.2.

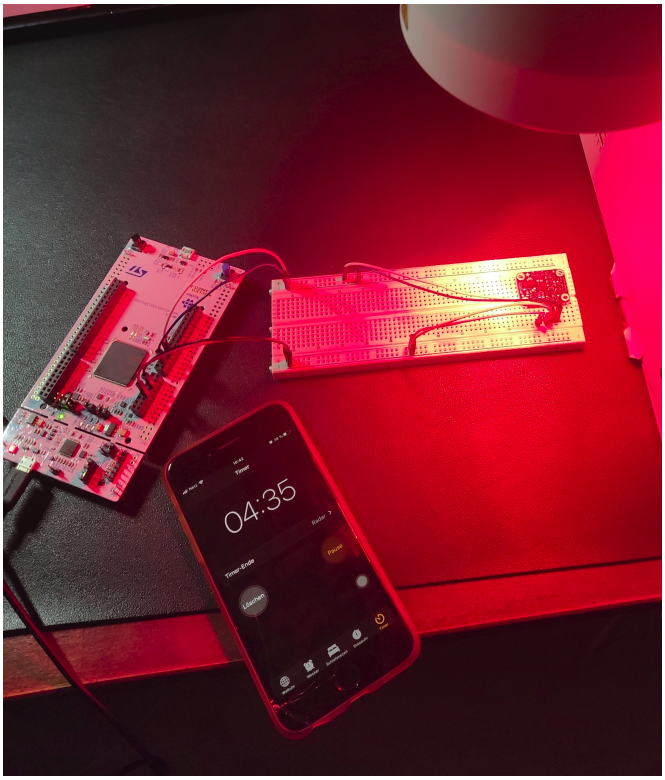

Figure 3.2: Setup temperature experiments

The breakout board of the sensor is located 20 cm directly underneath the heat lamp. The heat lamp heats the sensors for five minutes before the sensors are left for five minutes to cool down. The generated data is recorded for the whole ten minutes. A break of more than five minutes between each sensor experiment is taken. This pause ensures that all sensors have equal starting conditions.

A crucial aspect of these experiments is their reproducibility to show the accuracy of the found results. This is why, each experiment is repeated twice per sensor. A third run is conducted to verify the calculated values, in which new sensors of the same model were used.

These different setups are gathered in Table 3.2.

Name	Explanation
First run	First temperature run with the original sensor
Second run	Second run with the original sensor
Third run	First run of a new sensor of the same model

Table 3.2: Overview Temperature experiments

The gathered sensor data is then plotted against the recorded temperature data. The drift of each axis is then evaluated using `polyfit`, which fits a polynomial curve against a graph [Math]. In this case, only a linear curve is needed to approximate the concrete slope of the measurements. This linear curve describes both the slope and the offset of the measurements relative to zero.

For the two initial experiment runs, the absolute averages and differences were calculated. The measurements of the third run were compared to the first one. To calculate the percentual deviation of the new sensors from the original sensors measurements, the following equation is used:

$$\Delta_{TwoSensors} = \frac{D_{newSensor} - D_{oldSensor}}{D_{oldSensor}} \tag{3.3}$$

with D indicating the respective drift values.

3.4 Simulation

Simulation is crucial to the ADCS as they enable testing in a simulated space environment. As the natural space environment is only reached after launch, testing in a simulated environment becomes crucial to verify the system.

There are multiple possibilities for simulating IMUs in MATLAB, such as using the simulation tool Simulink [Doc20] or the methods for the imuSensor object offered by MATLAB [Matd]. This approach allows the user to specify parameters for accelerometers, magnetometers, and gyroscopes [Matd].

3.4.1 Gyroscope Simulation

Both Simulink and the imuSensor implementation offered by MATLAB can simulate a gyroscope.

Simulink

The Figure 3.3 shows the model which was used for the gyroscope simulation.

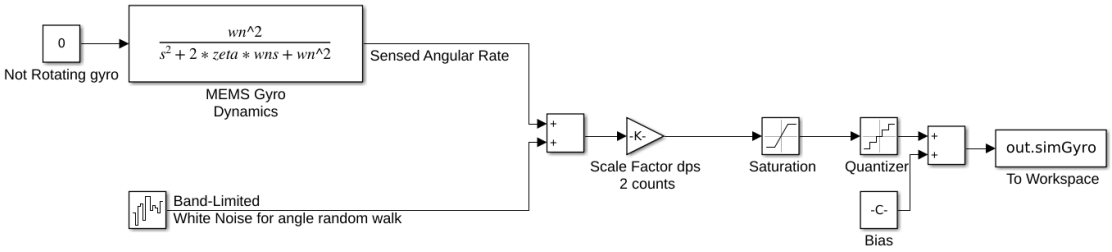

Figure 3.3: Gyroscope simulation in Simulink

The model in Figure 3.3 was based on [KK19] and [Dou13] and slightly modified to better approximate the simulation by applying the bias later in the simulation.

The model adds White Noise onto the gyroscope dynamics before applying the sensor's sensitivity as a scale factor. The data itself has to be saturated as the resulting values can not be represented by an infinitesimally small number [Dou13]. The data also needs to be quantized, as the gyroscope does not continuously generate data. Finally, the bias is added onto the simulated measurements to account for deterministic errors of the sensor.

3.4.2 Magnetometer Simulation

The magnetometers were simulated using the imuSensor implementation, as no mathematical simulation was found that can be implemented using Simulink.

3.4.3 Analysis

The simualted data was suscepted to the allan variance. The values were then compared against the values calculated from the recorded using

$$\Delta_{Simulation} = \frac{E_{simulated} - E_{recorded}}{E_{recorded}} \tag{3.4}$$

with E denoting the calculated error coefficient from the respective data.

3.5 Calibration

In order to evaluate the two calibration methods, the scripts developed by Crassidis were used for the TWOSTEP after Alonso implementation [Cra]. This implementation is simply referred to as TWOSTEP throughout this thesis.

Analyzing and comparing the calibration results was difficult, as the correct calibrated measurements of a sensor recording were unknown. Simulated data were used instead to determine how well the algorithms can determine the biases and scale factor. This data has fixed bias and scale values applied to it so that the calculated results from the algorithms can be compared to the initial parameters.

For the magcal method [Matf], the data was simulated using the imuSensor implementation by MATLAB [Matd] after [Matg]. The TWOSTEP algorithm uses an already built-in Monte-Carlo simulation in the script after Crassidis [Cra]. It was not possible to standardize the simulation approaches.

There are two parameters that the calibration algorithms, as described in Section 2.4, calculate, the bias vector as well as a scale matrix. These parameters can be set to certain values in [Matg] for magcal and [Cra] for the TWOSTEP. Two different approaches were taken to independently evaluate their influence on the deviation of the calculated values from the set once.

First, the scale was set to a fixed value, while the inputted bias vector changes. Then, this vector was fixed, while the scale matrix was set to different values in each run. Subsections 3.5.1 and 3.5.2 depict the input parameters for the respective cases.

3.5.1 Fixed Scale Matrix

As a constant bias four different values were used as depicted in Table 3.3.

Set	**X-bias in µT**	**Y-bias in µT**	**Z-bias in µT**
Set 1	-34.132	-244.33	15.000
Set 2	2	10	4
Set 3	20	0	9
Set 4	42.33	-74.3	21.98

Table 3.3: Biases used for calibration analysis

The values in Table 3.3 were chosen arbitrarily to cover a wide range of possible offsets.

For the scale matrix $\mathbf{S}$, one matrix was used to focus solely on each algorithm's change

in calculated biases. The values for this matrix were selected as follows:

$$\mathbf{S} = \begin{bmatrix} 0.9 & 0.5 & 2 \\ 0.5 & 2 & 0.1 \\ 2 & 0.1 & 3 \end{bmatrix} \tag{3.5}$$

The biases were input as a constant bias to the imuSensor object, while the scale matrix was applied to the imuSensor magnetic Field, as shown in [Matg].

3.5.2 Fixed Bias

To further elaborate on the difference between the three calibration methods, the bias was constant with different scale matrices as an input.

The used bias was:

$$Bias = \begin{bmatrix} 2\mu T & 10\mu T & 4\mu T \end{bmatrix} \tag{3.6}$$

This bias was used as the second set of biases in the previous experiment showed a stabilization of the scale matrix calculated by the TWOSTEP Alonso implementation for the following bias sets.

The four sets of used scale matrices are listed in Table 3.4.

Set	Scale matrix
Set 1	$\begin{bmatrix} 0.9 & 0.5 & 2 \\ 0.5 & 2 & 0.1 \\ 2 & 0.1 & 3 \end{bmatrix}$
Set 2	$\begin{bmatrix} 10 & 0.5 & -2 \\ 0.5 & 5 & 0.1 \\ -2 & 0.1 & 3 \end{bmatrix}$
Set 3	$\begin{bmatrix} 0.9 & -30 & 2 \\ -30 & 2 & 1 \\ 2 & 1 & 3 \end{bmatrix}$
Set 4	$\begin{bmatrix} 0.9 & 0.6 & 0.01 \\ 0.47 & 2 & 0.21 \\ 2 & -0.1 & 3 \end{bmatrix}$

Table 3.4: Scale matrices used for calibration analysis

3.5.3 Comparison

In order to compare the calculated bias vectors and scale matrices, the respective magnetometer measurement model has to be taken into consideration. It can be seen,

that the two models represented in Equations 2.4.1 and 2.4.2 are not equivalent. To compare the algorithms with their different models, one model would be converted into the other. Solving both models after their respective scale matrix or bias vector allows for a coefficient comparison between the two models. This would then allow determining a conversion of one model into the other.

First, the Crassidis model, presented in Section 2.4.1 was reiterated upon. The presented model contains many unknown values and is not considered in this analysis. These missing values include the attitude matrix, the orthogonal matrix, as well as the noise of the magnetometer.

The value for the magnetic field strength R_k was assumed to be $50\mu T$ in the script offered by Crassidis [Cra]. This results in the previous model being simplified into:

$$B_k = (\mathbf{I_3} + \mathbf{D^{true}})^{-1}(R_k + b^{true}), k = 1, 2, ...N \tag{3.7}$$

This allows for easy solving for either the bias vector:

$$b^{true} = B_k \cdot (\mathbf{I_3} + \mathbf{D^{true}}) - R_k, k = 1, 2, ...N \tag{3.8}$$

or the scaling matrix:

$$\mathbf{D^{true}} = \frac{R_k + b^{true}}{B_k} - I_3, k = 1, 2, ...N \tag{3.9}$$

Unfortunately, a similar transformation was not possible with the magnetometer model used for the magcal implementation as shown in Equation 2.4.2.

The reason for this was the missing reference value of the magnetic field strength. Such value for this could not be found in the documentation of magcal [Matf] or its described use case [Matg].

This was why the values calculated by the respective calibration algorithm could not be directly compared; however, a general comparison for simulated values was undertaken.

4 Results

4.1 Sensor Selection

As mentioned in the List 2.2, the selection of possible sensors was not only limited by the characteristics of the datasheet but also external factors.

This led to the selection of five sensors, the IMUs BNO055, ICM20948, and the LSM9DS1. Additionally, the magnetometer LIS3MDL and the gyroscope and accelerometer BMI088 were selected. These are the sensors that were analyzed throughout this thesis in order to determine the best option for a final IMU decision.

The Table 4.1 gives an overview of the characteristics of the gyroscope sensors as read from their respective datasheets.

Gyroscope	Range	Sensitivity	Zero-offset	Temperature sensitivity drift	Zero-offset over temperature	Nonlinearity in %
BNO055[21d]	± 125 °/s to ± 2000 °/s	16 LSB/°/s	± 1 °/s	± 0.03 %/K to ± 0.07 %/K	± 0.015 °/s/K to ± 0.03 °/s/K	± 0.05
LSM9DS1[15]	± 245 °/s to ± 2000 °/s	8.75 °/s/LSB to 70 °/s/LSB	± 30 °/s	/	/	/
ICM20948[17a]	± 245 °/s to ± 2000 °/s	131 LSB/°/s to 16.4 LSB/°/s	± 5 °/s	/	± 0.05 °/s/°C	± 0.1
BMI088[21c]	± 125 °/s to ± 2000 °/s	262.144 LSB/°/s to 16.384 LSB/°/s	± 1°/s	± 0.03 %/K	± 0.015 °/s/K	± 0.05

Table 4.1: Characteristics of the selected gyroscopes

The characteristic of the scale, as described in Section 2.2.1 could not be found in any of the gyroscope datasheets, which is why it is not included in Table 4.1.

As the IMU selection also depended on the integrated magnetometer sensors, their characteristics also had to be evaluated. Table 4.2 shows these specifications as found in the respective datasheets.

Magnetometer	Range	Sensitivity	Zero-offset	Temperature sensitivity drift	Zero-offset over temperature
BNO055[21d]	± 1300 µT x-,y-axis ± 2500 µT z-axis	16 LSB/°/s	± 40 µT	± 0.01 %/K to ± 0.03 %/K	± 0.23 µT/K to ± 0.37 µT/K
LSM9DS1[15]	± 4 G to ± 16 G	0.14 mG/LSB to 0.58 mG/LSB	± 1 G with a scale of ± 4 G	/	/
ICM20948[17a]	± 4900 µT	0.15 µT	/	/	/
LIS3MDL[17b]	± 4 G to ± 16 G	6842 LSB/G to 1711 LSB/G	± 1 G for a range of ± 4 G	/	/

Table 4.2: Characteristics of the selected magnetometers

All of the units have been kept consistent with their respective datasheets.

The BNO055 had already been in development as it has similar characteristics to the BMX055. This sensor has been used on the satellite MOVE-II [Mes+17].

The LSM9DS1 seemed promising, as the magnetometer specifications showed a smaller zero-rate offset for the magnetometer than the BNO055. Even though the datasheet gives this specification for the smallest range possible, it was hoped that such a small zero-offset could also be maintained at higher ranges. The zero-offset of the gyroscope appears to be at a high value [15].

This high value raised the need for a third IMU with a lower zero-rate offset than the LSM9DS1 gyroscope. This sensor was found in the ICM20948, whose gyroscope zero-offset was more similar to the values given in the BNO055 datasheet [21d]. Furthermore, the broader range of the ICM20948 magnetometer compared to the other sensors seemed to be intriguing [17a].

This concludes the selection of the IMUs. This selection, however, was intended to be expanded with the help of a standalone magnetometer and a standalone gyroscope and accelerometer.

For the magnetometer, the LIS3MDL was chosen. Its datasheet [17b] indicates similar characteristics to the LSM9DS1 [15], which made it viable for a direct comparison.

The BMI088 showed similar characteristics considering sensitivity and zero-offset when compared to the BNO055. Additionally, its parameters regarding drift induced from temperature changes were lower, which qualified it as a direct comparison gyroscope [21c].

Multiple breakout boards were ordered with each sensor, to minimize the probability of issues caused in production or transportation. This ordering process does not hold for the BMI088, as only one breakout board was found available, which was the one that was ordered and used throughout the thesis.

The reason why breakout boards were ordered instead of the sensors in a standalone

way, was to reduce the time until testing of the sensor would be possible.

4.2 Implementation

During the implementation of the ICM02948, issues with the communication to the magnetometer were encountered. The source of this issue has not been found. The ICM20948 uses two different I^2C addresses to communicate with the gyroscope or the magnetometer. While communication with the first works without flaws, the latter can not be addressed. As multiple breakout boards have been tested with the same code and no communication with the magnetometer was possible, a hardware issue was also ruled out. When referencing the ICM20948, only the gyroscope is considered.

All gyroscope output in this thesis was read out in the unit °/s, while the magnetometer data was read out in µT. The temperature data of the BNO055, LSM9DS1, and ICM20948, was read out in °C. For the LIS3MDL and the BMI088, the read temperature values do not match with the actual temperatures in °C. However, changes in the ambient temperature did affect the temperature sensor output accordingly. This change in values was seen as a reasonable implementation, as the temperature change was more important than the actual value.

4.3 Error Coefficients

The following results stem from the long term recordings of the sensors. The initial start conditions are gathered in Subsection 3.3.1.

4.3.1 BNO055

Allan Deviation

Gyroscope Figure 4.1 shows the allan deviation of all gyroscope axes of the BNO055 gyroscope.

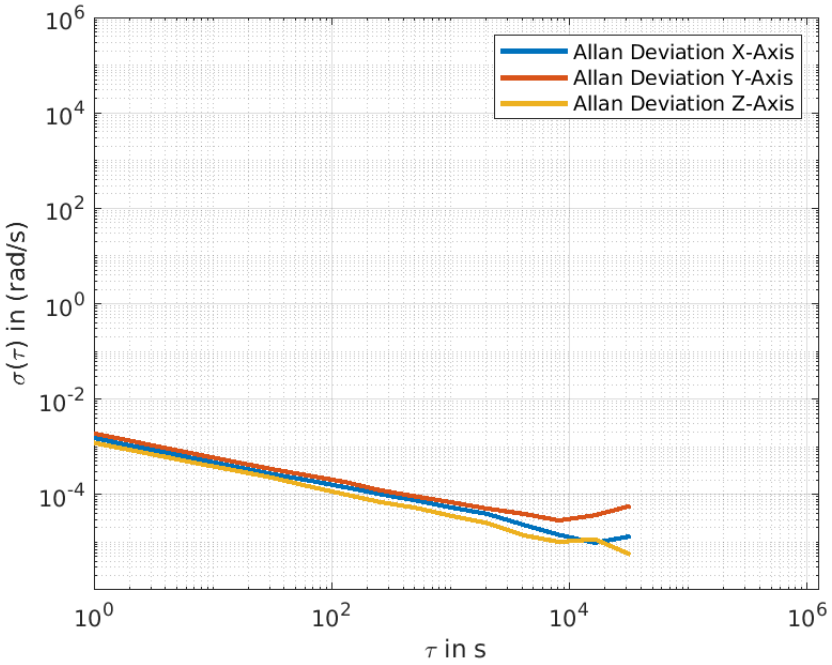

Figure 4.1: Allan deviation of the BNO055 gyroscope

The x- and the y-axis appear to be quite similar in that they both only show one kink and are composed of two relative straight lines with a slope of $-1/2$. The z-axis seems to be influenced by multiple error sources, as two kinks in the graph indicate. It can also be observed that the y-axis is the highest of the three plots, followed by the x- and then the z-axis.

To further analyze the separate error coefficients of each axis, they were evaluated with fitted lines against the plot.

Figure 4.2 shows the allan deviation of the x-axis of the gyroscope of the BNO055, alongside all four possible slopes fitted against the graph as explained in Table 2.2.

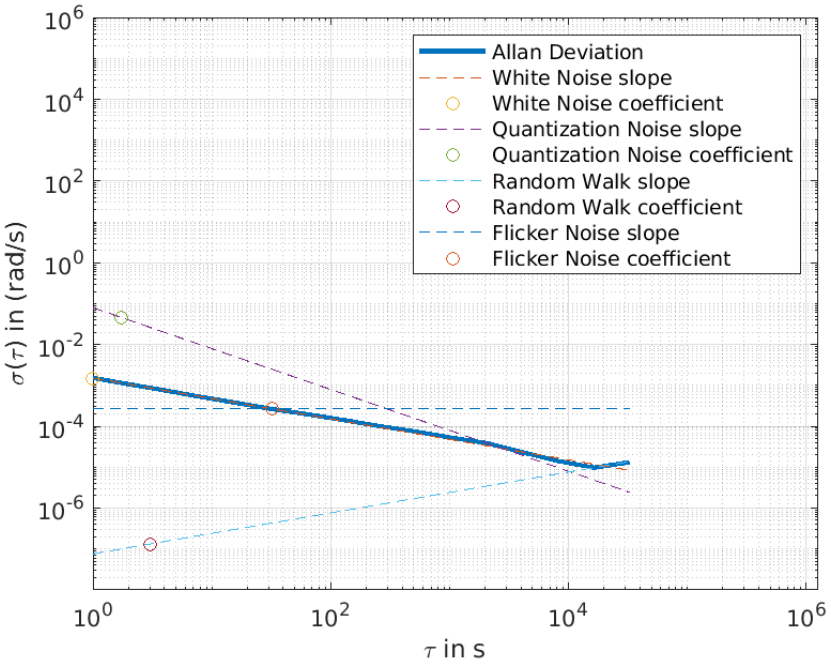

Figure 4.2: Allan deviation of the BNO055 gyroscope on the x-axis

While there are lines equivalent to both the quantization noise, indicated by the slope of -1 and flicker noise, indicated by the slope of 0, fitted against the graph, they only shortly fully describe the behavior of the graph. These two errors do exist but barely influence the x-axis of the gyroscope, which is why their values can be ignored.

Figure 4.3 shows the evaluation of the y-axis of the BNO055 gyroscope.

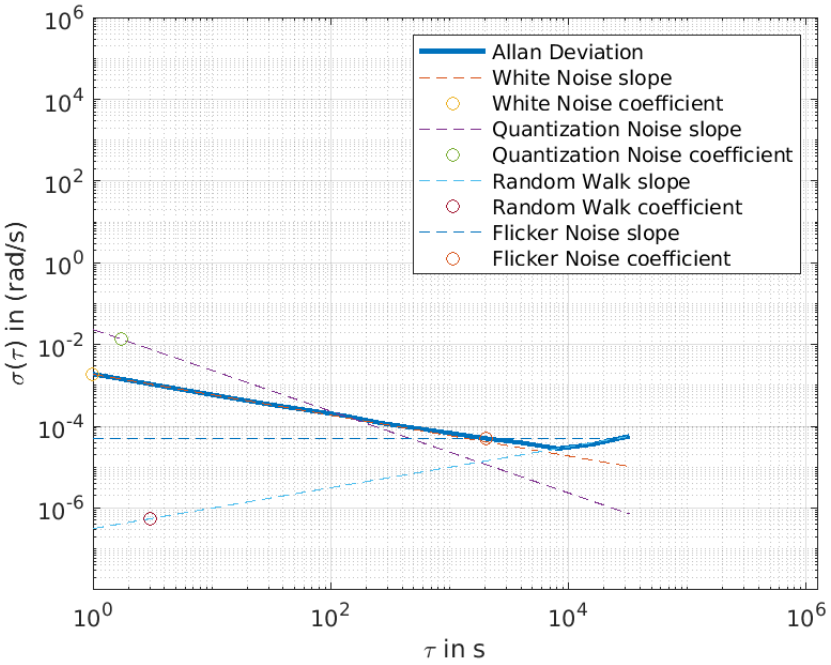

Figure 4.3: Allan deviation of the BNO055 gyroscope on the y-axis

Similar to the x-axis depicted in Figure 4.2, the white noise seems to be the most influencing error source on the measurement. It can also be seen that while the lines for quantization noise and flicker noise are fitted against the plot, they do not fully match the slope of the graph. The quantization noise impacts the sensor measurements for a short while around a sample size of a bit over $10^2 s$. The flicker noise can not be fitted against the graph.

Figure 4.4 depicts the allan deviation of the gyroscope z-axis.

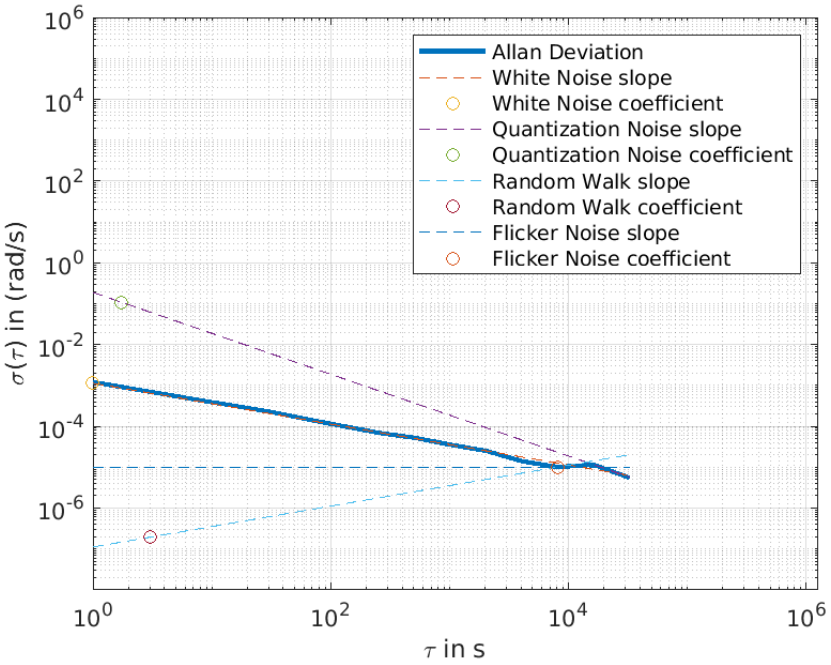

Figure 4.4: Allan deviation of the BNO055 gyroscope on the z-axis

The allan deviation of the z-axis in Figure 4.4 shows that again, for shorter cluster times, the white noise is the most prominent error on the sensor measurements on this axis. For larger cluster times, however, the flicker noise, random walk, and quantization noise significantly impact the sensor measurements.

The error coefficients of all the axes are summarized in Table 4.3:

Axis	**Quantization noise in** $(\mathrm{rad/s})/\sqrt{\mathrm{Hz}}$	**White noise in** $(\mathrm{rad/s})/\sqrt{\mathrm{Hz}}$	**Flicker noise in** $(\mathrm{rad/s})$	**Random walk in** $(\mathrm{rad/s})/\sqrt{\mathrm{Hz}}$
x-axis	0.046037	0.0015144	0.00039819	$1.3132 \cdot 10^{-7}$
y-axis	0.013544	0.0018760	$7.5660 \cdot 10^{-5}$	$5.4495 \cdot 10^{-7}$
z-axis	0.10845	0.0011311	$1.5180 \cdot 10^{-5}$	$1.9297 \cdot 10^{-7}$

Table 4.3: Error coefficients BNO055 gyroscope calculated by the allan deviation

The error values depicted in Table Table 4.3 have to be evaluated alongside the respective plots of the allan deviation. Some values appear small, such as the flicker noise for the y- and z-axis. This can most likely be attributed to inaccuracies concerning the evaluation through fitted lines. Figures 4.2, 4.3, and 4.4 show that the slope for the

flicker noise was only barely fitted against the allan deviation of the axes, but rather against fragments in the respective curves. This indicates a strong inaccuracy for determining the error coefficient of the flicker noise.

A similar observation can be made for the error coefficient of the quantization noise. The allan deviation of the x-axis depicted in Figure 4.2 can be shortly fitted with the slope of the quantization noise, which indicates a marginal accuracy to the calculated error coefficient. Figure 4.3, shows that the slope of this error was instead fitted against fragments of the plot, which indicates a higher inaccuracy in the calculated error coefficient for the y-axis. The allan deviation of the z-axis can be slightly better approximated by the slope of the quantization noise, as shown in Figure 4.4. This fit only holds for larger cluster times, at which the slope can be fitted against the graph. Comparably, the calculated error coefficient of the quantization noise appears to be the most accurate for the x-axis, followed by the z- and the y-axes. Overall, this accuracy was marginal, as even the fit against the allan deviation of the x-axis indicates a certain amount of uncertainty.

The calculated random walk error coefficients in Table 4.3 all appear to be of a small value. For these values, their respective accuracy has to be considered. For all three axes, the respective Figures 4.2, 4.3, and 4.4 show that the slope of the random walk can be shortly fitted against the plot for higher cluster times. This relatively short fitting indicates some inaccuracy to the calculated coefficients; however, as the slopes are fitted generally against the actual allan deviation and not fragments in the plot, the values can be considered overall accurate.

Lastly, the white noise coefficient needs to be evaluated. All three Figures for the respective axes show that the slope of the white noise can be fitted the best against the allan deviation compared to the other slopes, and this indicates a high accuracy for the calculated error coefficients for each axes.

Magnetometer Similarily, the BNO055 magnetometer allan deviation was evaluated. Figure 4.5 depicts the allan deviation for the three magnetometer axis.

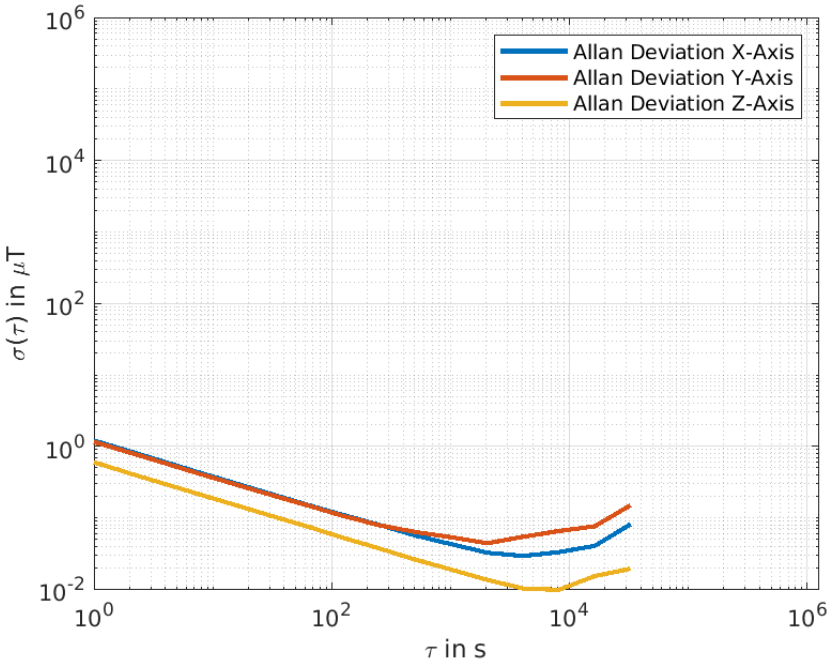

Figure 4.5: Allan deviation of the BNO055 magnetometer

The x- and y-axis are close together for almost all cluster times and only split up in higher cluster times. The z-axis, which appears lower on the graph, runs almost parallel to the x- and y-axis, but it does show an additional kink compared to the two.

Figure 4.6 shows the closer evaluation of the x-axis of the magnetometer.

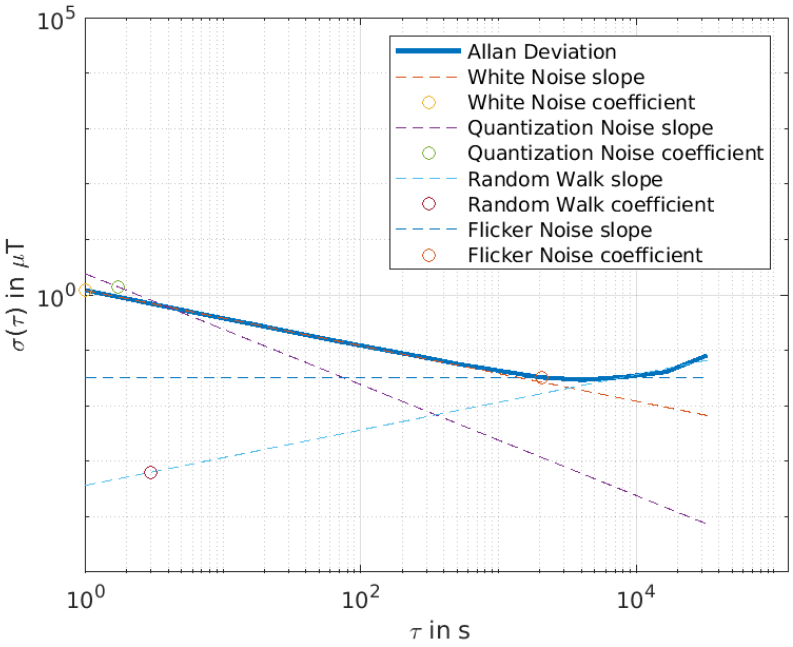

Figure 4.6: Allan deviation of the BNO055 magnetometer on the x-axis

The white noise error seems to be the dominant error source for shorter cluster times. However, this dominance does change at higher cluster times, when first the flicker noise, and then soon after the random walk becomes the dominant error source. While represented in the graph as a line with a slope of -1, the quantization noise barely influences the measurements of the x-axis of the magnetometer.

Plot 4.7 shows the allan deviation of the y-axis of the magnetometer.

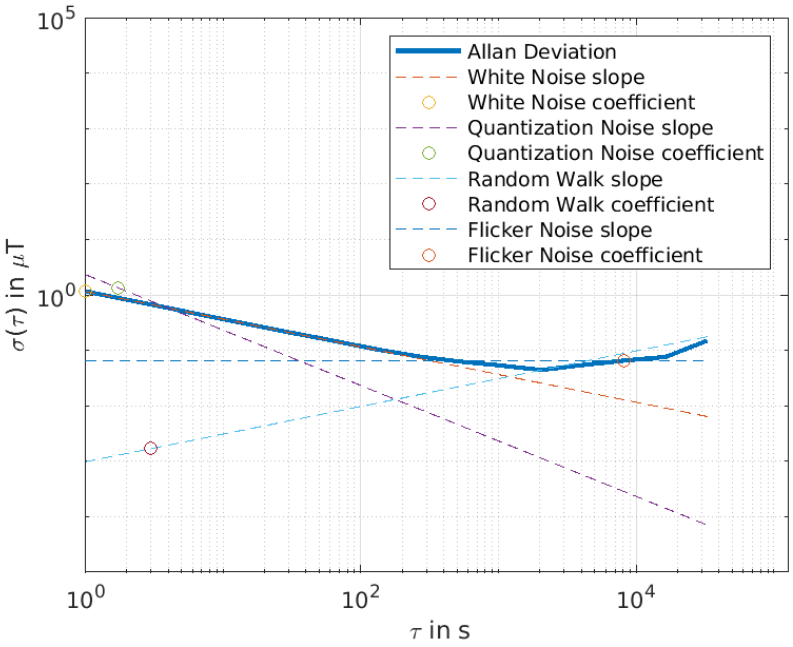

Figure 4.7: Allan deviation of the BNO055 magnetometer on the y-axis

Similar to the x-axis, the measurements in Figure 4.7 are influenced by the random walk or the white noise at low cluster times, while the main error source was later attributed to the flicker noise and then the random walk. Again, the quantization noise barely influences the measurements.

Figure 4.8 depicts the plot for the allan deviation at the z-axis of the magnetometer.

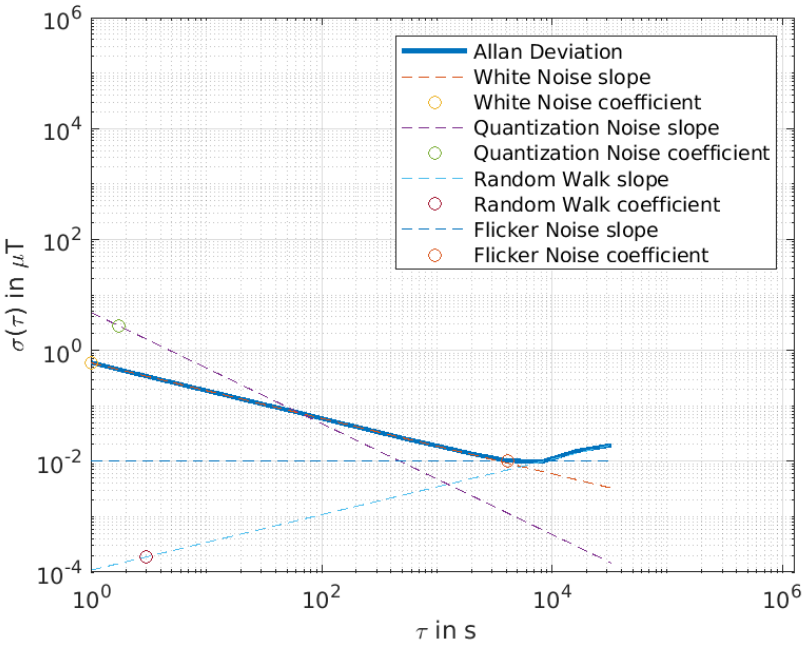

Figure 4.8: Allan deviation of the BNO055 magnetometer on the z-axis

The primary influence at shorter cluster times stems from the white noise, while now, at higher cluster times, the random walk more substantially impacts the measurements. Neither the quantization noise nor the flicker noise strongly affects the measurements.

Table 4.4 gathers all the calculated error coefficients for the magnetometer of the BNO055.

Axis	**Quantization noise in µT/$\sqrt{\text{Hz}}$**	**White noise in µT/$\sqrt{\text{Hz}}$**	**Flicker noise in µT**	**Random walk in µT/$\sqrt{\text{Hz}}$**
x-axis	1.3858	1.2057	0.048810	0.00063294
y-axis	1.3352	1.1557	0.098254	0.0016865
z-axis	2.7579	0.5924	0.015409	0.00018817

Table 4.4: Error coefficients BNO055 magnetometer

The coefficients calculated for the random walk appear to be the smallest values in Table 4.4, with the x- and z-axes being significantly smaller than the value calculated for the y-axis. All three axes in the Figures 4.6, 4.7, and 4.8 show that the slope of the random walk can be fitted against the calculated allan deviation. For the y-axis, it can

be seen in Figure 4.7 that the slope was fitted against rather short sections of the allan deviation, in comparison to the other axes. This fit indicates that the overall accuracy of the calculated value for the y-axis was relatively low compared to the other two axes. These seem to allow for a better fit of the random walk slope, though only a small section allows for this fit.

The next smallest overall error coefficient are the values calculated for the flicker noise. Here, the value calculated for the y-axis appears to be the biggest out of the three axes, while the z-axis appears to have the lowest flicker noise coefficient. The x- and the z-axis shown in their respective Figures a relatively good fitting of the flicker noise slope, which deems the calculated values relatively accurate. The y-axis, however, shows a worse fit of the slope, which indicates that the higher error coefficient might stem from a higher inaccuracy of the fitting.

As the next error coefficient, the white noise is analyzed. It can be seen that the values calculated for the x- and y-axis are comparable to each other, while the z-axis appears to have a smaller error coefficient. Considering the respective Figures 4.6, 4.7, and 4.8, it can be seen that the slope for all three axes can be fitted well against the respective plots. This indicates a high accuracy for the calculated error coefficients for all three axes. The lower value for the z-axis compared to the other two axes indicates that the white noise influenced the z-axis less.

The last error coefficients to be considered are the coefficients calculated for the quantization noise. The calculated values for the x- and y-axes are relatively close to each other, while the coefficient for the z-axis lies above the previous two axes. To evaluate the accuracy of the coefficients, the respective plots are considered. It can be seen in the Figures 4.6, 4.7, and 4.8 that for all three axes, the slope of the quantization noise was only fitted against a fragment of the allan deviation. This fit indicates that the calculated error coefficients are relatively inaccurate.

PSD Verification

Gyroscope Next, the PSD of the BNO055 was evaluated. This yielded the plot shown in Figure 4.9 for all three gyroscope axes.

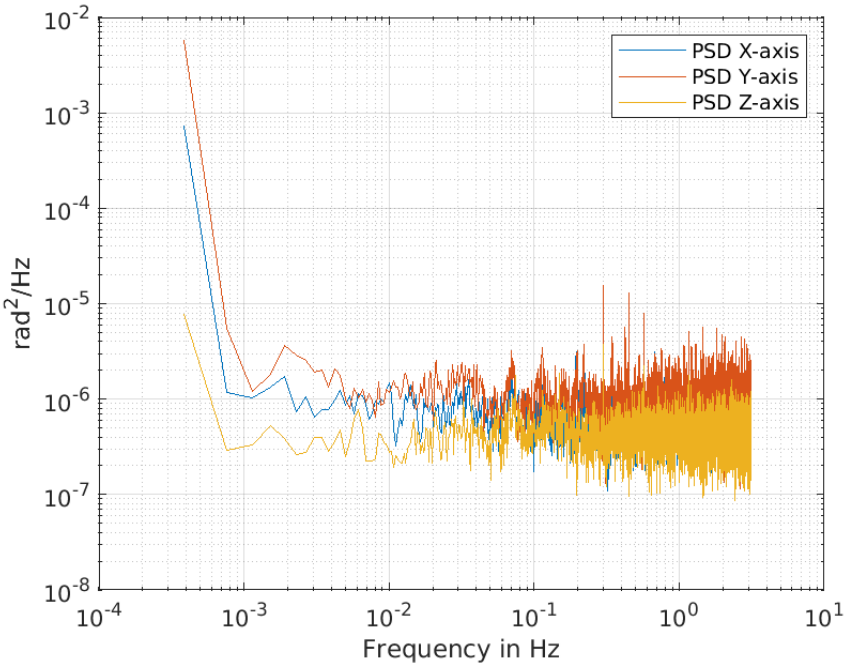

Figure 4.9: PSD of the BNO055 gyroscope

Fitting lines against the respective axes plot resulted in graphs as shown Figure 4.10 for the x-axis.

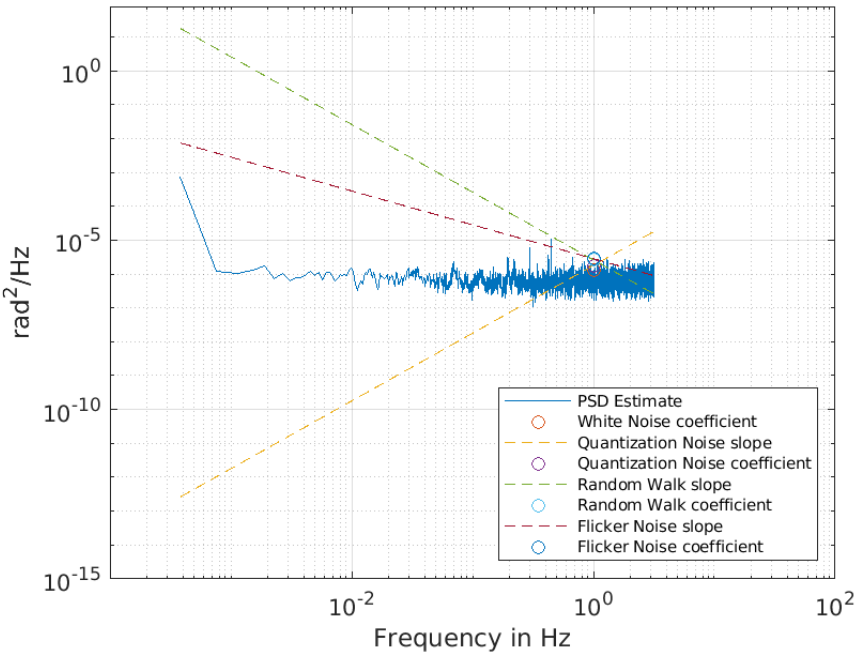

Figure 4.10: Analyzed PSD of the BNO055 gyroscope x-axis

Figure 4.10 shows, that the PSD estimate levels quickly.

The remaining axes appear to behave similarly, as also visible in Figure 4.9. The plots with the fitted lines can be found in the digital appendix of this thesis.

Concrete error values calculated by the PSD method can be found in Table 4.5.

Axis	**Quantization noise in** $(\mathrm{rad/s})/\sqrt{\mathrm{Hz}}$	**White noise in** $(\mathrm{rad/s})/\sqrt{\mathrm{Hz}}$	**Flicker noise in** $(\mathrm{rad/s})$	**Random walk in** $(\mathrm{rad/s})/\sqrt{\mathrm{Hz}}$
x-axis	0.0013340	0.0011334	0.0016808	0.0016139
y-axis	0.0012262	0.0011388	0.00075143	0.0010898
z-axis	0.00057124	0.00052445	0.00087739	0.00073647

Table 4.5: Error coefficients BNO055 gyroscope calculated by PSD

The error coefficients in Table 4.5 all appear to be of similar value. Across every noise source and axis, the z-axis appears to have the lowest overall error coefficients.

Considering the error coefficients and comparing them with the achieved plot in Figure 4.10, it can be seen that the slopes for the flicker noise, white noise, and quantization

noise do not appear to be a good fit to the PSD estimate. Moreover, the best fit would be the level slope of the white noise, which was also the case for all three remaining axes.

This indicates that while the calculated values are similar for the x- and y-axes and all four error coefficients of the z-axis are relatively close to each other, only the white noise error coefficient can be seen as accurate. This observation also correlates to the allan deviation, indicating a high accuracy for the white noise error coefficient.

Table 4.6 shows the devitation of the error coefficients calculated by the PSD method and the allan deviation.

Axis	**Quantization noise difference in %**	**White noise difference in %**	**Flicker noise difference in %**	**Fandom walk Difference in %**
x-axis	-97.102	-25.157	322.12	$12.289 \cdot 10^5$
y-axis	-90.947	-39.297	892.78	$19.988 \cdot 10^4$
z-axis	-99.473	-22.536	5680.0	$38.155 \cdot 10^4$

Table 4.6: Percentual error coefficients difference between the PSD and allan deviation calculation for the BNO055 gyroscope

Table 4.6 shows that the percentual difference for the most important error coefficient of the white noise, lays under an absolute value of 50%. The differences for the quantization noise layed for all three axes at around -100%.

Alongside the previous analysis of the error coefficients, this varying deviation can be correlated to the accuracy of the calculated values. The white noise error coefficient is the most accurate, explaining why its deviations were relatively small compared to the other error coefficients. Especially the random walk error coefficient shows a high deviation, which stems from the overall uncertainty regarding this error source.

Magnetometer The PSD for the magnetometer was evaluated, which results in the Figure 4.11 for all three axes.

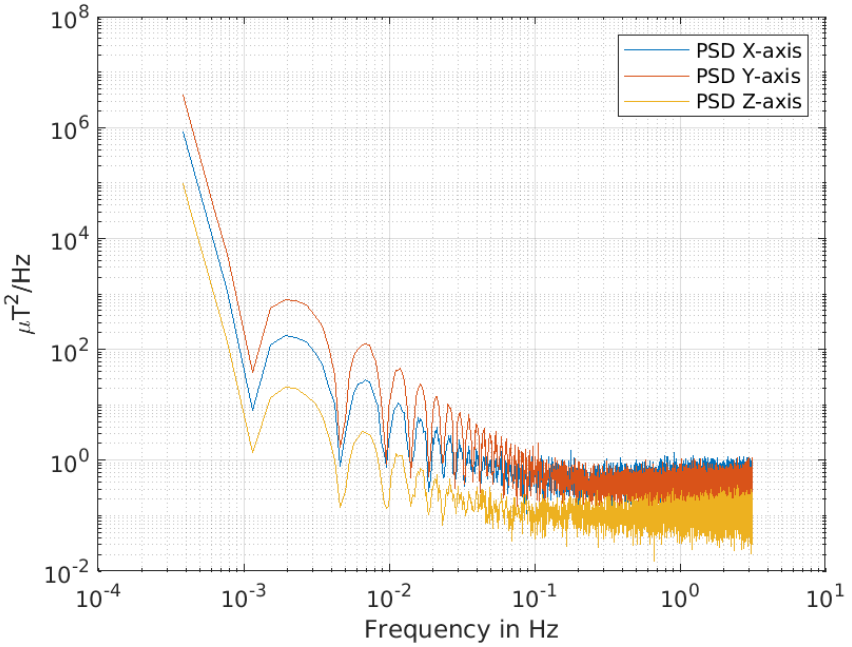

Figure 4.11: PSD of the BNO055 magnetometer

Fitting the different slopes against the PSD of the x-axis results in 4.12.

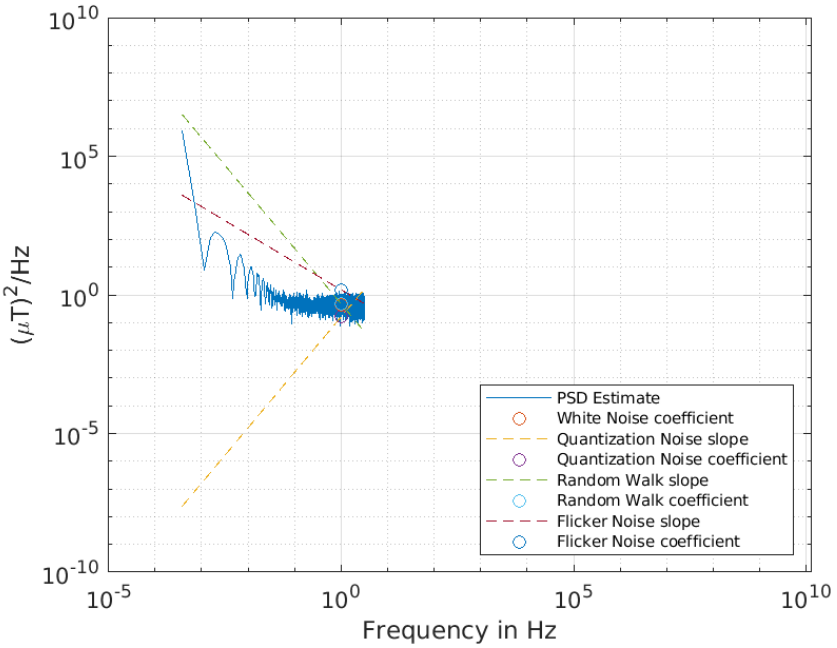

Figure 4.12: PSD of the BNO055 magnetometer x-axis

It can be seen that the plot first falls before leveling out. The initial falling could be approximated with the flicker noise; however, as seen in Figure 4.12, the appropriate slope for this error source was not directly fitted against the plot.

The remaining axes are similarly analyzed, and the plots can be found in the digital appendix of this thesis.

The calculated error coefficients of the PSD can be found in Table 4.7.

Axis	**Quantization noise in µT/$\sqrt{\text{Hz}}$**	**White noise in µT/$\sqrt{\text{Hz}}$**	**Flicker noise in µT**	**Random walk in µT/$\sqrt{\text{Hz}}$**
x-axis	0.39945	0.66296	1.2341	0.69035
y-axis	0.34001	0.72955	1.0393	0.41531
z-axis	0.23798	0.20766	0.39612	0.45296

Table 4.7: Error coefficients BNO055 magnetometer calculated by PSD

The coefficients for the x- and the y-axes are the only values that are comparably higher than the values calculated for the z-axis. Analyzing the respective plots, these higher

values most likely resulted from inaccuracies, as the slopes for the flicker noise are not exactly fit against the graph. This means that the flicker noise error coefficients can be seen as relatively inaccurate. The same can be said for the quantization noise and the random walk.

Only the coefficient was given for the white noise instead of the actual slope. It can be seen that a level plot best approximates the plot alongside the error coefficient, and this indicates a high accuracy for the calculated white noise error coefficient.

The concrete percentual differences between the error coefficients calculated by the PSD and the allan deviation can be see in Table 4.8.

Axis	Quantization noise difference in %	White noise difference in %	Flicker noise difference in %	Random walk difference in %
x-axis	-71.176	-45.013	2428.4	108970
y-axis	-74.535	-36.872	957.77	24526
z-axis	-91.371	-64.946	2470.6	240616

Table 4.8: Percentual error coefficients difference between the PSD and allan deviation calculation for the BNO055 magnetometer

Table 4.8 shows, that the percentual differences between the white noise calculated by the allan deviation and PSD lays under the absolute value of 50% for the x- and the y-axis, with the z-axis depicting a higher absolute value.

This relatively small deviation for the white noise error coefficient was consistent with the observation that these coefficients could be accurately calculated by both the PSD and the allan deviation. The higher percentual deviations in Table 4.8 stem from the initial uncertainty, which was detected for the respective analysis of the error coefficients.

Separate Sensor Verification

Gyroscope Compared with another BNO055, the relevant error noise values, the white noise, only deviate slightly. The percentual differences between the error coefficients can be seen in Table 4.9.

Axis	Quantization noise difference in %	White noise difference in %	Flicker noise difference in %	Random walk difference in %
x-axis	-98.710	-30.732	-93.823	236.72
y-axis	-95.104	-44.436	-38.394	0.81203
z-axis	-86.597	-22.536	3.8560	46.875

Table 4.9: Percentual error coefficients difference between two BNO055 gyroscopes

The most relevant values are the white noise and the random walk. The white noise appears to be consistent for the x- and z-axis, while the random walk was the most stable for the y- and then the z-axis. The x-axis experiences a difference for the random walk at just over 100%, which can not be fully explained. Considering that the white noise error deviates less than 50% for the x-axis, this drastic change for the random walk was considered to be surprising. Besides this occurrence, the error values appear to be stable, deeming the two BNO055s as comparable.

Magnetometer The differences of the magnetometers between two BNO055 sensors are gathered in Table 4.10.

Axis	Quantization noise difference in %	White noise difference in %	Flicker noise difference in %	Random walk difference in %
x-axis	10.227	-45.139	958.19	-28.242
y-axis	79.143	-36.628	-31.366	44.791
z-axis	94.417	32.423	98.943	$36.735 \cdot 10^4$

Table 4.10: Percentual error coefficients difference of two BNO055 magnetometers

Table 4.10 shows that the absolute difference in the random walk coefficient was below 40% for the x- and y-axes, while the z-axes show a bigger deviation. The differences calculated for the white noise are also quite significant and not to be neglected. The y- and z-axes appear to be stable regarding this error coefficient, both deviating under 50%. The x-axis deviates slightly above this value. Overall, the BNO055s appear to be comparable.

4.3.2 LSM9DS1

Allan Deviation

Gyroscope Figure 4.13 shows the log-log plot of the allan deviation of all three axes of the LSM9DS1 gyroscope.

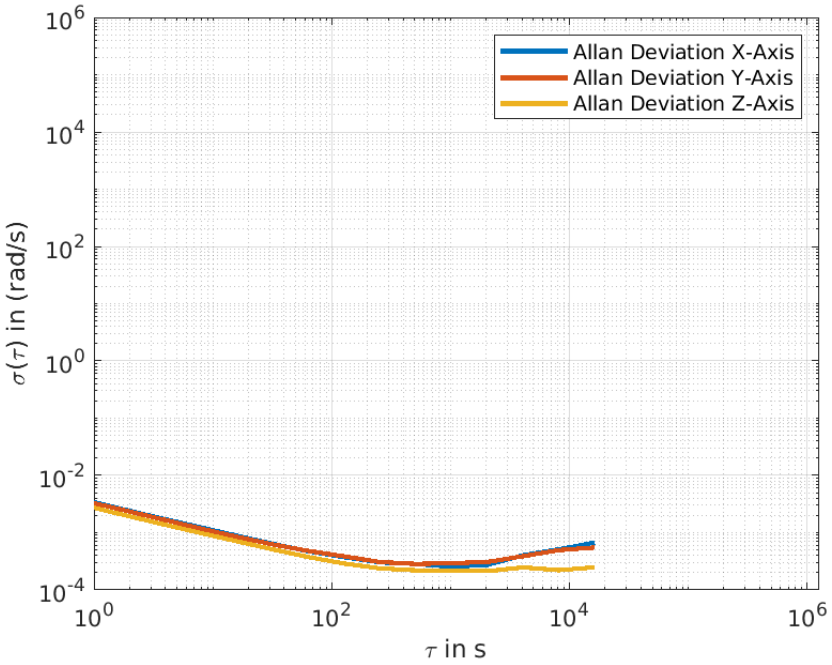

Figure 4.13: Allan deviation of the LSM9DS1 gyroscope

It can be seen that all three axes can first be approximated by a line with a slope of $-1/2$ before leveling out. This falling slope stems from the white noise, while the flicker noise causes the leveling of the walk. The x- and y-axes then clearly rise again with a slope of approximately $1/2$, which indicates the presence of the random walk.

The allan deviation for the gyroscope was evaluated for all three axes by fitting the appropriate slopes against the allan deviation. The analysis of the x-axis of the LSM9DS1 gyroscope is shown in Figure 4.14.

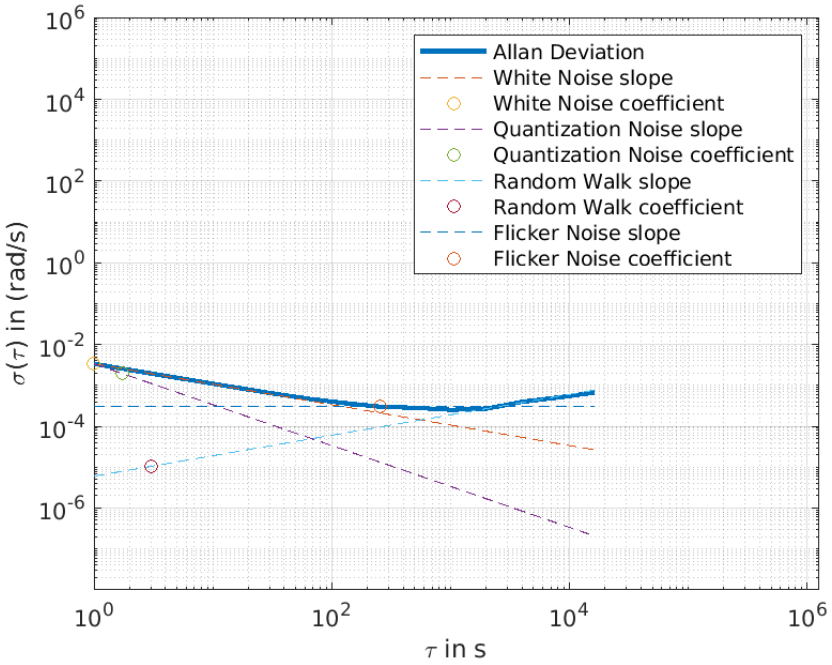

Figure 4.14: Allan deviation of the LSM9DS1 gyroscope on the x-axis

It can be seen in Figure 4.14 that the slope of the white noise first approximated the allan deviation of the x-axis, then the flicker noise as well as the random walk for higher cluster times.

As the allan deviation of the y-axis behaves in a comparably similar manner to the allan deviation of the x-axis, this plot is omitted here, and the reader is referenced to the digital appendix of this thesis.

The analysis of the z-axis of the LSM9DS1 gyroscope is shown in Figure 4.15.

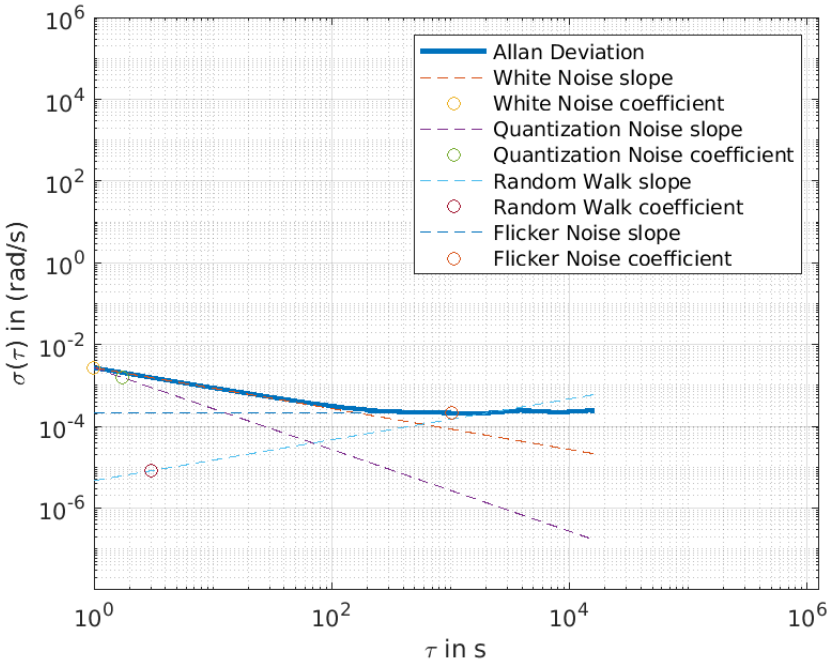

Figure 4.15: Allan deviation of the LSM9DS1 gyroscope on the z-axis

Figure 4.15 shows that the allan deviation of the z-axis can first be approximated by the slope of the white noise before the slope of the flicker noise appears to be a closer fit.

The error coefficients calculated for the LSM9DS1 gyroscope are listed in Table 4.11.

Axis	**Quantization noise in** $(\mathrm{rad/s})/\sqrt{\mathrm{Hz}}$	**White noise in** $(\mathrm{rad/s})/\sqrt{\mathrm{Hz}}$	**Flicker noise in** $(\mathrm{rad/s})$	**Random walk in** $(\mathrm{rad/s})/\sqrt{\mathrm{Hz}}$
x-axis	0.0019555	0.0033869	0.00045392	$1.0430 \cdot 10^{-5}$
y-axis	0.0026892	0.0032936	0.00042520	$1.0454 \cdot 10^{-5}$
z-axis	0.0015642	0.0027094	0.00031994	$8.1093 \cdot 10^{-6}$

Table 4.11: Error coefficients LSM9DS1 gyroscope

Table 4.11 shows the random walk as the error source with the lowest error coefficient over the three axes. Figure 4.14 shows that the allan deviation of the x-axis appears to be a good fit for the slope of the random walk for higher values. As described and also depicted in Figure 4.13, the allan deviation of the y-axis behaves similarly to the x-axis deviation. This behavior explains why the calculated coefficients for the x- and y-axis appear to be almost equivalent in Table 4.11. The z-axis, on the other hand, can

barely be fitted by the slope of the random walk as seen in Figure 4.15. While the calculated error coefficient of the random walk for the z-axis in Table 4.11 appears to be the smallest value, this might be due to inaccuracies in the analysis.

The error coefficients of the flicker noise appear to be the following highest error coefficients in the Table 4.11. The values for the x- and y-axes can be seen as very similar, while the z-axis depicts a slightly smaller value. Comparing the coefficients with their respective Figures 4.14, 4.15, and 4.13, it can be seen that the allan deviations of all three plots can be evaluated with the slope of the flicker noise. This indicates that the calculated coefficients can be seen as comparably accurate.

The next highest error coefficients in Table 4.11 is the quantization noise. Here, the values calculated for the x- and z-axes appear relatively close to each other, with the y-axis depicting the highest value. It has to be noted that none of the graphs for the respective axes show a proper fitting of the quantization noise slope. This indicates the high accuracy of the calculated values for all three axes.

Finally, the coefficients of the white noise are analyzed further. It can be seen that the values for the x- and the y-axes appear to be similar, which could already be seen for the previous error coefficients. The z-axis shows a slightly lower error coefficient for the white noise. As seen in the respective Figures 4.14, 4.15, and 4.13, the allan deviation of all three axes can be well approximated with the slope of the white noise. This indicates that the calculated error coefficients are relatively accurate.

Magnetometer Next, the LSM9DS1 magnetometer was evaluated, which resulted in the plot shown in Figure 4.16.

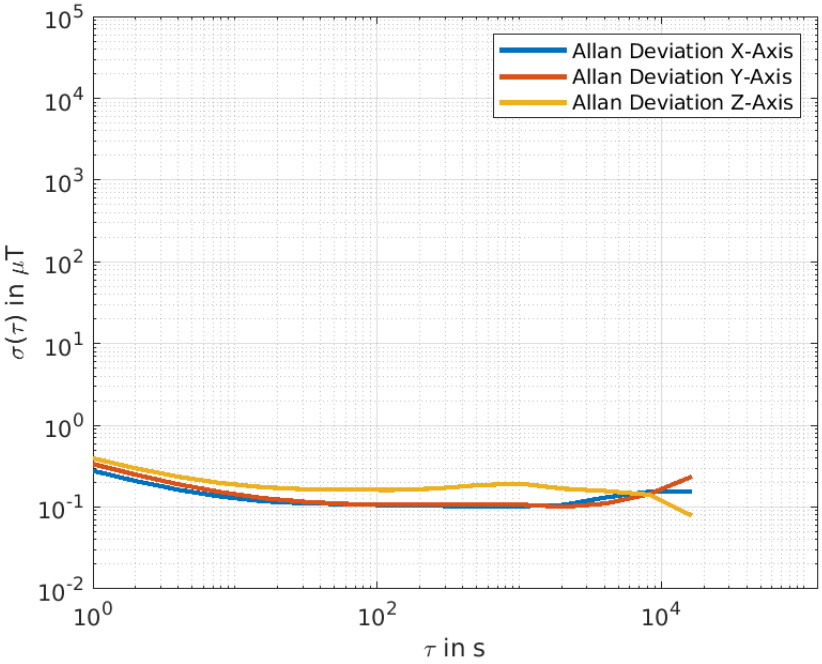

Figure 4.16: Allan deviation of the LSM9DS1 magnetometer

All three axes first slightly fall with a slope of $-1/2$, which indicates the presence of the white noise, before roughly leveling out, which indicates the presence of the flicker noise. Finally, the y-axis rises with a slope of $1/2$, caused by the random walk, while the z-axis shortly falls with a slope of roughly -1, which the quantization noise might cause.

Figure 4.17 depicts the allan deviation for the x-axis of the LSM9DS1 magnetometer.

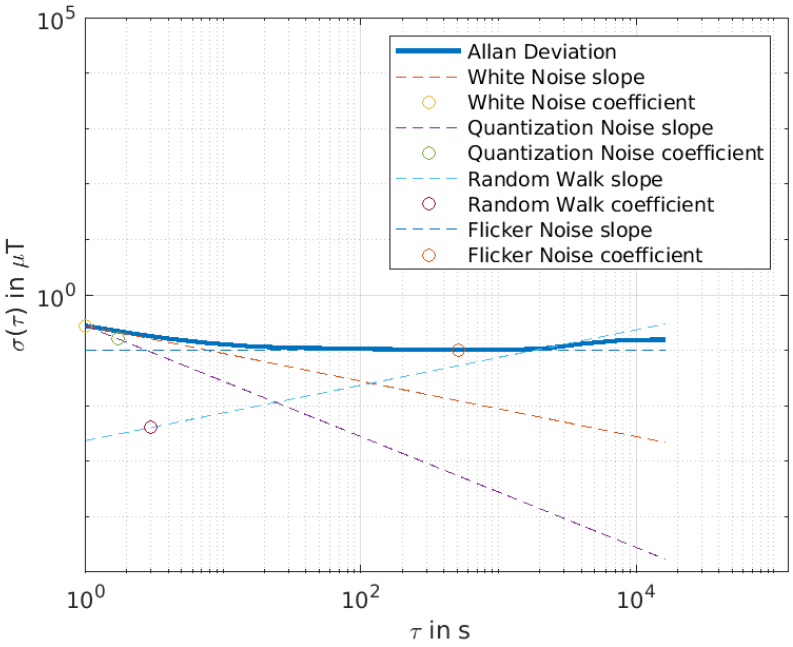

Figure 4.17: Allan deviation of the LSM9DS1 magnetometer x-axis

As seen in Figure 4.16, this axis behaves similarly for the y-axis, which is why this allan deviation can be seen as similar to the calculated allan deviation of the y-axis. The actual plot for this can be found in the digital appendix of this thesis. The z-axis of the LSM9DS1 magnetometer can be seen to deviate from the two previous axes in Figure 4.16. For further analysis of the accuracy of the calculated error coefficients, the allan deviation of the z-axis can be seen in Figure 4.18.

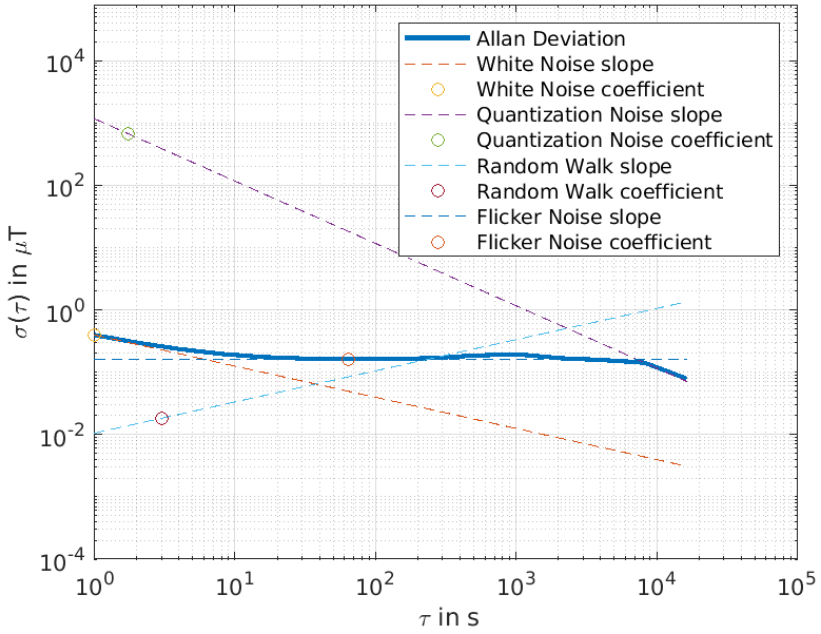

Figure 4.18: Allan deviation of the LSM9DS1 magnetometer z-axis

Table 4.12 shows the calculated values of the LSM9DS1 magnetometer.

Axis	**Quantization noise in µT/$\sqrt{\text{Hz}}$**	**White noise in µT/$\sqrt{\text{Hz}}$**	**Flicker noise in µT**	**Random walk in µT/$\sqrt{\text{Hz}}$**
x-axis	0.16029	0.27762	0.15262	0.0040556
y-axis	0.19380	0.33568	0.16374	0.0029923
z-axis	670.53	0.394803	0.24484	0.018179

Table 4.12: Error coefficients LSM9DS1 magnetometer

Table 4.12 shows the random walk error coefficients to have the lowest overall value amongst the calculated values. The values for the x- and y-axes are roughly comparable, with the value for the z-axis being slightly higher. Analyzing the respective Figures 4.16, 4.17, and 4.18, it can be seen that the slope of the random walk was fitted against small fragments of the plots, rather than an accurate fit. This indicates that the calculated values are to be considered relatively inaccurate.

Next, the flicker noise error coefficients are evaluated. It can be seen that the values for

the x- and y-axes only deviate slightly from each other, while the value for the z-axis lays slightly above the two other axes. Considering the respective Figures, it can be seen that the slope of the flicker noise appears to be a comparably good fit to the allan deviation in comparison to the random walk slope. This fit indicates that the calculated values can be considered to be accurate.

The next highest values for the x- and y-axes can be found in the error coefficients of the quantization Noise. It can immediately be seen that the error coefficient of the z-axis appears to be high. Together with Figure 4.18, it can be concluded that this error coefficient was relatively inaccurate due to its short fit against the depicted allan deviation. While the two other values for the x- and y-axes appear to be more realistic, the respective Figures 4.16 and 4.17 show that the slope of the quantization noise is only being fitted against fragments of the graph. This indicates that the calculated values are relatively inaccurate.

Lastly, the white noise error coefficients are evaluated. It can be seen for that x- and y-axis in Figures 4.16 and 4.17 that the slope of the white noise does not appear to be a good fit to the allan deviation. A similar observation can be made for the z-axis in Figure 4.18, and this indicates that the calculated values for the axes are inaccurate.

PSD Verification

Gyroscope The evaluation of the gyroscope continued with the execution of the PSD. This yielded the plot as shown in Figure 4.19 for all three axes.

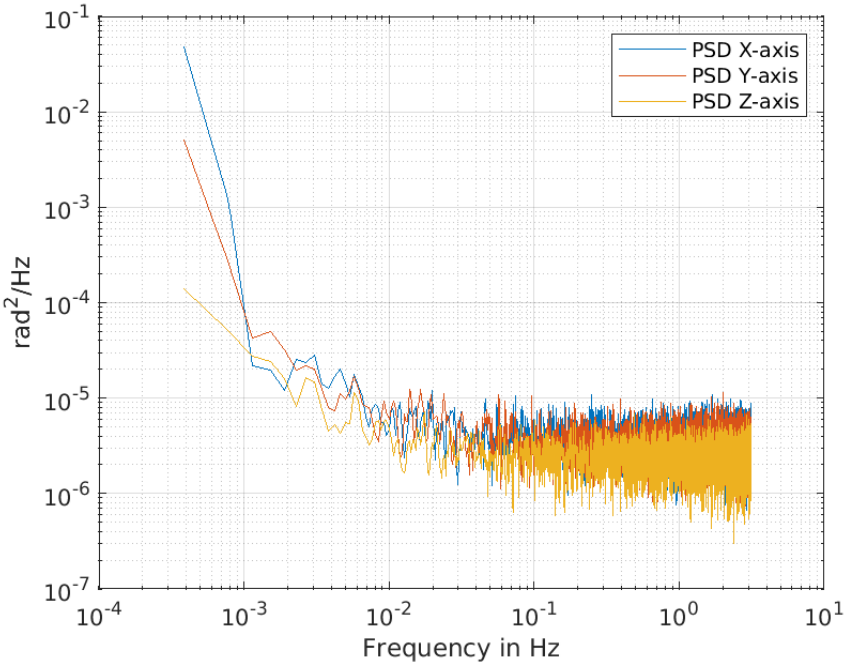

Figure 4.19: PSD of the LSM9DS1 gyroscope

Figure 4.19 shows that all three axes behave similarly. While the axes first fall at a slope of approximately -1, they then level out.

In order to evaluate the error coefficients, lines were fitted against the respective axes plot, which resulted in graphs as shown Figure 4.20.

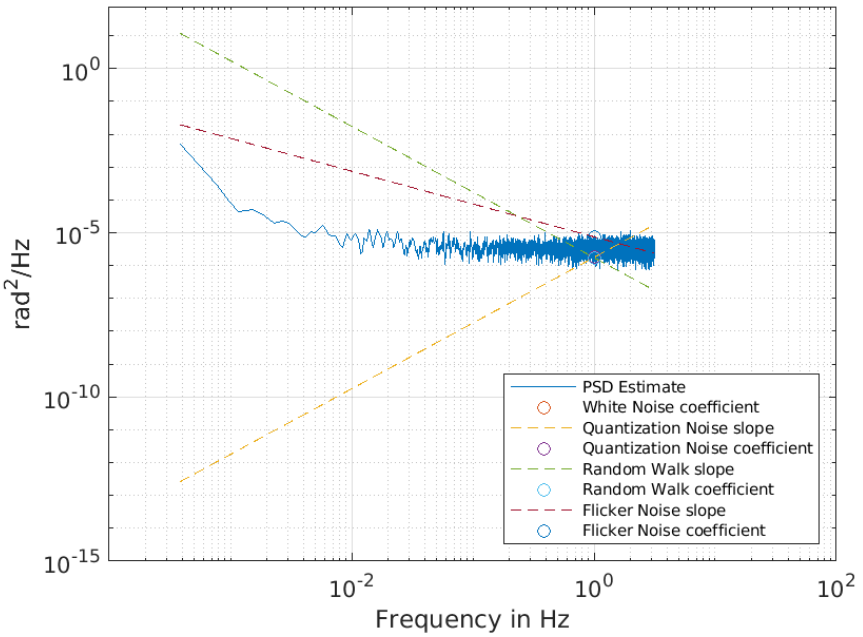

Figure 4.20: Analyzed PSD of the LSM9DS1 gyroscope y-axis

It can be seen in Figure 4.20 that the graph quickly levels out, which indicates a strong presence of the white noise error. Similar plots can also be seen for the remaining axes, which can be found in the digital appendix of this thesis.

The concrete error values for all three axes are shown in Table 4.13.

Axis	**Quantization noise in** $(\mathrm{rad/s})/\sqrt{\mathrm{Hz}}$	**White noise in** $(\mathrm{rad/s})/\sqrt{\mathrm{Hz}}$	**Flicker noise in** $(\mathrm{rad/s})$	**Random walk in** $(\mathrm{rad/s})/\sqrt{\mathrm{Hz}}$
x-axis	0.0013966	0.0020266	0.0027275	0.0028852
y-axis	0.0013254	0.0013326	0.0027305	0.0013172
z-axis	0.0010078	0.0022321	0.0022402	0.00073182

Table 4.13: Error coefficients LSM9DS1 gyroscope calculated by PSD

Out of the slopes of the PSD, only the level slope of the white noise could be a good approximation for the PSD estimate. This indicates, that only the calculated values for the white noise shown in Table 4.13 can be considered to be accurate.

The error coefficients were then compared to the coefficients calculated by the allan deviation and the percentual differences are displayed in Table 4.14.

Axis	Quantization noise difference in %	White noise difference in %	Flicker noise difference in %	Random walk difference in %
x-axis	-28.580	-40.163	500.89	27562
y-axis	-50.713	-59.538	542.16	12500
z-axis	-35.572	-17.614	600.20	8924.4

Table 4.14: Percentual error coefficients difference between the PSD and allan deviation calculation for the LSM9DS1 gyroscope

The deviation of the white noise errors lies at an absolute value of around 50%, while this deviation was significantly lower for the z-axis. The quantization noise deviation was roughly comparable to the white noise deviation. This deviation indicates that these two errors can also be evaluated using the PSD. The remaining error coefficients, however, deviate significantly.

The low deviation of the White Angle error coefficients indicates that both the allan deviation and the PSD accurately calculate this coefficient. The slight deviation of the quantization noise could not be explained, as it had been declared to be inaccurate in the previous analysis.

Magnetometer Next, the PSD was executed on the magnetometer of the LSM9DS1 sensor. This resulted in the plot shown in Figure 4.21.

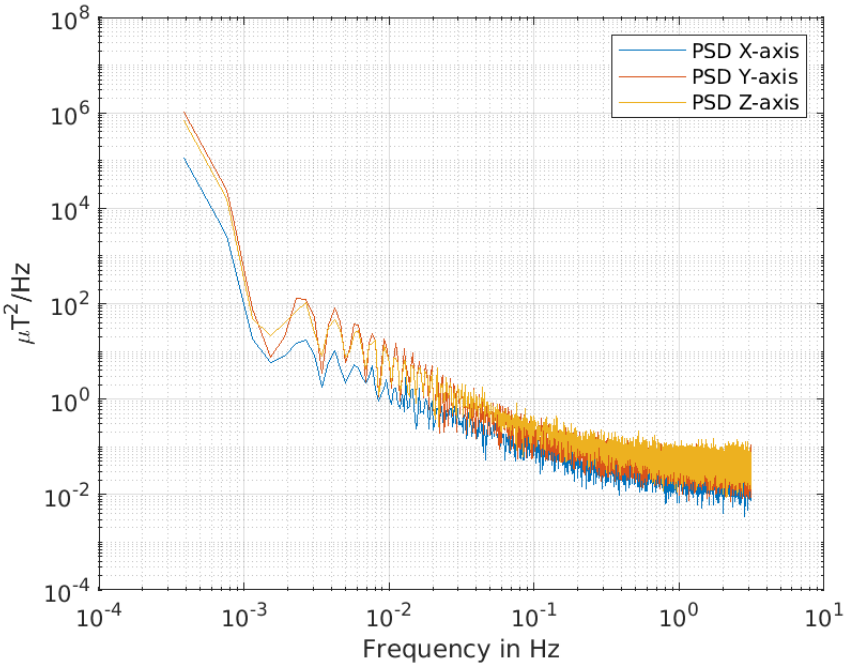

Figure 4.21: PSD of the LSM9DS1 magnetometer

Figure 4.21 shows that all three axes behave similarly. While the plots are first falling at a slope of approximately -1, they continue to level out.

In order to evaluate the error coefficients, lines were fitted against the respective axes plot, which resulted in graphs as shown in Figure 4.22.

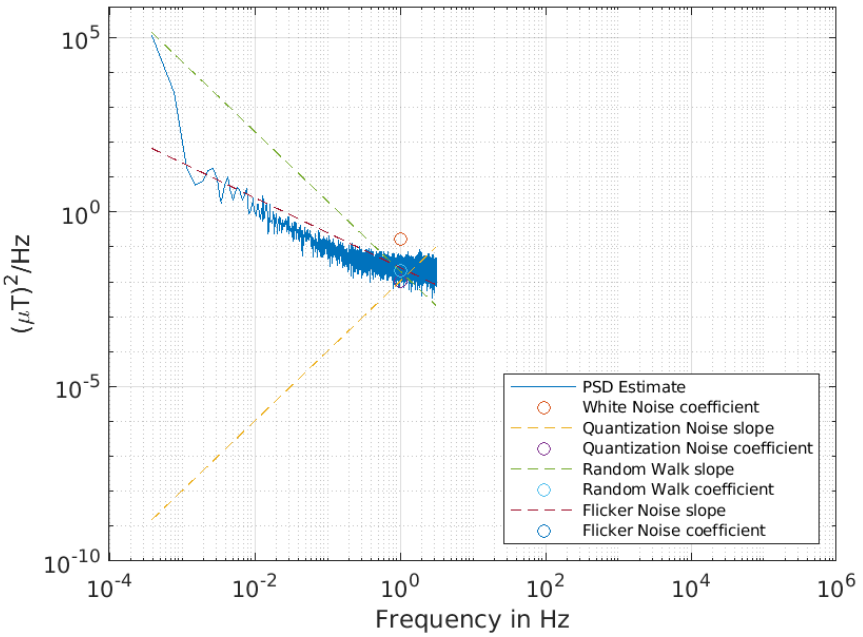

Figure 4.22: Analyzed PSD of the LSM9DS1 magnetometer x-axis

The plot in Figure 4.22 can be seen as similar for the y- and z-axes, which appear to be similar to the x-axis as depicted in Figure 4.21. The actual plots for these axes can be found in the digital appendix.

The respective calculated values can be found in Table 4.15.

Axis	**Quantization noise in µT/$\sqrt{\text{Hz}}$**	**White noise in µT/$\sqrt{\text{Hz}}$**	**Flicker noise in µT**	**Random walk in µT/$\sqrt{\text{Hz}}$**
x-axis	0.10105	0.40457	0.16019	0.14324
y-axis	0.19711	0.23404	0.21545	0.27898
z-axis	0.18048	0.23969	0.39461	0.14215

Table 4.15: Error coefficients LSM9DS1 magnetometer calculated by PSD

Evaluating the calculated plots, which are represented as Figure 4.21, it can be seen that only the slope for the flicker noise appears to be a good fit for the PSD estimate. This observation indicates that only the error coefficients calculated for the flicker noise should be seen as accurate, while the other coefficients should be neglected.

The percentage differences between the error coefficients calculated by the allan deviation and PSD are gathered in Table 4.16.

Axis	Quantization noise difference in %	White noise difference in %	Flicker noise difference in %	Random walk difference in %
x-axis	-36.955	45.726	4.9629	3431.8
y-axis	1.7047	-30.279	31.582	9223.0
z-axis	-99.973	-39.290	61.173	681.95

Table 4.16: Percentual error coefficients difference between the PSD and allan deviation calculation for the LSM9DS1 magnetometer

Table 4.16 shows that the deviation of the flicker noise calculated by the allan deviation and the PSD was relatively low, especially for the x-axis. This indicates that these values could be accurately calculated.

The white noise error coefficients also appear only to deviate slightly, which can not be explained, as the PSD analysis deemed the values calculated through the PSD estimate to be relatively inaccurate.

It can also be seen that the deviations of the quantization noise coefficients between the two methods enormously vary between the axes. This, however, supports the claim that these values are relatively inaccurate, as they appear to deviate randomly.

Lastly, the random walk difference can be considered to be high, indicating a strong deviation and, therefore, inaccuracy between the two used calculation methods.

Separate Sensor Verification

Gyroscope Compared with another LSM9DS1, the relevant error noise values only deviate slightly. The percentual differences between the error coefficients can be seen in Table 4.17.

Axis	Quantization noise difference in %	White noise difference in %	Flicker noise difference in %	Random walk difference in %
x-axis	-6.834	-6.834	-3.6697	31.148
y-axis	101.78	0.89059	-6.0307	-44.929
z-axis	0.91975	0.91975	-7.0026	-56.716

Table 4.17: Percentual error coefficients difference LSM9DS1 gyroscopes

As described, the white noise is the most accurately determinable error source for the

LSM9DS1 gyroscope, which was why its deviation between two LSM9DS1 gyroscopes had to be monitored. For the y- and z-axes, this deviation is at under 1%, while the x-axis deviation is set at just over 7%. The flicker noise deviation is the next important error coefficient, which deviates at just over 5% for the y- and z-axes, while the x-axis deviation lies at under 4%. Considering these numbers as shown in Table 4.17, the overall deviation between two different LSM9DS1 gyroscopes is seen as only marginal.

Magnetometer Table 4.18 shows the percentual differences between the magnetometers of two LSM9DS1 sensors.

Axis	Quantization noise difference in %	White noise difference in %	Flicker noise difference in %	Random walk difference in %
x-axis	$94.537 \cdot 10^4$	0.18792	0.9648	-39.605
y-axis	$82.933 \cdot 10^4$	-17.969	6.9563	36.075
z-axis	-99.954	34.227	2.9365	-86.648

Table 4.18: Percentual error coefficients difference LSM9DS1 magnetometer

In Table 4.18, it can be seen that the percentual differences are low for all three axes, especially for the x-axis with a deviation of under 1%. The white noise error coefficient is the next most influential error coefficient for all three axes. Here, the deviation between the two sensors lies at under 30% for all three axes. Similar to the flicker noise, the x-axis deviates less than 1%. The last important error coefficient is the random walk for the x- and y-axis. Here, the values deviate at just under 50% between the two sensors. Considering how this error is the least influential, this rather high deviation can be neglected to a certain degree. This observation concludes that the general deviation between the error coefficients measured between two LSM9DS1 magnetometers can be considered marginal.

4.3.3 ICM20948

Allan Deviation

The allan deviation executed on the ICM20948 gyroscope results in the graph as shown in Figure 4.23.

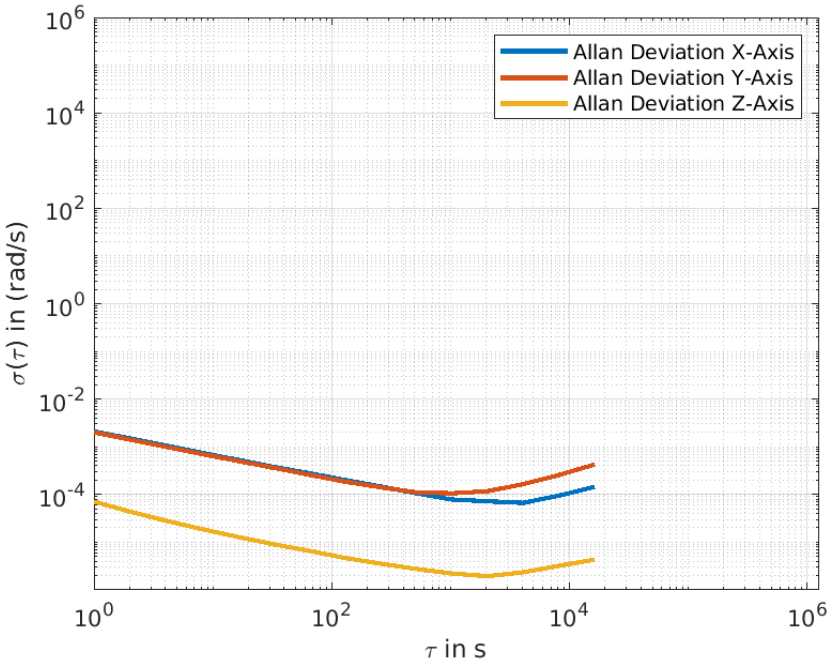

Figure 4.23: Allan deviation of the ICM20948 gyroscope

All three axes behave approximately similarly, first falling with a slope of roughly $-1/2$, which indicates the presence of the white noise. All three axes shortly level out before rising again, which indicates the influence of both the quantization noise and the random walk. The z-axis is notably below the two other axes.

To further evaluate the calculated error coefficients depicted later in this section, the allan deviation of the x-axis can be seen in Figure 4.24.

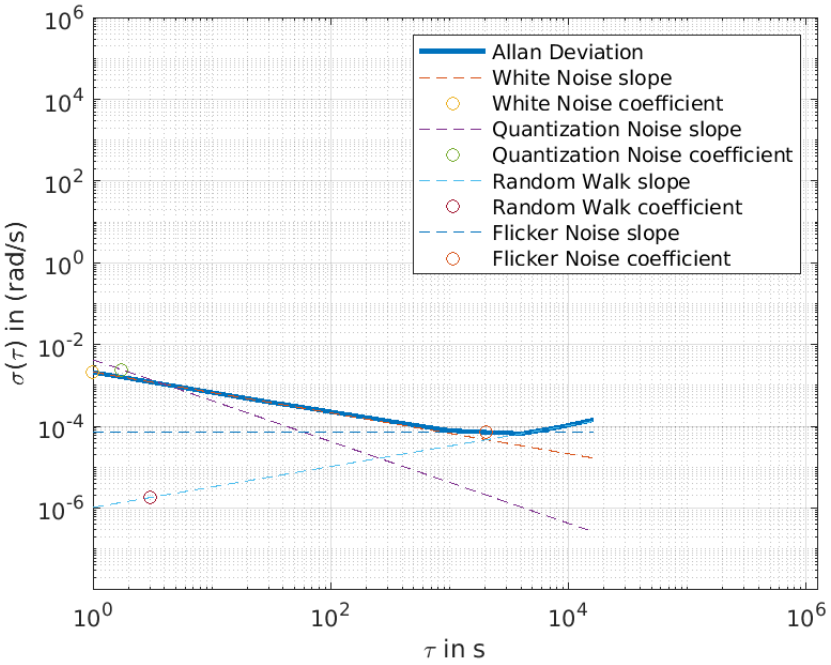

Figure 4.24: Allan deviation of the ICM20948 gyroscope x-axis

As depicted in Figure 4.23, all three axes show a rather similar allan deviation, which is why Figure 4.24 can be seen as an analysis of the allan deviation of all three axes for the ICM20948 gyroscope.

The error coefficients were calculated for the ICM20948 gyroscope and gathered in Table 4.19.

Axis	**Quantization noise in** $(\mathrm{rad/s})/\sqrt{\mathrm{Hz}}$	**White noise in** $(\mathrm{rad/s})/\sqrt{\mathrm{Hz}}$	**Flicker noise in** $(\mathrm{rad/s})$	**Random walk in** $(\mathrm{rad/s})/\sqrt{\mathrm{Hz}}$
x-axis	0.0024547	0.0021258	0.00010799	$1.7954 \cdot 10^{-6}$
y-axis	0.0011584	0.0020037	0.00016730	$4.4752 \cdot 10^{-6}$
z-axis	$4.0926 \cdot 10^{-5}$	$5.2654 \cdot 10^{-5}$	$3.3104 \cdot 10^{-6}$	$6.2968 \cdot 10^{-8}$

Table 4.19: Error coefficients ICM20948 gyroscope

It can be seen in Table 4.19, that the z-axis seems to be extremely noise free, as all error coefficients are close to 0.

The random walk error appears to have the smallest value for all three axes in Table

4.19. Considering the plots in Figures 4.23 and 4.24, it can be seen that the slope of the random walk appears to be a good fit for the allan deviation. This may indicate that the calculated error coefficients are relatively accurate.

Next, the flicker noise coefficients are slightly higher than the previously discussed random walk coefficients for all three axes. Considering the respective figures, it can be seen that the slope of the flicker noise is instead fitted to small fragments of the allan deviation, which indicates an inaccuracy considering the calculated error coefficients.

A similar observation can be made for the quantization noise coefficients, which appear to result from an inaccurate fit of the respective slope. This deems the calculated values to be inaccurate.

Finally, the white noise error coefficients are analyzed. It can be seen, that the slope of the white noise is a good fit for the respective axes, which indicates the calculated values to be accurate.

PSD Verification

For further analysis, the PSD was also executed on the ICM20948 gyroscope. This resulted in the plot as shown in Figure 4.25.

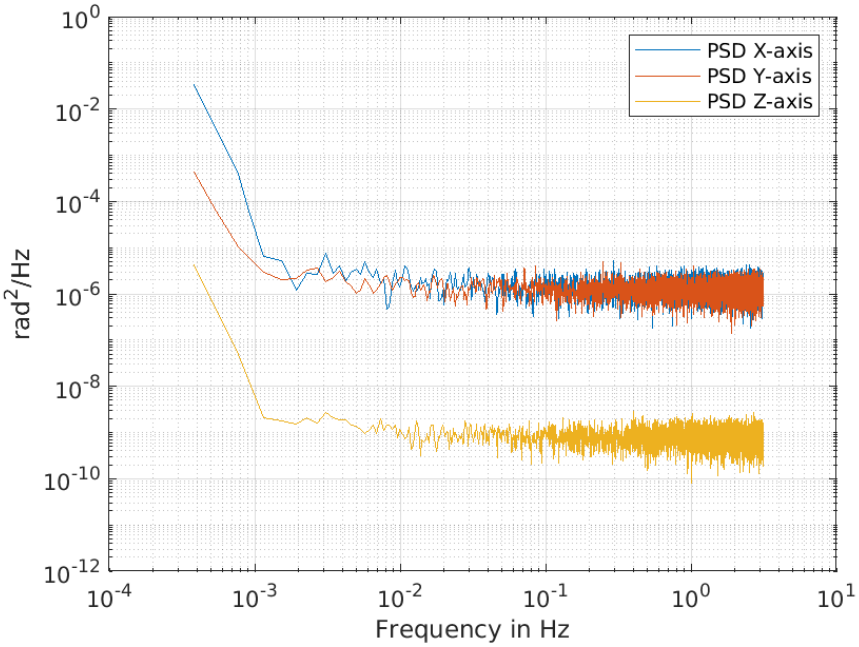

Figure 4.25: PSD of the ICM20948 gyroscope

The graph in Figure 4.25 shows that while all three axes have a rather similar curve, the z-axis lays drastically below the other two. All three axes level at a frequency higher than 10^{-2} Hz.

To fully evaluate the calculated error coefficients later in this section, Figure 4.26 shows the analysis of the PSD estimate calculated for the x-axis. This analysis can be seen as analog to the remaining two axes, as indicated by Figure 4.25.

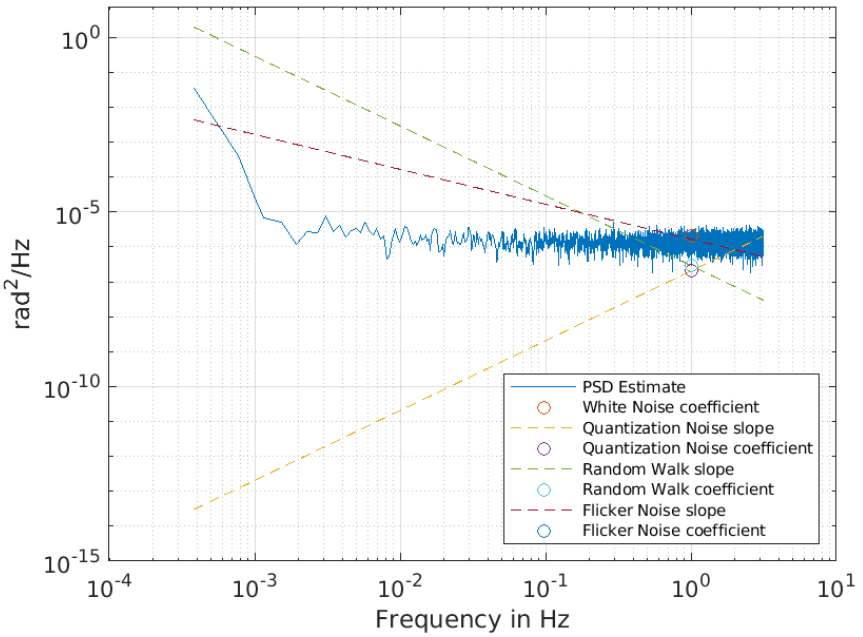

Figure 4.26: PSD of the ICM20948 x-axis gyroscope

The concrete values for the error coefficients calculated by the PSD can be found in Table 4.20.

Axis	**Quantization noise in** $(\mathrm{rad/s})/\sqrt{\mathrm{Hz}}$	**White noise in** $(\mathrm{rad/s})/\sqrt{\mathrm{Hz}}$	**Flicker noise in** $(\mathrm{rad/s})$	**Random walk in** $(\mathrm{rad/s})/\sqrt{\mathrm{Hz}}$
x-axis	0.00045188	0.0014433	0.0012902	0.00054021
y-axis	0.00061224	0.00097058	0.00088501	0.0010892
z-axis	$2.5256 \cdot 10^{-5}$	$2.6040 \cdot 10^{-5}$	$1.5532 \cdot 10^{-5}$	$1.1038 \cdot 10^{-5}$

Table 4.20: Error coefficients ICM20948 gyroscope calculated by PSD

As shown in Figures 4.25 and 4.26, only the level plot of the white noise would appear to be an acceptable fit against the PSD slope. This observation indicates that the calculated coefficients for the white noise in Table 4.20 are the only coefficients that can be considered to be accurately calculated, as the remaining slopes do not appear to be a good fit against the PSD estimate of the respective axes.

A concrete comparison between the coefficients calculated by the PSD and the allan deviation can be found in Table 4.21.

Axis	Quantization noise difference in %	White noise difference in %	Flicker noise difference in %	Random walk difference in %
x-axis	-81.591	-32.107	1094.8	29988
y-axis	-47.147	-51.561	429.00	24239
z-axis	-38.290	-50.545	369.17	17430

Table 4.21: Percentual error coefficients difference between the PSD and allan deviation calculation for the ICM20948 gyroscope

It can be seen in Table 4.21, that the deviation of the white noise coefficients for the PSD and the allan deviation appears to be consistent, which indicates an overall accurate calculation.

The deviations calculated for the quantization noise coefficients appear to be relatively small for the y- and z-axes, while the deviation for the x-axis appears to be higher. This can not be fully explained, as the values calculated by the PSD for the quantization noise had been declared to be inaccurate.

The flicker noise and random walk differences appear to be exceptionally high, which indicates that the previously calculated coefficients are inaccurate. In the case of an accurate calculation, this deviation should be considerably lower.

Separate Sensor Verification

The percentual differences in the error coefficients compared to a secondary measurement are gathered in Table 4.22.

Axis	Quantization noise difference in %	White noise difference in %	Flicker noise difference in %	Random walk difference in %
x-axis	281.85	-5.1562	-21.363	-39.808
y-axis	2523.4	-1.1176	-52.402	-69.193
z-axis	1153.1	-0.60673	-56.720	-79.113

Table 4.22: Percentual error coefficients difference ICM20948 gyroscopes

The white noise coefficient can be seen only to slightly differ for the y- and z-axis, while the difference is slightly higher for the x-axis. The overall absolute deviation, however, is under 10 %. The flicker noise is only consistent for the x-axis, with a deviation under 30 %, while the y- and z-axes show over 75 % devitations. Similarly, the random walk appears to be the most consistent on the x-axis at under 50 %, while both the y- and z-axes show over 100 % devitations.

Due to the slight error difference for the essential error coefficient, the white noise, the overall measurements of the two separate sensors can still be seen as accurate.

4.3.4 LIS3MDL

Allan Deviation

The allan deviation executed on the LIS3MDL measurements resulted in the graph as shown in Figure 4.27.

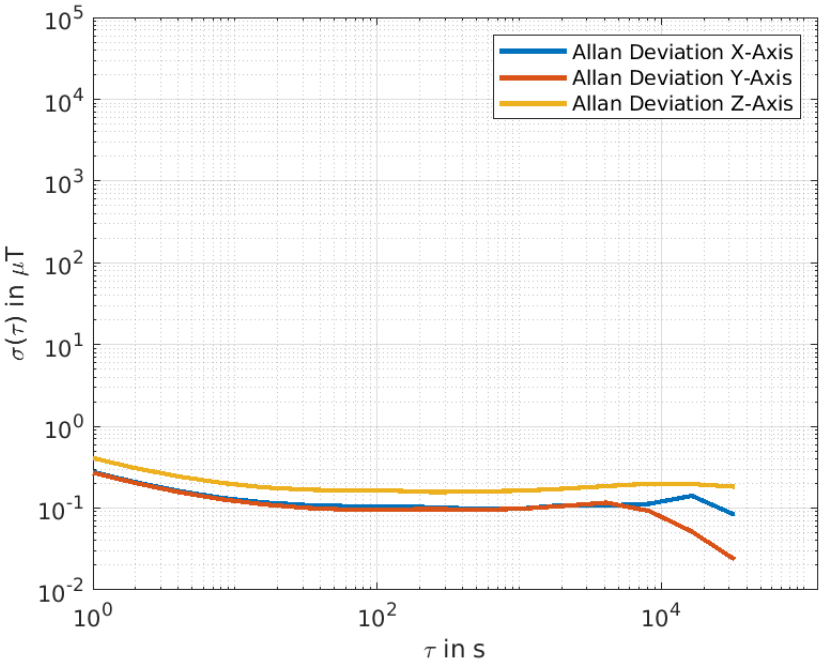

Figure 4.27: Allan deviation of the LIS3MDL magnetometer

All three axes first fall slightly before staying mainly level. The x- and the y-axes then appear to be falling stronger, indicating the quantization noise's presence. The x- and the y-axes appear similar due to their proximity in the plot, while the z-axis appears to be slightly above the other two axes.

In order to fully analyze the calculated error coefficients later in this section, Figure 4.28 shows the analyzed x-axis of the LIS3MDL magnetometer.

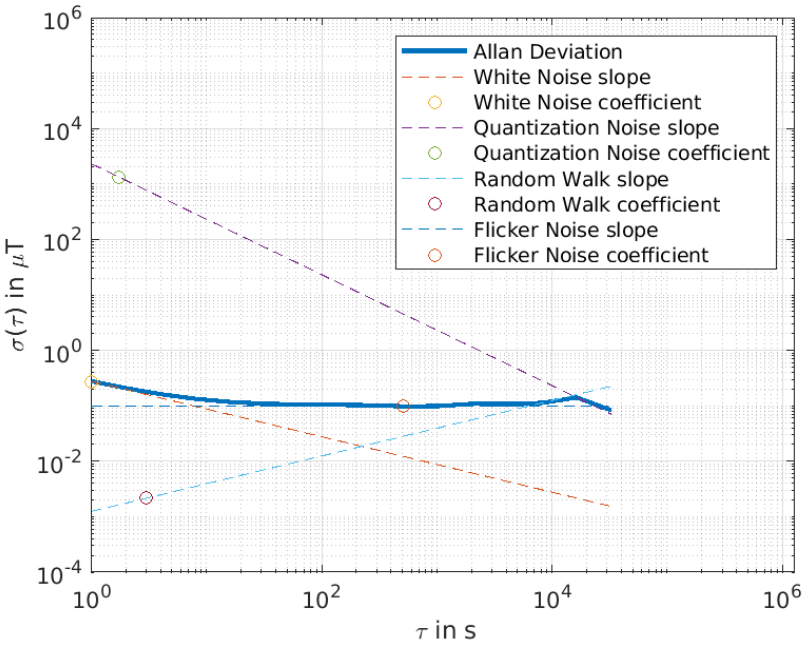

Figure 4.28: Allan deviation of the LIS3MDL magnetometer x-axis

Figure 4.28 can also be seen as an analysis of the y-axis, for which the allan deviation only slightly differs, as depicted in Figure 4.27.

As the allan deviation for the z-axis deviates from the other two axes as depicted in Figure 4.27, its analyzed allan deviation is depicted in Figure 4.29.

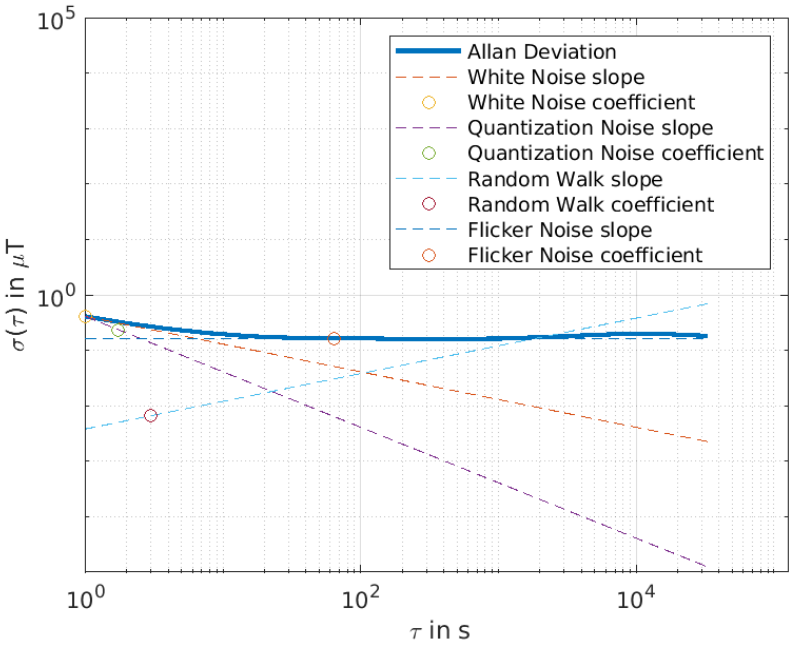

Figure 4.29: Allan deviation of the LIS3MDL magnetometer z-axis

The following error coefficients were calculated for the LIS3MDL magnetometer:

Axis	**Quantization noise in µT/$\sqrt{\text{Hz}}$**	**White noise in µT/$\sqrt{\text{Hz}}$**	**Flicker noise in µT**	**Random walk in µT/$\sqrt{\text{Hz}}$**
x-axis	1333.4	0.27599	0.14688	0.0021535
y-axis	487.16	0.27017	0.14360	0.0040602
z-axis	0.23573	0.40829	0.24637	0.0065963

Table 4.23: Error coefficients LIS3MDL magnetometer

Table 4.23 shows that the coefficients calculated for the random walk are the lowest amongst the coefficients depicted in the table. Comparing this with the respective Figures 4.27, 4.28, and 4.29, the slope of the random walk can be fitted against the allan deviation of the x-axis, which can not be said for either the y- or the z-axis. This indicates that the error coefficient calculated for the y- and z-axes can be seen to be inaccurate, while the value for the x-axis appears to be more accurate.

Next, the flicker noise coefficients are evaluated. It can be seen in Table 4.23, the values for the x- and y-axis are almost identical, while the value for the z-axis is slightly higher.

The Figures 4.27, 4.28, and 4.29 show that the slope of the flicker noise can be fitted well against the allan deviation. This indicates that the calculated coefficients can be considered to be accurate.

The calculated coefficients of the white noise are evaluated next. Similar to the flicker noise, the coefficients for the x- and y-axis appear to be almost identical. The respective figures also show that the slope of the white noise can be fitted against the respective allan deviation, which indicates a certain accuracy to the calculated error coefficients.

Lastly, the coefficients for the quantization noise are evaluated. It can be seen that the values for the x- and y-axes appear to be unrealistically high. Alongside Figure 4.28, it can be seen that this is most likely due to an inaccurate fit of the quantization noise slope. While the coefficient for the z-axis appears to be lower than the previous two axes, Figure 4.29 shows that the slope of the quantization noise can not be well fitted against the curve of the allan deviation. This fit concludes that the calculated coefficients for the quantization noise can be seen as inaccurate.

PSD Verification

A further analysis was conducted using the PSD, which resulted in the plot as shown in Figure 4.30.

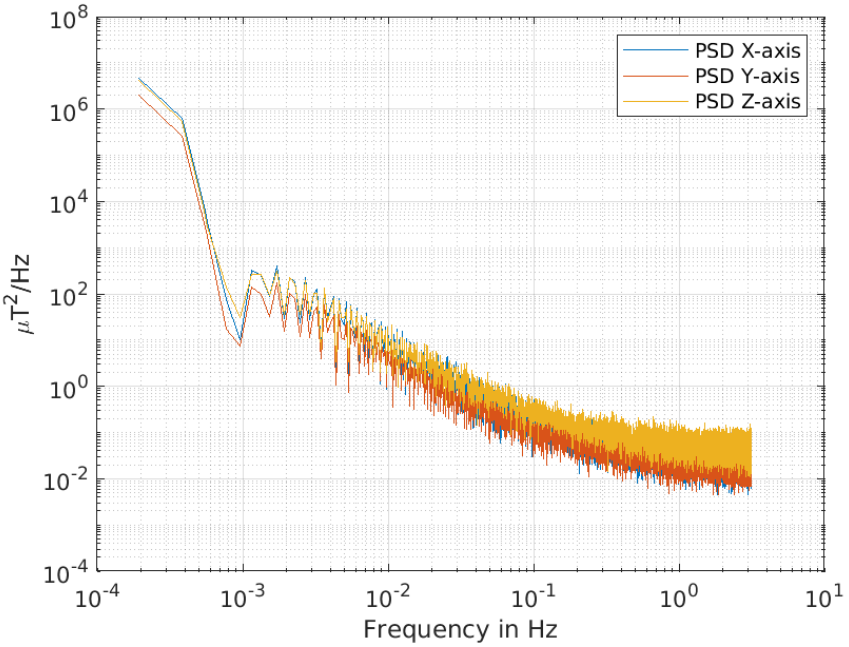

Figure 4.30: PSD of the LIS3MDL magnetometer

It can be seen in Figure 4.30 that all three axes have a very similar curve, which can be mainly described by a line with a slope of -1 and a small leveling of the plot.

To further evaluate the error coefficients, which are gathered later in this section, Figure 4.31 depicts the analyzed x-axis of the PSD estimate.

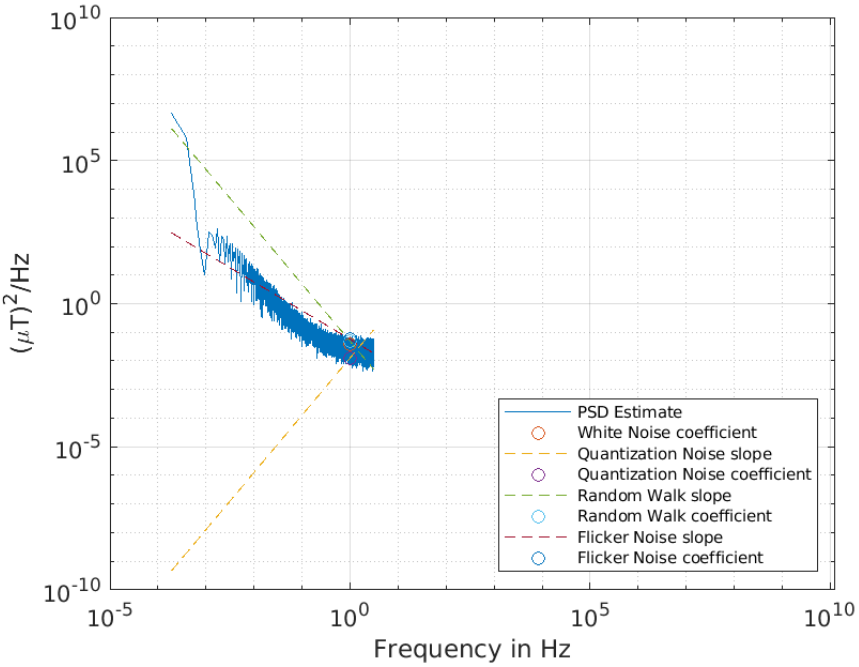

Figure 4.31: Analyzed PSD of the LIS3MDL magnetometer x-axis

As Figure 4.30 shows the PSD estimate of all three axes to be comparable, Figure 4.31 can be seen as an equivalent to the analyzed y- and z-axes.

The calculated error coefficients for each axis are gathered in Table 4.24.

Axis	**Quantization noise in µT/$\sqrt{\text{Hz}}$**	**White noise in µT/$\sqrt{\text{Hz}}$**	**Flicker noise in µT**	**Random walk in µT/$\sqrt{\text{Hz}}$**
x-axis	0.11194	0.19608	0.23903	0.22083
y-axis	0.081739	0.090525	0.18253	0.12431
z-axis	0.11257	0.23058	0.26488	0.18497

Table 4.24: Error coefficients LIS3MDL magnetometer calculated by PSD

The best fit of a slope against the PSD estimate is the slope of the flicker noise, as depicted in Figure 4.31. The level slope of the white noise might also be a good approximation. This means that out of the calculated coefficients in Table 4.24, the values for the flicker noise should be considered to be the most accurate. The white noise may follow this; however, this cannot be fully confirmed due to a lack of implementation.

Considering the calculated values, Table 4.24 shows that the coefficients of the x- and z-axis are at a comparable value, while the y-axis appears to be below the values of the other two axes.

As the slopes for neither the quantization noise, nor the random walk appear to be a good fit for the PSD estimate, the calculated values in Table 4.24 are to be neglected due to inaccuracies.

A concrete comparison between the error coefficients calculated by the allan deviation and the PSD can be found in Table 4.25.

Axis	Quantization noise difference in %	White noise difference in %	Flicker noise difference in %	Random walk difference in %
x-axis	-99.992	-28.955	62.739	10154
y-axis	-99.983	-66.493	27.109	2961.6
z-axis	-52.244	-43.525	7.5139	2704.2

Table 4.25: Percentual error coefficients difference between the PSD and allan deviation calculation for the LSM9DS1 magnetometer

Table 4.25 shows, that the deviations of the white noise error coefficients between the allan deviation and the PSD is relatively low for both the x- and z-axes, while the devitaiton for the y-axis appears to be slightly higher.

For the flicker noise differences, a relatively small deviation can be observed for the z-axis, while the x-axis appears to deviate more significantly. It has to be noted that the deviation of the flicker noise is positive, while it is negative for the white noise. An explanation for this could not be found.

The overall low deviations of the error coefficients for the white noise and the flicker noise indicate that these values could be accurately calculated.

Contrary to this observation, the deviation for the quantization noise and especially the random walk appears to be significantly higher. This observation indicates that especially the random walk error coefficients are inaccurately computed.

Separate Sensor Verification

To verify, that no damages have affected the sensor measurements of the LIS3MDL, another sensor of the same model was evaluated. The percentual deviations from the error coeficients as calculated by the allan deviation can be found in Table 4.26.

axis	Quantization noise difference in %	White noise difference in %	Flicker noise difference in %	Random walk difference in %
x-axis	-99.988	1.7760	5.2129	-9.0600
y-axis	-99.958	30.212	13.032	-3.9568
z-axis	1.2946	1.2947	-0.30469	-33.422

Table 4.26: Percentual error coefficients difference between two LIS3MDL magnetometers

As shown in Table 4.26, for the x- and z-axes, difference of the flicker noise coefficients are minimal, while it is slightly higher for the y-axis. The next important coefficient is the white noise, which has only a slight difference for the x- and z-axes while the difference is higher on the y-axis. The last important error coefficient is the quantization noise- here, great differences can be seen between the two sensors. This difference is because while the first sensor explicitly showed the influence of the quantization noise for both the x- and y-axis, this is not the case for the second sensor. These axes show a deviation of almost 200 %, while the z-axis deviation lies at under 2 %.

Overall, it can be said that the LIS3MDL appears to be relatively stable. The overall differences for the most significant error coefficients, that of the flicker and the white noise, are relatively marginal.

4.3.5 BMI088

Allan Deviation

The allan deviation executed on the BMI088 measurements resulted in the plot shown in Figure 4.32.

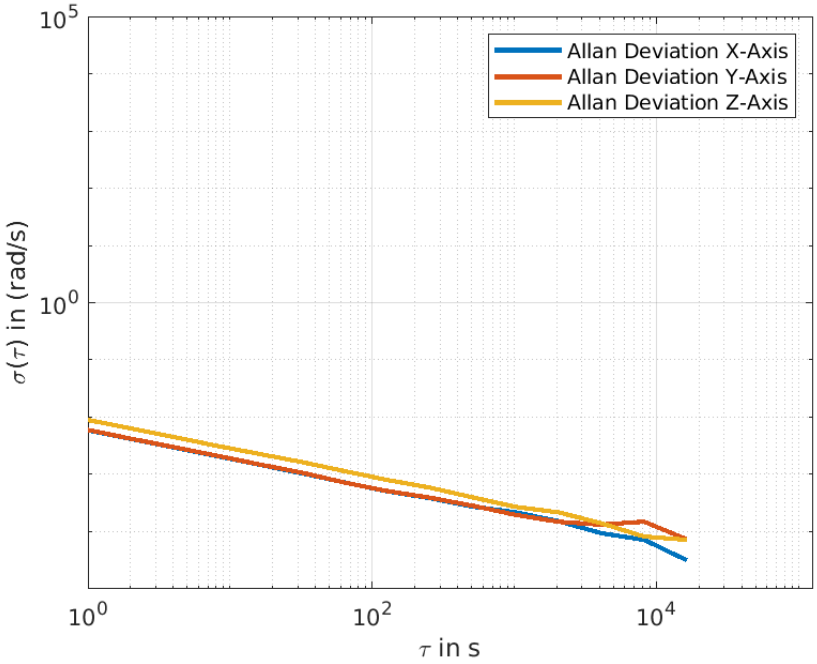

Figure 4.32: Allan deviation of the BMI088 gyroscope

Figure 4.32 shows that all three axes first fall at a slope of $-1/2$, which indicates a strong presence of white noise.

In order to fully analyze the error coefficients calulated later in this section, the analyzed allan deviation of the x-axis is depicted in Figure 4.33.

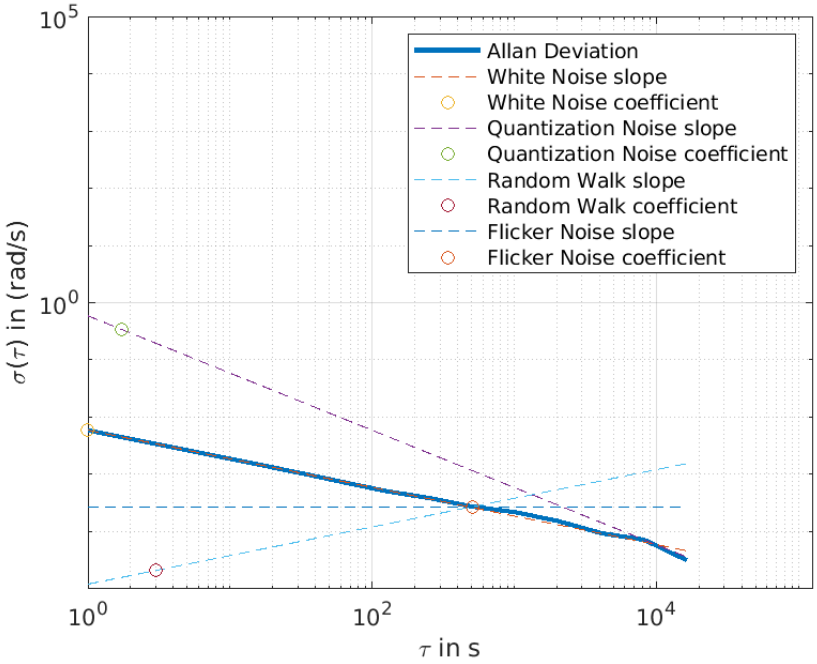

Figure 4.33: Allan deviation of the BMI088 gyroscope x-axis

As depicted in Figure 4.32, the allan deviation of the x- and the y-axes can be seen as equivalent, while the z-axis also behaves comparably. This is why the plots for these axes can be seen as equivalent. The actual plots can be found in the digital appendix.

The error coefficients were calculated for the BMI088 gyroscope and gathered in Table 4.27.

Axis	**Quantization noise in** $(\mathrm{rad/s})/\sqrt{\mathrm{Hz}}$	**White noise in** $(\mathrm{rad/s})/\sqrt{\mathrm{Hz}}$	**Flicker noise in** $(\mathrm{rad/s})$	**Random walk in** $(\mathrm{rad/s})/\sqrt{\mathrm{Hz}}$
x-axis	0.33953	0.0059126	0.00041034	$2.0865 \cdot 10^{-5}$
y-axis	0.70427	0.0059868	0.00022277	$3.5723 \cdot 10^{-6}$
z-axis	0.33026	0.0089710	0.00012293	$81.563 \cdot 10^{-6}$

Table 4.27: Error coefficients BMI088 gyroscope

Table 4.27 shows that the calculated error coefficients for the random walk are significantly lower than the other depicted coefficients. Analyzing the respective plots shown in the Figures 4.32 and 4.33 show that this low value is rather attributed to inaccuracies, as the slope of the random walk can only be fitted against fragments of

the allan deviation.

The following error coefficient to be considered is the flicker noise. Similar to the random walk, it can be seen in the Figures 4.32 and 4.33 that the slope of the flicker noise does not appear to be an appropriate fit against the plot of the allan deviation. This indicates that the values calculated for the flicker noise should be considered inaccurate.

Next, the white noise error coefficients are analyzed. The values for the x- and the y-axis are almost equivalent. Considering the Figures 4.32 and 4.33, it can be seen that the slope of the white noise can be seen as an appropriate fit against the allan deviation. This indicates that the calculated error coefficients can be considered to be accurate.

Lastly, the error coefficients of the quantization noise are analyzed. It can be seen that the values for the x- and z-axes are comparable. Considering the respective figures, it can be seen that the slop of the quantization noise can be slightly fitted against the allan deviation of the slopes, and this small fit indicates some accuracy to the calculated coefficients.

PSD Verification

Figure 4.34 shows the PSD analysing the gyroscope axes.

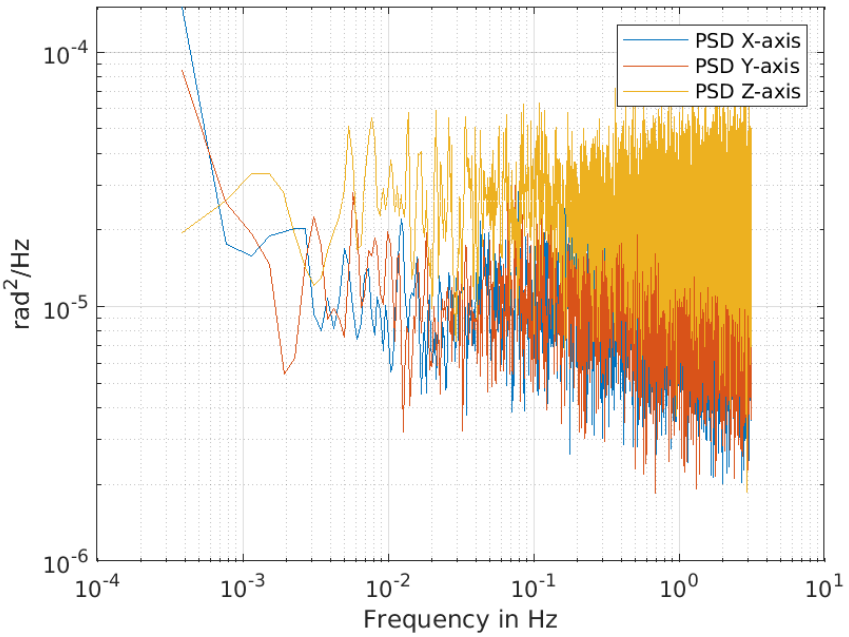

Figure 4.34: PSD of the BMI088 gyroscope

It can be seen in Figure 4.34 that all three axes behave roughly similarly, with the z-axis being the highest in the plot, followed by the y- and x-axes. All three axes appear to level out, indicating a strong white noise presence quickly.

To analyze the calculated error coefficients, Figure 4.35 depicts the analyzed PSD estimate for the x-axis.

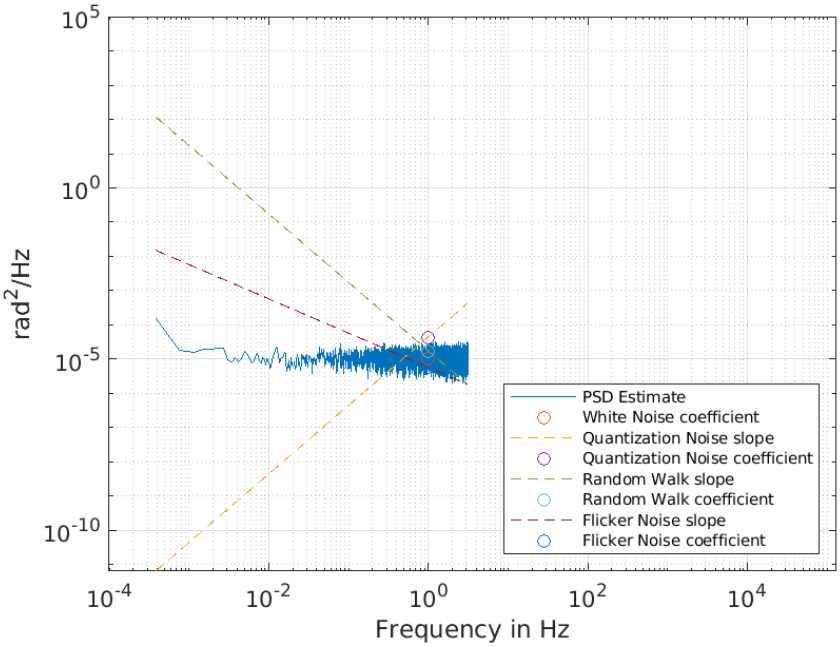

Figure 4.35: Analyzed PSD of the BMI088 gyroscope x-axis

Figure 4.35 shows the fitted lines against the graph for the x-axis. As seen in Figure 4.34, this plot can be considered to be equivalent for the y- and z-axes.

The calculated error values for all three axes can be found in Table 4.28.

Axis	**Quantization noise in** (rad/s)/$\sqrt{\text{Hz}}$	**White noise in** (rad/s)/$\sqrt{\text{Hz}}$	**Flicker noise in** (rad/s)	**Random walk in** (rad/s)/$\sqrt{\text{Hz}}$
x-axis	0.0066160	0.0032519	0.0023937	0.0041707
y-axis	0.0024058	0.0037410	0.0053328	0.0066364
z-axis	0.0055274	0.0043079	0.0054096	0.0054700

Table 4.28: Error coefficients BMI088 gyroscope calculated by PSD

Considering the Figures 4.34 and 4.35, it can be seen that the level slope of the white noise appears to be the only appropriate fit against the respective PSD estimates. This indicates that only these values gathered in Table 4.28 can be seen as accurate. The coefficients calculated for the white noise for the x- and y-axes appear to be almost equivalent.

A comparison between the error coefficients calculated by the PSD and the allan

deviation can be found in Table 4.29

Axis	Quantization noise difference in %	White noise difference in %	Flicker noise difference in %	Random walk difference in %
x-axis	-98.051	-45.000	483.35	19889
y-axis	-99.658	-37.513	2293.8	$18.567 \cdot 10^4$
z-axis	-98.326	-51.980	4300.4	$34.992 \cdot 10^4$

Table 4.29: Percentual error coefficients difference between the PSD and allan deviation calculation for the BMI088 gyroscope

It can be seen in Table 4.29, that the percentual deviations for both the flicker noise as well as the random walk are unrealistically high, which indicates an overall uncertainty regarding this error coefficient.

Contrary to these high deviations, the difference between the white noise coefficients calculated by the allan deviation and the PSD appears to be relatively low. This indicates a higher accuracy in the previous calculation for these coefficients.

Finally, the quantization noise difference should also be considered. These lay at a constant value for all three axes, which could not be fully explained.

4.4 Temperature experiments

This section gathers the results regarding the TVAC test as well as the repeated heat experiments. For the latter one, no units for the temperature are given in the respective plots due to issues in the temperature implementation, as explained in Section 4.2.

4.4.1 TVAC

Prior to a high altitude balloon launch in October 2021, a TVAC test was conducted, in which the integrated system as shown in Section 7.2.1 was set into the TVAC for multiple hours. The drift bias of the BNO055 gyroscope are gathered in Table 4.30.

File	X-axis drift in °/s/s	Y-axis drift in °/s/s	Z-axis drift in °/s/s	Temperature drift in °C/s
Log129	1.3010 $\cdot 10^{-5}$	-4.5309 $\cdot 10^{-5}$	1.0266$\cdot 10^{-5}$	-0.0035447
Log139	-0.00011163	0.00020162	-0.00026085	-0.00049213
Log141	-5.1594 $\cdot 10^{-5}$	7.3261 $\cdot 10^{-6}$	-6.4069 $\cdot 10^{-6}$	0.0021824
Log142	-1.8706 $\cdot 10^{-5}$	8.3924 $\cdot 10^{-5}$	-7.43848 $\cdot 10^{-6}$	0.0074136
Log146	-0.00077399	-0.0041280	0.00051600	0.49689

Table 4.30: Temperature and measurement drift of the BNO055 gyroscope as observed in the TVAC

The logs depicted in Table 4.30 all stem from the TVAC, however, due to the issues described in Section 3.3.2, only fragments of data could be recovered. This circumstance is the reason why the log files vary in length, and also shows why some logs are missing.

It can be observed in Table 4.30 that the highest measurement drift of the gyroscope occurs in Log146 and Log139. The highest temperature change occurs in Log146, which correlates with the highest measurement drift. This correlation, however, does not translate to the other logs: while Log142 has the second-highest temperature drift, the second-highest measurement drift occurs in Log139.

A possible explanation for this could be the external temperature sensor, which was used to record the temperature data. While located relatively close to the BNO055, this sensor cannot precisely measure the temperature of the BNO055 directly. The BNO055 magnetometer was analyzed in a similar fashion, which results in the drift values gathered in Table 4.31.

File	X-axis drift in µT/s	Y-axis drift in µT/s	Z-axis drift in µT/s	Temperature drift in °C/s
Log129	-0.00018453	0.00045537	-0.00030902	-0.0035447
Log139	-0.0028126	-0.0019536	0.00023921	-0.00049213
Log141	0.00011606	-0.00090411	9.1913 $\cdot 10^{-5}$	0.0021824
Log142	0.00014105	-2.8336 $\cdot 10^{-5}$	0.00044122	0.0074136
Log146	-0.032057	-0.020704	-0.011545	0.49689

Table 4.31: Temperature and measurement drift of the BNO055 magnetometer as observed in the TVAC

Table 4.31 shows, that the magnetometer generally experiences more drift than the

gyroscope, as depicted in Table 4.30. Logs 139 and 146 depict the strongest temperature deviations both in a positive and negative direction, showing the highest drift for the magnetometer measurements.

The lost data fragments mean that not an equal amount of data from the lowering and rising temperatures has been recorded. As a first evaluation, it can be said that the BNO055 seems to be more susceptible to a rise in temperature rather than decreasing temperature.

As the TVAC evaluation only involved one of the sensors and showed some significant gaps in data, it was evident that the evaluation had to be repeated.

4.4.2 BNO055

The results gathered from the experiment with a heat lamp as described in Section 3.3.2 are gathered here for the BNO055 measurement.

First and Second Run

Gyroscope Figures 4.36 and 4.37 depict the gyroscope recordings from the first and second temperature experiment, plotted against the recorded temperature. These two experiments were conducted using the first, original BNO055 sensor.

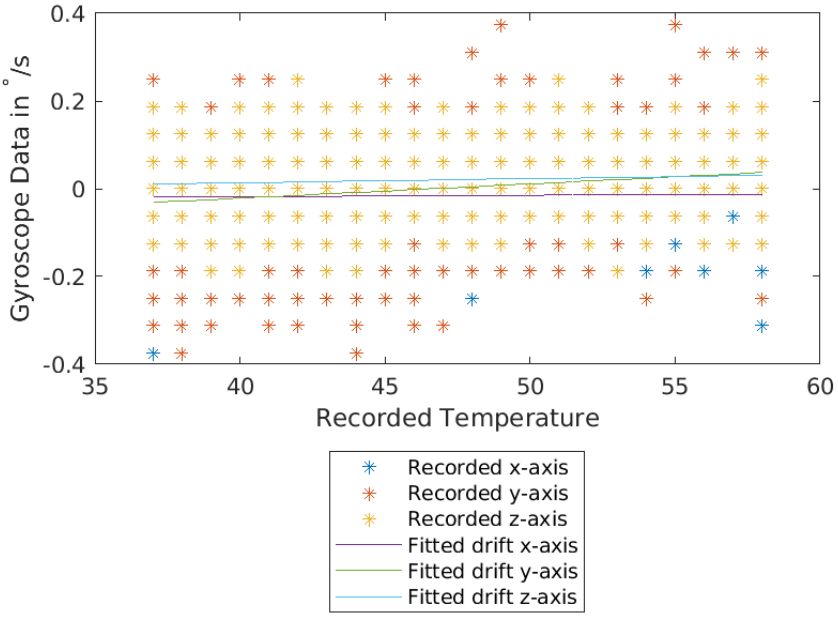

Figure 4.36: Results first run BNO055 gyroscope

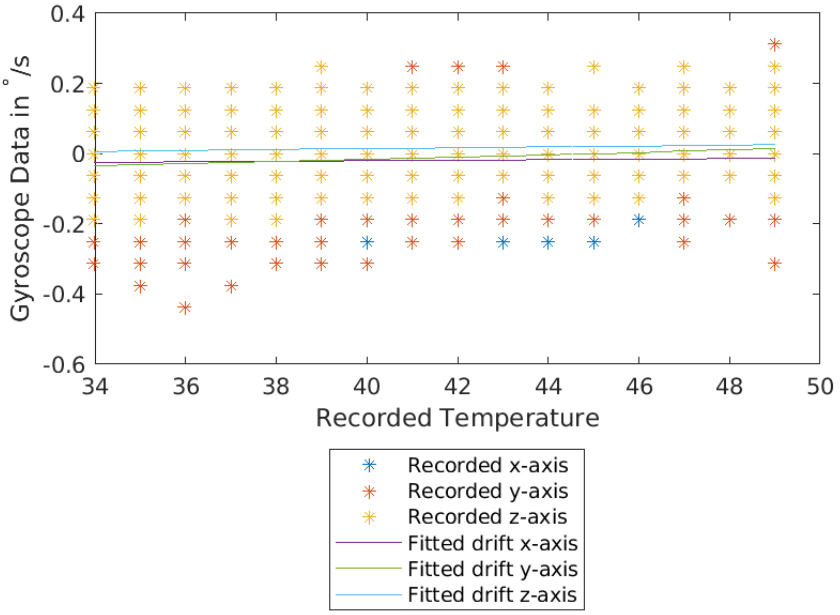

Figure 4.37: Results second run BNO055 gyroscope

The Figures 4.36 and 4.37 show, that the two plots look very similary, as the fitted lines for both gyroscopes only show a relatively small upwards slope. The measurements drift only slightly.

Table 4.32 shows the slope as well as offset from zero of both temperature runs.

Axis	**First experiment: drift in** °/s/°C	**Second experiment: drift in** °/s/°C	**First experiment: offset in** °/s	**Second experiment: offset in** °/s
x	0.00037438	0.00052039	-0.033044	-0.041445
y	0.0030917	0.0034018	-0.14199	-0.15506
z	0.00083141	0.00080102	-0.019112	-0.018734

Table 4.32: Results of the BNO055 gyroscope during both temperature experiments

All axes of the BNO055 gyroscope appear to have a small positive drift. The x-axis appears to experience the highest drift value, followed by the y- and finally z-axis.

The datasheet [21d] notes a zero offset change over temperature as a value between the typical value of $\pm$ 0.015 °/s/K and the maximum value of$\pm$ 0.03 °/s/K. This is the

comparison value to the here calculated drift value. All three axes show a lower drift than the given typical amount of drift, validating the results.

Magnetometer Figures 4.38 and 4.39 show the magnetometer recording of the original BNO055 of the two runs plotted against the recorded temperature.

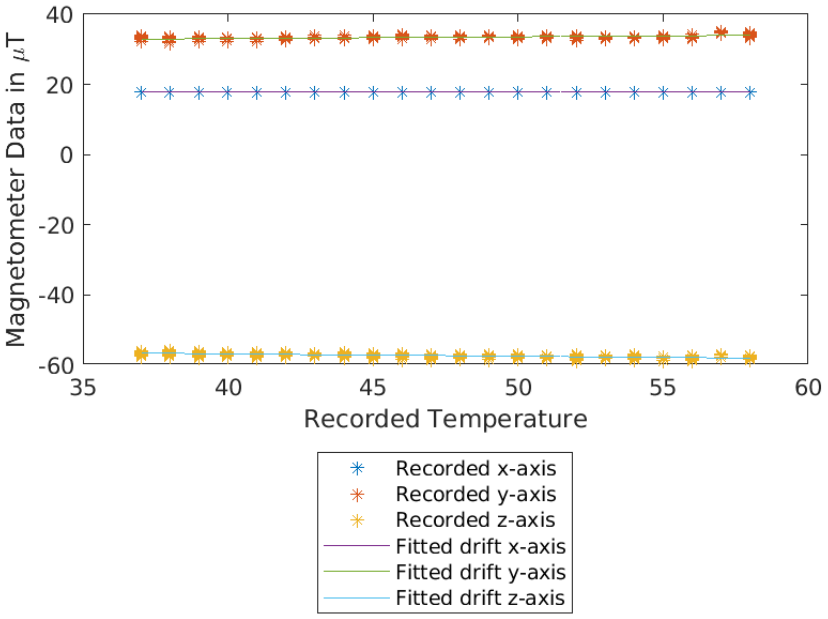

Figure 4.38: Results first run BNO055 magnetometer

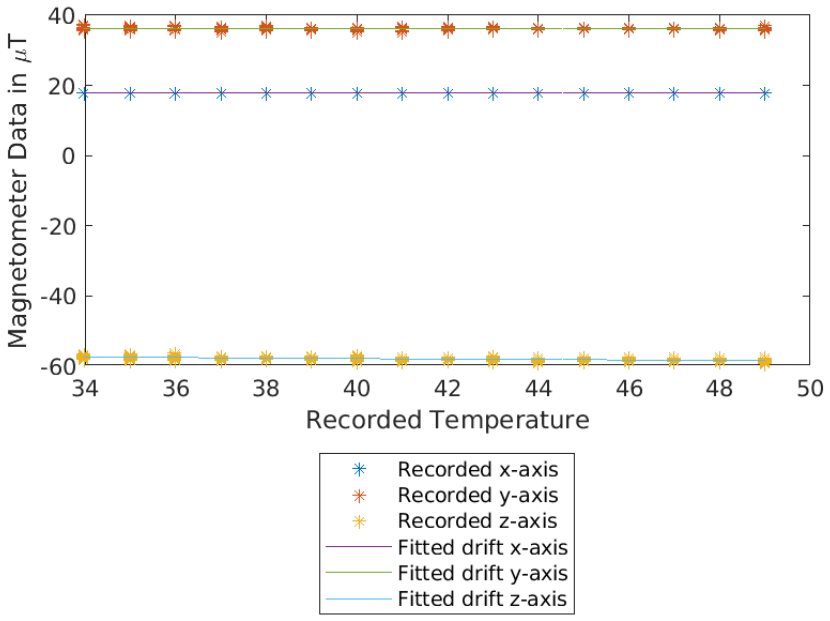

Figure 4.39: Results second run BNO055 magnetometer

Again, both graphs look quite similar, which indicates the accuracy of the experiment. Barely no drift can be seen in the respective figures.

The drifts and offsets were calculated as before for the first temperature experiment, which resulted in the values given in Table 4.33.

Axis	**First experiment: drift in µT/°C**	**Second experiment: drift in µT/°C**	**First experiment: offset in µT**	**Second experiment: offset in µT**
x	-1.8049 $\cdot 10^{-15}$	-3.9073 $\cdot 10^{-15}$	17.937	17.937
y	0.017442	-0.065231	32.827	38.778
z	-0.067986	-0.074023	-54.065	-54.882

Table 4.33: Results of the BNO055 magnetometer during both temperature experiments

Table 4.33 shows that the magnetometer barely drifts on the x-axis in both cases. The drift values on the y- and z-axes are remarkably higher than the x-axis but still at a relatively small value.

The datasheet [21d] cites a zero offset temperature drift of around $\pm$ 0.23 µT/K up to a

maximum value of $\pm$ 0.37 µT/K. This can be compared to the calculated drift values here. The drifts calculated for the x-axis are significantly lower than the given typical value. The y-axis drift of the first run appears to be slightly above the typical value, while the second run reveals a higher absolute drift. The z-axis drift of both runs lies above the maximum expected drift amount.

Summary The Sections 4.4.2 and 4.4.2 both suggest that the BNO055 has some kind of temperature compensation implemented. The datasheet [21d] does not cite anything like this, but the stability of the sensor measurements could not be guaranteed to the extent it is without any internal compensation.

Third Run

The third run with a new sensor was conducted to verify the above-analyzed data.

Gyroscope Figure 4.40 shows the recorded gyroscope data plotted against the recorded temperature.

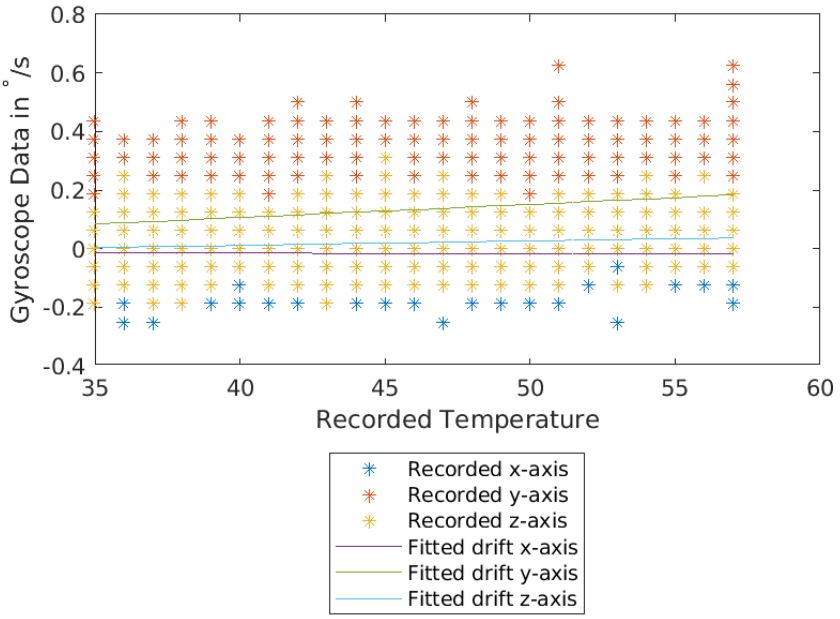

Figure 4.40: Results third run BNO055 gyroscope

Table 4.34 shows the calculated drift and offset values for the new sensor.

Axis	**Drift in °/s/°C**	**Offset in °/s**
x	-0.00018664	-0.0078763
y	0.0045472	-0.076001
z	0.0015000	-0.048900

Table 4.34: Results of the BNO055 gyroscope during the third temperature experiment

Table 4.35 gathers the percentual differences of both the respective drift and offset calculated.

Axis	**Drift deviation in %**	**Offset deviation in %**
x	-149.85	-76.164
y	47.078	-46.474
z	80.415	155.85

Table 4.35: Results deviation of the BNO055 gyroscope of the new sensor compared to the measurements of the first temperature experiment

Table 4.35 shows a rather big deviation for both the drift and the offset between the old and the new sensor. The x-axis appears to drift in another direction as previously encountered. The y-axis appears to be most stable as both for the drift and offset deviation, its absolute value stays under the 50% mark.

The accuracy of the second sensor could not be fully evaluated, however a strong reproducibility of the values could not be observed.

Magnetometer Figure 4.41 visualizes the recorded magnetometer data against the recorded temperature data of the new BNO055 sensor.

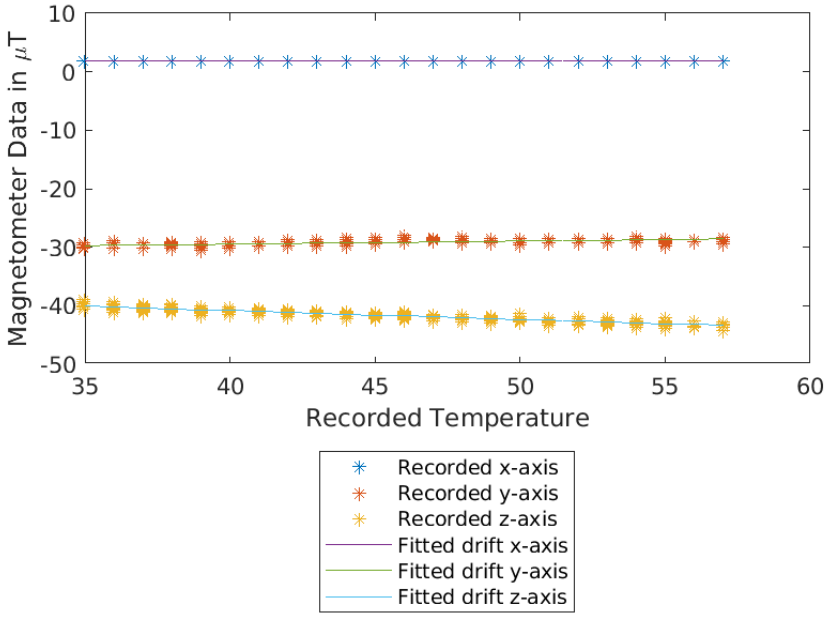

Figure 4.41: Results third run BNO055 magnetometer

The calculated offset and drift values of the new BNO055 magnetometer can be found in Table 4.36.

Axis	**Drift in µT/°C**	**Offset in µT**
x	$2.7802 \cdot 10^{-17}$	1.9370
y	0.051643	-31.527
z	-0.14738	-34.955

Table 4.36: Results of the BNO055 magnetometer during the third temperature experiment

The comparison between this third and the first run can be found in Table 4.37.

Axis	Drift deviation in %	Offset deviation in %
x	-101.54	-89.201
y	196.09	-196.04
z	116.78	-35.348

Table 4.37: Results deviation of the BNO055 magnetometer of the new sensor compared to the measurements of the first temperature experiment

Table 4.37 shows that the drift deviation is at an absolute value of over 100 %, which appears to be of significant change. The offset appears to be relatively consistent for the y-axis, while the x-axis reaches a deviation of almost -190 %.

It can not be fully determined whether this high deviation shows that the second BNO055 magnetometer supports or denies the first measurements. The strong deviations in Table 4.37 do show that some the original values could not be fully reproduced.

4.4.3 LSM9DS1

First and Second Run

Gyroscope Figures 4.42 and 4.43 depict the recorded gyroscope data of the LSM9DS1 over its recorded temperature.

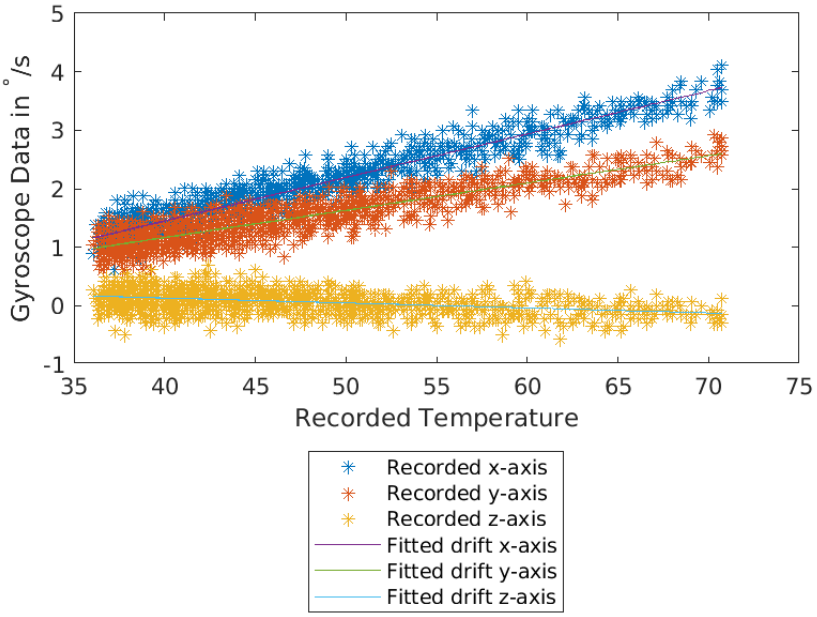

Figure 4.42: Results first run LSM9DS1 gyroscope

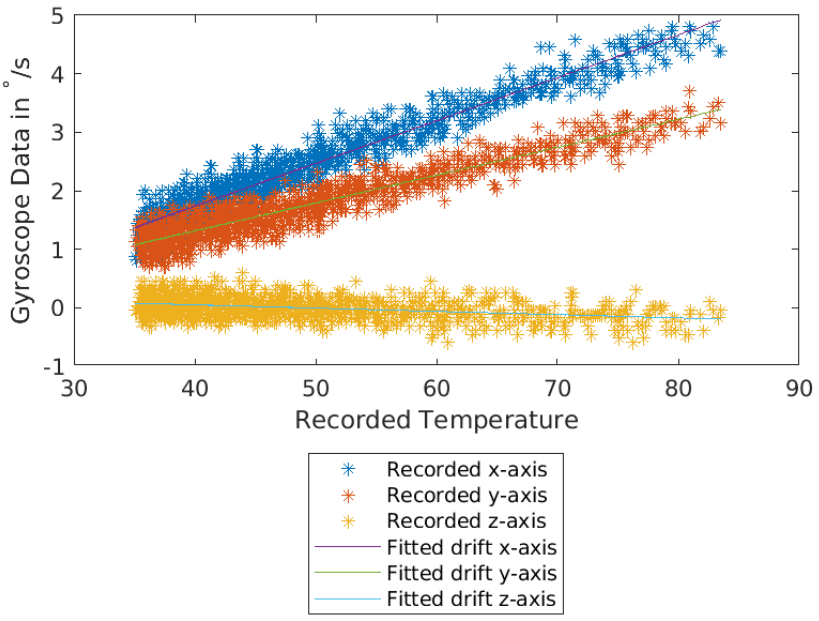

Figure 4.43: Results second run LSM9DS1 gyroscope

Both depicted graphs show similar strong drifts for the x- and y-axis, while the z-axis experiences less drift.

The results of the LSM9DS1 gyroscope recorded during the first temperature experiment are summarized in Table 4.38.

Axis	**First experiment: drift in °/s/°C**	**Second experiment: drift in °/s/°C**	**First experiment: offset in °/s**	**Second experiment: offset in °/s**
x	0.074197	0.073289	-1.5177	-1.1977
y	0.046638	0.047626	-0.69990	-0.59121
z	-0.0084739	-0.0056246	0.47116	0.27546

Table 4.38: Results of the LSM9DS1 gyroscope during both temperature experiments

It can be seen in Table 4.38 that the x-axis experiences the overall highest drift and the highest overall zero-offset. The z-axis appears to be the most stable axis amongst the three, with a slight negative drift being deductible. This also correlates with the respective Figures 4.42 and 4.43.

Magnetometer Figures 4.44 and 4.45 depict the recorded magnetometer data of the LSM9DS1 against its recorded temperature.

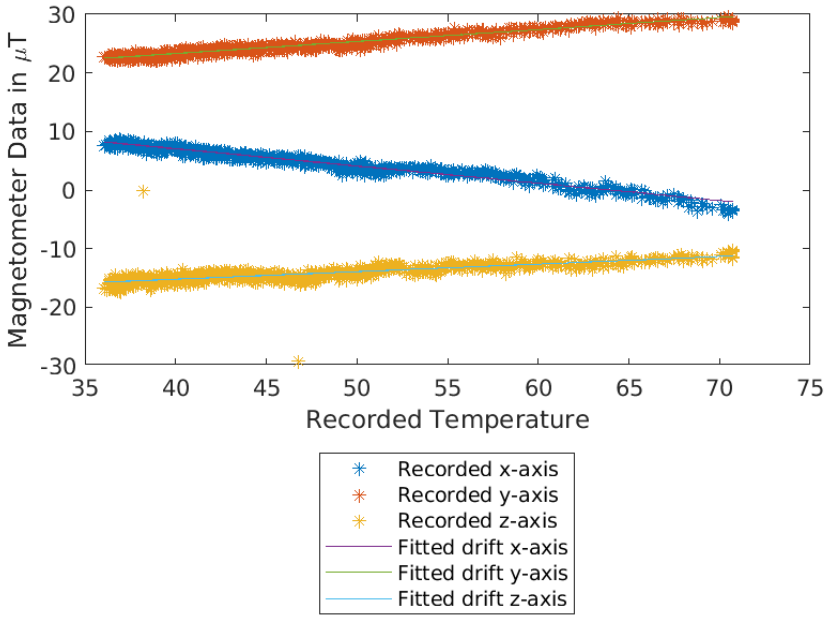

Figure 4.44: Results first run LSM9DS1 magnetometer

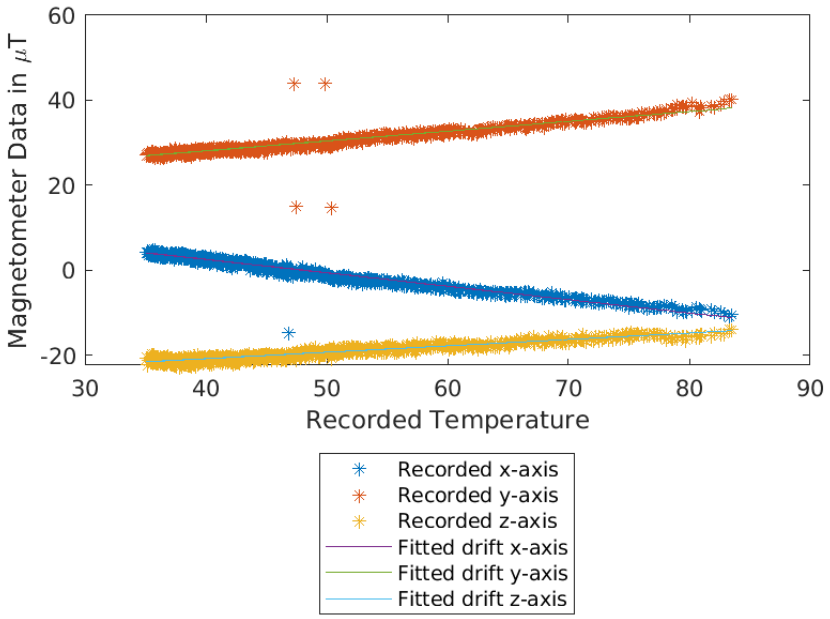

Figure 4.45: Results second run LSM9DS1 magnetometer

Both figures appear to experience some similar drift for all three axes.

Table 4.39 show the calculated drift and offset values of the first run.

Axis	**First experiment: drift in µT/°C**	**Second experiment: drift in µT/°C**	**First experiment: offset in µT**	**Second experiment: offset in µT**
x	-0.29430	-0.31586	18.824	15.202
y	0.204494	0.23075	15.124	18.886
z	0.12907	0.15075	-20.383	-26.806

Table 4.39: Results of the LSM9DS1 magnetometer during both temperature experiments

All three axes show significant drifts values. The magnetometer x- and y-axes both show similar absolute drifts value, however in opposing directions. The z-axis shows the smallest drifts amongst the three axes. Overall, the calculated values appear to be reproducible.

There is no comparison value for the temperature drift given for the LSM9DS1 gyro-

scope or magnetometer in the datasheet [15], which is why a comparison could not be conducted here.

Third Run

Next, a new LSM9DS1 is used to verify the previous results.

Gyroscope Figure 4.46 shows the recorded gyroscope data of the over its recorded temperature.

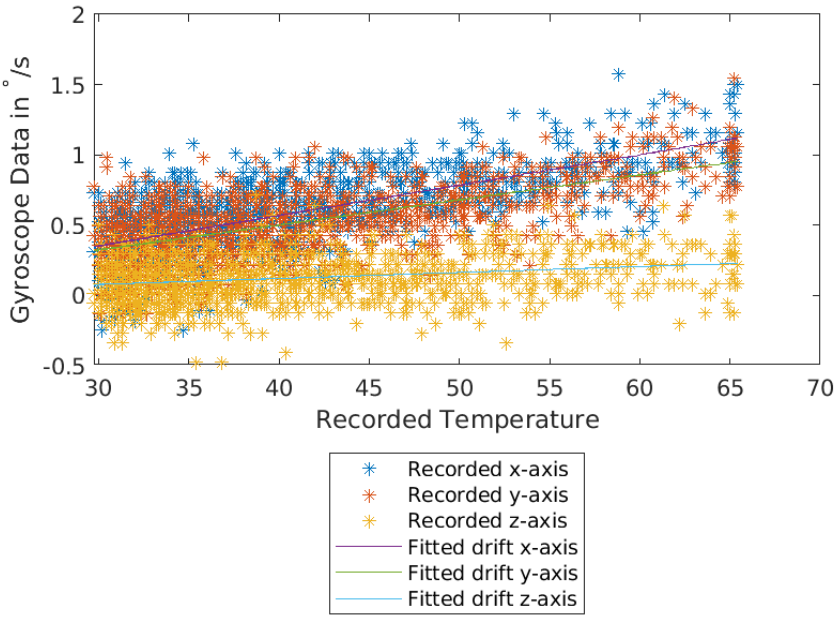

Figure 4.46: Results third run LSM9DS1 gyroscope

The x- and y-axes drift in a similar manner, while the z-axis stays relatively constant.

Table 4.40 shows the values calculated during the third temperature experiment.

Axis	Drift in °/s/°C	Offset in °/s
x	0.021638	-0.29705
y	0.017811	-0.21058
z	0.0042466	-0.048761

Table 4.40: Results of the LSM9DS1 gyroscope during the third temperature experiment

The percentual deviations between the third and the first experiment are shown in Table 4.41.

Axis	Drift deviation in %	Offset deviation in %
x	-70.837	-80.428
y	-61.809	-69.913
z	-150.11	-110.35

Table 4.41: Results deviation of the LSM9DS1 gyroscope of the new sensor compared to the measurements of the first temperature experiment

It can be seen in Table 4.41 that the z-axis appears to have the highest absolute percentual deviation, regarding the drift and the offset with the devitaion at over 100 %. The y-axis appears to be the most stable with an offset and drift deviation at just under the absolute value of 70 %. This, however, is still a relatively high deviation, which can not be fully explained. This might indicate, that one of the sensors produces faulty results, however, this claim would require a more throughout analysis.

Magnetometer The magnetometer measurments were plotted against the recorded temperature and can be seen in Figure 4.47.

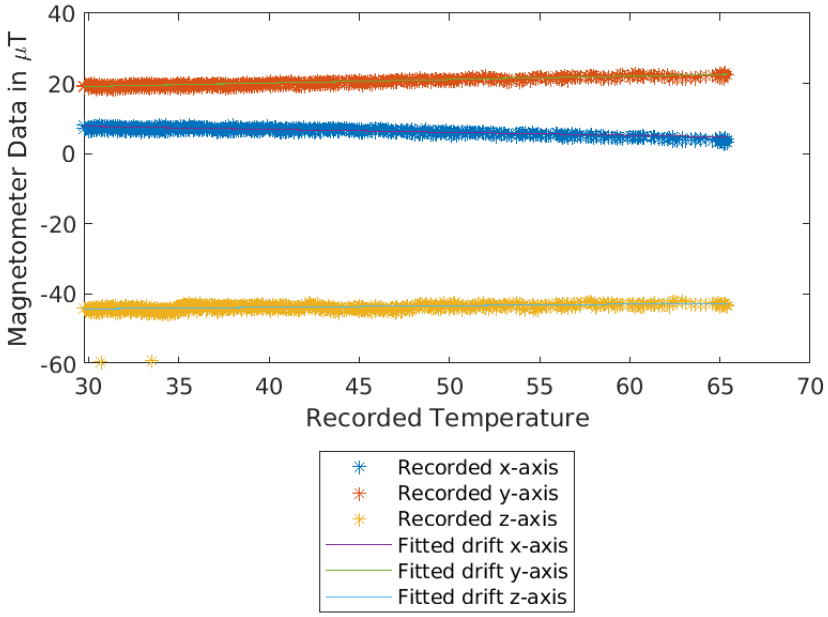

Figure 4.47: Results third run LSM9DS1 magnetometer

Figure 4.47 shows a drift for the x-and y-axes, while the z-axis appears to be relatively level.

The calculated values for the third temperature experiment can be found in Table 4.42.

Axis	**Drift in µT/°C**	**Offset in µT**
x	-0.084411	10.288
y	0.098377	16.191
z	0.045029	-45.569

Table 4.42: Results of the LSM9DS1 magnetometer during the third temperature experiment

The percentual differences compared to the first temperature experiment can be found in Table 4.43 .

Axis	Drift deviation in %	Offset deviation in %
x	-71.318	-45.348
y	-51.893	7.0540
z	-65.114	123.57

Table 4.43: Results deviation of the LSM9DS1 magnetometer of the new sensor compared to the measurements of the first temperature experiment

Similar to the gyroscope y-axis as shown in Table 4.41, the y-axis of the magnetometer of the LSM9DS1 appears to be the most stable across two different LSM9DS1 sensors, which is depicted in Table 4.43. The absolute drift devition lays at just under 50 %, while the offset deviation is under 5 %, which is considerably lower than the other two axes. A concrete reason for this can not be found as of writing this, however there appears to be a general higher consistency at the y-axis for both the gyroscope and the magnetometer of the LSM9DS1.

4.4.4 ICM20948

Plots regarding the ICM20948 can be found in the digital appendix of this work.

First and Second Run

The ICM20948 gyroscope was plotted against its recorded temperature and evaluated similar to the previous sensors. The values in Table 4.44 were calculated for the both temperature experiments.

Axis	First experiment: drift in °/s/°C	Second experiment: drift in °/s/°C	First experiment: offset in °/s	Second experiment: offset in °/s
x	-0.015330	-0.016140	0.051043	0.073886
y	-0.020091	-0.017497	0.63268	0.55256
z	0.00010184	0.00021498	-0.0066016	-0.011592

Table 4.44: Results of the ICM20948 gyroscope during both temperature experiments

While the x- and the y-axes show similar drifts for both runs in Table 4.44, the zero-offsets of the y-axis is significantly higher than that of the x-axis. The z-axis appears to be the most stable of the three axes considering its drifts and offsets.

The datasheet [17a] notes $\pm 0.05^\circ/s/^\circ C$ as a zero variation over temperature. Here, this value is represented as the drift. It can be seen that all three axes fulfill this given data from the datasheet, which indicates their accuracy.

Third Run

The third temperature experiment was conducted using a new ICM20948 sensor. The calculated values can be found in Table 4.45.

Axis	Drift in °/s/°C	Offset in °/s
x	0.0072089	-0.29722
y	-0.014214	0.88964
z	-6.1332 $\cdot 10^{-5}$	-0.0021843

Table 4.45: Results of the ICM20948 gyroscope during the third temperature experiment

Table 4.46 depicts the percentual deviation between the new sensor measurement compared to the first temperature experiment of the old sensor.

Axis	Drift deviation in %	Offset deviation in %
x	-100.91	-84.891
y	-98.477	-54.474
z	-98.905	-19.992

Table 4.46: Results deviation of the ICM20948 gyroscope of the new sensor compared to the measurements of the first temperature experiment

The depicted deviation in Table 4.46 of the drift values can be classified as high, as the percentual deviation lies at an absolute value of roughly 100%. The deviation of the offset varies, with the z-axis showing the slightest deviation of roughly -20%. The x-axis displays the highest deviation of almost -85%. Overall, the second ICM20948 deviates to a certain extent, however it can not be said whether this invalidates the results from the first two runs.

4.4.5 LIS3MDL

The plots which resulted from the LIS3MDL temperature experiments can be found in the digital appendix of this work.

First and Second Run

Table 4.47 shows the calculated drift and offset values of the first and second temperature experiment of the first LIS3MDL.

Axis	First experiment: drift in µT/°C	Second experiment: drift in µT/°C	First experiment: offset in µT	Second experiment: offset in µT
x	0.35118	0.33662	-31.460	-33.517
y	-0.49300	-0.47133	5.4680	5.0100
z	-0.39834	-0.34125	-38.312	-39.048

Table 4.47: Results of the LIS3MDL magnetometer during both temperature experiments

The x-axis experiences the only positive drift in both experiment runs, while the y- and z-axes experience a negative drift. The x- and z-axes drifts are also close concerning the absolute amount, while the y-axis encounters the absolute highest drift amongst the three axes.

The datasheet [17b] does not mention a comparison value, which is why a further comparison was not possible.

Third Run

To further analyze the values, a second, new LIS3MDL magnetometer was subjected to the same temperature experiment. The results can be found in Table 4.48.

Axis	Drift in µT/°C	Offset in µT
x	0.10379	-52.085
y	-0.12897	3.7313
z	-0.13945	-57.347

Table 4.48: Results of the LIS3MDL magnetometer during the third temperature experiment

The corresponding percentual drift values, comparing this measurement to the first run, can be found in Table 4.49.

Axis	Drift deviation in %	Offset deviation in %
x	-70.445	65.557
y	-73.840	-31.761
z	-64.993	49.685

Table 4.49: Results deviation of the LIS3MDL magnetometer of the new sensor compared to the measurements of the first temperature experiment

It can be seen in Table 4.49 that the calculated drift values of this third experiment deviate at an absolute value of roughly 70%. The offset deviates in both negative and positive percentual values, with the x-axis experiencing the highest offset deviation of around 65%, while the y-axis experiences an absolute deviation of 31%. Further analysis is necessary to evaluate this percentual deviation.

4.4.6 BMI088

The drift and offset values for the BMI088 gyroscope were calculated and can be found in the Table 4.50.

Axis	**First experiment: drift in °/s/°C**	**Second experiment: drift in °/s/°C**	**First experiment: offset in °/s**	**Second experiment: offset in °/s**
x	-3.4756 $\cdot 10^{-5}$	4.5130 $\cdot 10^{-5}$	0.030447	0.00045739
y	6.8768 $\cdot 10^{-5}$	3.8013 $\cdot 10^{-5}$	-0.052420	-0.034337
z	-6.2771 $\cdot 10^{-5}$	1.8088 $\cdot 10^{-5}$	0.021838	0.0075609

Table 4.50: Results of the BMI088 gyroscope during both temperature experiments

It can be seen in Table 4.50 that in both experiment runs, only a slight drift is calculated for all three gyroscope axes. The offset for all three axes is significantly lower in the second experiment. The datasheet [21c] offers the typical value of $\pm 0.015°/s/K$ as a comparison value for the drift values. All recorded drift of the BMI088 gyroscope is below this number. Similar to the BNO055 [21d], this data sheet does not mention any temperature compensation, however, the calculated results strongly imply the existence of such compensation.

4.5 Simulations

4.5.1 Gyroscope Simulation

Simulink

Simulating the gyroscope in Simulink as described in Section 3.4.1 resulted in plotted graphs of the simulated data which resembled the recorded data visually, as depicted in Figure 4.48 for the x-axis of the BNO055 gyroscope.

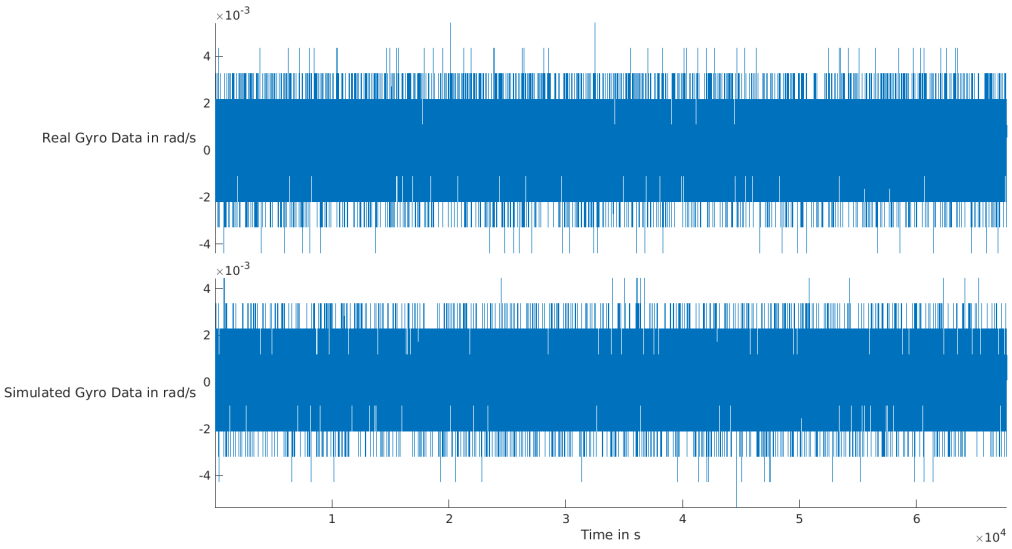

Figure 4.48: Gyroscope simulation of the x-axis of the BNO055 gyroscope

The upper graph in Figure 4.48 shows the recorded data, while the lower shows the simulation result. The gyroscope data is given in rad/s.

The resulting simulation graphs resemble their recorded counterparts similarly for the LSM9DS1, ICM20948, and BMI088, and can be found in the digital appendix of this thesis.

An issue with this approach were the different noise factors. Simulating the white noise can be done using white noise, random walk with purple noise, flicker noise with pink and quantization noise with brown noise. This can be concluded using [Matc] and the PSD slopes as depicted in Table 2.2.

When implementing these noise values, however, the simulation crashed. The cause for this could not be determined, which is why these error coefficients could not be integrated into the simulation in Figure 3.3.

ImuSensor Implementation

Simulating the sensors using the imuSensor resulted in a technically more accurate simulation. The error coefficients needed for the simulations were calculated using the allan deviation from the recorded data. The results are shown in Section 3.3.1 and were used to simulate gyroscope data. The allan deviation was then used to calculate the

error coefficients, and the resulting coefficients were compared to the initial values.

The quantization noise can not be set for the imuSensor, which is why this coefficient is neglected in the comparison.

Table 4.51 shows the absolute differences in the error coefficients calculated from the recorded and the simulated data.

Device	**Axis**	**White noise in** $(\mathrm{rad/s})/\sqrt{\mathrm{Hz}}$	**Flicker noise in** $(\mathrm{rad/s})$	**Random walk in** $(\mathrm{rad/s})/\sqrt{\mathrm{Hz}}$
BNO055	x-axis	0.00014248	0.00037291	$8.5734 \cdot 10^{-8}$
BNO055	y-axis	0.00049813	$2.4763 \cdot 10^{-5}$	$3.3372 \cdot 10^{-7}$
BNO055	z-axis	0.00027083	$2.4113 \cdot 10^{-7}$	$5.4352 \cdot 10^{-8}$
LSM9DS1	x-axis	0.00082112	0.00013398	$4.4926 \cdot 10^{-6}$
LSM9DS1	y-axis	0.00090586	0.00047625	$5.4571 \cdot 10^{-6}$
LSM9DS1	z-axis	0.00068492	$7.4444 \cdot 10^{-5}$	$4.634 \cdot 10^{-6}$
ICM20948	x-axis	0.00058159	$6.6784 \cdot 10^{-6}$	$3.2317 \cdot 10^{-7}$
ICM20948	y-axis	0.00054881	$5.1094 \cdot 10^{-7}$	$2.7749 \cdot 10^{-6}$
ICM20948	z-axis	$1.036 \cdot 10^{-5}$	$1.0847 \cdot 10^{-6}$	$3.6345 \cdot 10^{-8}$
BMI088	x-axis	0.001681	0.00017251	$8.0192 \cdot 10^{-6}$
BMI088	y-axis	0.0017419	$2.2233 \cdot 10^{-5}$	$3.1742 \cdot 10^{-6}$
BMI088	z-axis	0.0025986	$7.0715 \cdot 10^{-5}$	$1.2594 \cdot 10^{-6}$

Table 4.51: Differences in error coefficients between simulated and recorded gyroscope data

Most significant here are the white noise and the random walk. As described in Section 3.3.1, it was observed that these error coefficients have the greatest influence on the gyroscope measurement. The difference between the white noise of the recorded real and the simulated data is smaller than 0.001 $\mathrm{rad/s}$ for all sensors and axes. The BMI088 is exempt from this observation, as the error difference is still under 0.01 $(\mathrm{rad/s})/\sqrt{\mathrm{Hz}}$. This deviation was evaluated as an acceptable error margin between the real and simulated error coefficients.

The random walk stays more accurate against actual and simulated data, as the most significant deviation is still under 0.00001 $(\mathrm{rad/s})/\sqrt{\mathrm{Hz}}$.

While not heavily influential on the sensor measurements, the flicker noise can also be seen as accurately simulated, as the most significant deviation between the coefficient calculated from the real and the simulated data is under 0.001. The differentiating influence can explain the variance of the error's inaccuracy on the measurement. The

higher differences are correlated with a lesser influence on the measurements, which indicates that they can be neglected.

This analysis deems the imuSensor implementation viable for simulating a gyroscope.

4.5.2 Magnetometer Simulation

The magnetometer simulation was evaluated using the allan deviation. The error coefficients of the recorded data were calculated and then input into the imuSensor, which calculated simulated data. The error coefficients of this new dataset were then evaluated and compared against the original input values, which can be seen in Table 4.52.

The quantization noise is again neglected, as it cannot be modified using the imuSensor implementation [Matd].

Device	**Axis**	**White noise in µT/$\sqrt{\text{Hz}}$**	**Flicker noise in µT**	**Random walk in µT/$\sqrt{\text{Hz}}$**
BNO055	x-axis	0.35046	0.00022026	0.00033778
BNO055	y-axis	0.32124	0.025564	0.00020769
BNO055	z-axis	0.16833	0.0096697	0.00014132
LSM9DS1	x-axis	0.070241	0.10108	0.0014858
LSM9DS1	y-axis	0.053782	0.075748	0.00086301
LSM9DS1	z-axis	0.1264	0.048929	0.0089052
LIS3MDL	x-axis	0.060417	0.092772	0.00061628
LIS3MDL	y-axis	0.045007	0.068797	0.0021057
LIS3MDL	z-axis	0.14311	0.12161	0.002884

Table 4.52: Differences in error coefficients between simulated and recorded magnetometer data

Table 4.52 shows that the magnetometer error coefficients generally deviate between recorded and simulated data. It has to be noted that most of the magnetometer axes are highly influenced by the flicker noise, which is why that error coefficient has to be evaluated the most critically. While the BNO055 magnetometer x-axis seems to be the most accurate regarding the flicker noise, the LSM9DS1 magnetometer shows deviations of over 0.1 µT. This observation indicates a certain uncertainty in the simulation. However, it has to be noted that the strongest influence on the magnetometer measurements stems from the white noise, which can not be simulated here.

Another strong influence on the magnetometer data has the random walk. Here, no higher differences than 0.01 $(\mu T)/\sqrt{Hz}$ are observed, which deems this simulation aspect as accurate.

The imuSensor implementation does not seem to fit the magnetometer simulation as it does for the gyroscope simulation from the standpoint of the allan deviation. However, it appears to be in an acceptable margin and, due to a lack of alternatives, can be seen as a proper simulation implementation of a magnetometer.

4.6 Calibration

The setup for the following experiments and results can be found in Section 3.5.

4.6.1 Fixed Scale Matrix

The following subsections use the parameter sets as described in Subsection 3.5.1.

Set 1

Table 4.53 shows the calculated biases with the inputted parameters as described in Section 3.5.

Calibration algorithm	**calculated x-bias in µT**	**calculated y-bias in µT**	**calculated z-bias in µT**
Given bias	-34.132	-244.33	15.000
magcal	-34.1322	-244.33	15.000
TWOSTEP [Cra]	-33.937	-244.21	15.089

Table 4.53: Biases calculated from Set 1

It can be seen in Table 4.53 that the magcal implementation shows the most accurate approximation for the bias calculation, while the TWOSTEP has a slightly higher deviation between actual and calculated bias values.

Next, the calculated scale-matrices are evaluated and can be found in Table 4.53.

Calibration algorithm	calculated scale matrix
Given scale matrix	$\begin{bmatrix} 0.9 & 0.5 & 2 \\ 0.5 & 2 & 0.1 \\ 2 & 0.1 & 3 \end{bmatrix}$
magcal	$\begin{bmatrix} 2.9745 & -0.46817 & -1.5507 \\ -0.46817 & 0.80345 & 0.20774 \\ -1.5507 & 0.20774 & 1.2709 \end{bmatrix}$
TWOSTEP [Cra]	$\begin{bmatrix} 0.89741 & 0.49973 & 1.9986 \\ 0.49973 & 1.9961 & -28.308 \\ 1.99865 & 0.095069 & 2.9908 \end{bmatrix}$

Table 4.54: Scale matrices calculated from Set 1

It can be seen in Table 4.54, that the values calculated by the TWOSTEP algorithm resemble the given values, while a stronger difference can be obeserved for the magcal. A reason for this might be the diferent underlying models, as described in Subsection 3.5.3, which appears to not influence the bias calculation, as seen in Table 4.53.

Set 2

Set 2 calculated the biases as gathered in Table 4.55.

Calibration algorithm	calculated x-bias in µT	calculated y-bias in µT	calculated z-bias in µT
Given bias	2	10	4
magcal	2.0000	10.0000	4.0000
TWOSTEP [Cra]	2.2340	9.8119	3.6602

Table 4.55: Biases calculated from Set 2

Similar to Table 4.53, the calculated biases from magcal is the closest to the input value. The TWOSTEP seems to correctly calculate the bias for the y-axis, the x-axis is however wrongly calculated. Crassidis implementation shows homogenous values for all three axes. The calculated scale matrices are shown in Table 4.56.

Calibration algorithm	calculated scale matrix
Given scale matrix	$\begin{bmatrix} 0.9 & 0.5 & 2 \\ 0.5 & 2 & 0.1 \\ 2 & 0.1 & 3 \end{bmatrix}$
magcal	$\begin{bmatrix} 2.9745 & -0.46817 & -1.5507 \\ -0.46817 & 0.80345 & 0.20774 \\ -1.5507 & 0.20774 & 1.2709 \end{bmatrix}$
TWOSTEP [Cra]	$\begin{bmatrix} 0.89720 & 0.49992 & 1.9996 \\ 0.49992 & 1.9967 & 0.094854 \\ 1.9996 & 0.094854 & 2.9904 \end{bmatrix}$

Table 4.56: Scale matrices calculated from Set 2

It can be seen in Table 4.56, the calculated scale matrix only slightly varies from the calculated values in Table 4.54 for both implementations. This is the expected result, as the input scale matrix did not change. The values calculated by the TWOSTEP algorithm in Table 4.56 resemble the given values, while a more substantial difference can be observed for the magcal. A reason for this might be the different underlying models, as described in Subsection 3.5.3.

Set 3

Table 4.57 shows the calculated biases using the third set of input biases.

Calibration algorithm	calculated x-bias in µT	calculated y-bias in µT	calculated z-bias in µT
Given bias	20	0	9
magcal	20.000	-0.00000	9.0000
TWOSTEP [Cra]	20.191	-0.13014	8.7253

Table 4.57: Biases calculated from Set 3

Similar to the first two bias sets, the calculated bias from the magcal implementation is the closest to the input bias, with the TWOSTEP calculating roughly worse values for the bias.

The scale matrices were calculated and gathered in Table 4.58.

Calibration algorithm	calculated scale matrix
Given scale matrix	$\begin{bmatrix} 0.9 & 0.5 & 2 \\ 0.5 & 2 & 0.1 \\ 2 & 0.1 & 3 \end{bmatrix}$
magcal	$\begin{bmatrix} 2.9745 & -0.46817 & -1.5507 \\ -0.46817 & 0.80345 & 0.20774 \\ -1.5507 & 0.20774 & 1.2709 \end{bmatrix}$
TWOSTEP [Cra]	$\begin{bmatrix} 0.89749 & 0.49963 & 1.9994 \\ 0.49963 & 1.9971 & 0.094149 \\ 1.9994 & 0.094149 & 2.9886 \end{bmatrix}$

Table 4.58: Scale matrices calculated from Set 3

Table 4.58 shows that the calculated values are comparable to the previous calculated matrices in Tables 4.54 and 4.56. The reason, why the scale matrix calculated by magacal deviates further from the given values than the TWOSTEP result, stays the same as described in Subsection 4.6.1.

Set 4

Finally, the fourth set of biases was input into the calibration methods. The biases were calculated and gathered in Table 4.59.

Calibration algorithm	calculated x-bias in µT	calculated y-bias in µT	calculated z-bias in µT
Given bias	42.33	-74.3	21.98
magcal	42.330	-74.300	21.980
TWOSTEP [Cra]	42.373	-74.277	21.986

Table 4.59: Biases calculated from Set 4

The biases from the magcal calibration appear to be the closest to the actual values again, with the result from the TWOSTEP algorithm being slightly different.

The calculated scale matrices are gathered in Table 4.60.

Calibration algorithm	calculated scale matrix
Given scale matrix	$\begin{bmatrix} 0.9 & 0.5 & 2 \\ 0.5 & 2 & 0.1 \\ 2 & 0.1 & 3 \end{bmatrix}$
magcal	$\begin{bmatrix} 2.9745 & -0.46817 & -1.5507 \\ -0.46817 & 0.80345 & 0.20774 \\ -1.5507 & 0.20774 & 1.2709 \end{bmatrix}$
TWOSTEP [Cra]	$\begin{bmatrix} 0.89843 & 0.49956 & 1.9987 \\ 0.49956 & 1.9979 & 0.097164 \\ 1.9997 & 0.097164 & 2.9936 \end{bmatrix}$

Table 4.60: Scale matrices calculated from Set 4

The calculated scale matrices in Table 4.60 appear to be similar to the previously calculated scale matrices in the Tables 4.54, 4.56 and 4.58. Again, the scale matrix calculated by magcal deviates from the given values, which is not the case for the scale matrix calculated by TWOSTEP. The reason for this appears to be the differing magnetometer models underlying the calculations.

4.6.2 Fixed Bias

The following subsections use the parameter sets as described in Subsection 3.5.2.

Set 1

The first set calculated the biases as shown in Table 4.61.

Calibration algorithm	calculated x-bias in µT	calculated y-bias in µT	calculated z-bias in µT
Given bias	2	10	4
magcal	2.0000	10.000	4.0000
TWOSTEP [Cra]	1.8719	10.104	4.3039

Table 4.61: Biases calculated from scale matrix Set 1

The calculation of the biases using the magcal implementation is the most accurate one to the actual values in Table 4.61, followed by the TWOSTEP algorithm.

Next the calculated scale matrices are gathered in Table 4.62.

Calibration algorithm	calculated scale matrix
Given scale matrix	$\begin{bmatrix} 0.9 & 0.5 & 2 \\ 0.5 & 2 & 0.1 \\ 2 & 0.1 & 3 \end{bmatrix}$
magcal	$\begin{bmatrix} 2.9745 & -0.46817 & -1.55070 \\ -0.46817 & 0.80345 & 0.20774 \\ -1.5507 & 0.20774 & 1.2709 \end{bmatrix}$
TWOSTEP [Cra]	$\begin{bmatrix} 0.90133 & 0.50027 & 2.0012 \\ 0.50027 & 2.0002 & 0.10377 \\ 2.0012 & 0.10377 & 3.0099 \end{bmatrix}$

Table 4.62: Scale matrices calculated from Set 1

The calculated scale matrix in Table 4.62 for the magcal implementation is roughly the same as in Table 4.56. It can again be observed, that the TWOSTEP algorithm results in a better estimation of the scale matrix.

Set 2

The second scale matrix was applied to the calculations and the following biases were calculated and collected in Table 4.63.

Calibration algorithm	calculated x-bias in µT	calculated y-bias in µT	calculated z-bias in µT
Given bias	2	10	4
magcal	2.0000	10.000	4.0000
TWOSTEP [Cra]	2.0585	9.9543	3.8732

Table 4.63: Biases calculated from scale matrix Set 2

Similar to Table 4.61, Table 4.63 the magcal implementation accurately calculates the bias values, followed by the bias calculated by the TWOSTEP algorithm.

The calculated scale matrices are shown in Table 4.64.

Calibration algorithm	calculated scale matrix
Given scale matrix	$\begin{bmatrix} 10 & 0.5 & -2 \\ 0.5 & 2 & 1 \\ -2 & 1 & 3 \end{bmatrix}$
magcal	$\begin{bmatrix} 0.58729 & -0.066604 & 0.39375 \\ -0.066604 & 1.0187 & -0.078358 \\ 0.39375 & -0.078358 & 1.9492 \end{bmatrix}$
TWOSTEP [Cra]	$\begin{bmatrix} 9.9939 & 0.50316 & -1.9930 \\ 0.50316 & 4.9989 & 0.096141 \\ -1.9930 & 0.096141 & 2.9912 \end{bmatrix}$

Table 4.64: Scale matrices calculated from Set 2

The resulting scale matrices in Table 4.64 show that the TWOSTEP calculates a scale matrix close to the given input. The matrix calculated by magcal differs from the previously calculated matrices; however, the values and the signs do not correctly estimate the given scale matrix. Similar to Subsection 4.6.1, this might be caused by the underlying mathematical model of the magcal method.

Set 3

The third input scale matrix results in the following bias values for each calibration method and collected in Table 4.65.

Calibration algorithm	calculated x-bias in µT	calculated y-bias in µT	calculated z-bias in µT
Given bias	2	10	4
magcal	2.0000	10.000	4.0000
TWOSTEP [Cra]	-9.4472	-1.6745	4.7530

Table 4.65: Biases calculated from scale matrix Set 3

It can be observed in Table 4.65, that the magcal implementation correctly estimates the bias. The TWOSTEP, however, clearly deviates from the given bias, which is surprising.

The calculated scale matrices can be found in Table 4.66.

Calibration algorithm	calculated scale matrix
Given scale matrix	$\begin{bmatrix} 0.9 & -30 & 2 \\ -30 & 2 & 1 \\ 2 & 1 & 3 \end{bmatrix}$
magcal	$\begin{bmatrix} 0.47501 & 0.029665 & 0.12318 \\ 0.029665 & 0.48706 & 0.25876 \\ 0.12318 & 0.25876 & 4.5006 \end{bmatrix}$
TWOSTEP [Cra]	$\begin{bmatrix} 28.981 & -2.3788 & -0.62996 \\ -2.3788 & 28.921 & -1.6178 \\ -0.62996 & -1.6178 & 3.2277 \end{bmatrix}$

Table 4.66: Scale matrices calculated from Set 3

Different from previous sets, the TWOSTEP algorithm appears to calculate a scale matrix that highly deviates from the input scale matrix. A similar deviation could already be seen in the bias calculation in Table 4.65. A possible reason for this might be the underlying mathematical model of the TWOSTEP; however, this deviation was only observed in this specific combination of input parameters. Alternatively, the scale matrix used as an input parameter might be the cause of the issue. The magcal algorithm appears to calculate an acceptable bias, however, as seen in Table 4.65, which counteracts this thesis.

The scale matrix calculated by the magcal algorithm in Table 4.66 cannot be seen as an indicator of whether the input matrix may cause the unusual deviations exhibited by the TWOSTEP. The magcal matrix does vary from previously calculated scale matrices, which, however, could not be thoroughly evaluated previously.

Set 4

The fourth input scale matrix is a non-symmetric matrix which differs to the previously used scale matrices. The calculated biases can be found in Table 4.67.

Calibration algorithm	calculated x-bias in µT	calculated y-bias in µT	calculated z-bias in µT
Given bias	2	10	4
magcal	2.0000	10.000	4.0000
TWOSTEP [Cra]	2.9455	9.7774	3.8377

Table 4.67: Biases calculated from scale matrix Set 4

The magcal biases in Table 4.67 are an accurate estimation of the actual value. The TWOSTEP appears to be estimating the biases with a slightly higher devitation to the magcal algorithm.

The calculated scale matrix are gathered in Table 4.68

Calibration algorithm	**calculated scale matrix**
Given scale matrix	$\begin{bmatrix} 0.9 & 0.6 & 0.01 \\ 0.47 & 2 & 0.21 \\ 2 & -0.1 & 3 \end{bmatrix}$
magcal	$\begin{bmatrix} 1.9206 & -0.38955 & -1.0295 \\ -0.38955 & 0.89988 & 0.23484 \\ -1.0295 & 0.23484 & 1.1869 \end{bmatrix}$
TWOSTEP [Cra]	$\begin{bmatrix} 1.4329 & 0.44270 & 1.3103 \\ 0.44270 & 2.0280 & -0.051907 \\ 1.31033 & -0.051907 & 2.7809 \end{bmatrix}$

Table 4.68: Scale matrices calculated from Set 4

It can be seen in Table 4.68 neither the magcal nor the TWOSTEP algorithm can adequately calculate the given scale matrix.

5 Discussion

5.1 Sensor Selection

5.1.1 Encountered Issues

A series of sectors complicated the selection of the sensors:

- **Availability** A multitude of possible sensors had to be rejected due to not being available as a result of the semiconductor crisis. Instead of the BMI088, the BMG250 was initially considered. Unlike the BMI088, this sensor consists of only a gyroscope while retaining similar characteristics [21b]. This decision was made as the BMG250 was not available online.
- **Documentation** As mentioned, the documentation of the sensor is crucial for the team and the implementation of the sensors in DOSIS. Such documentation was not found for the MTi-7 developed by Xsens [21e], which had been previously selected as a possible sensor alongside the BNO055.
- **Cost** The available budget was another argument against a sensor like the MTi-7. That sensor is in a price range of around 400€. Similarly, the same can be said about space-graded sensors, which limited the selection and complicated the selection process.
- **Time** Selecting the sensors in a limited period was another critically influencing aspect of the selection process. Due to the semiconductor crisis, sensor availability could vary from available to sold out for multiple months within a short period. This meant that the selection had to be done under certain time pressure, as otherwise possible candidates could not be available after a small amount of time.
- **Inconsistent datasheets** The selection process of the sensors was also halted by the datasheets of different sensors. As can be seen in the Tables 4.1 and 4.2 units and given characteristics across given datasheets can vary. Additionally, the naming of the characteristics is not consistent between different manufacturers. These inconsistencies complicated the selection process immensely, as sensors could not always be easily compared to each other.

5.2 Error coefficients

5.2.1 Allan Variance

Gyroscopes

As a general rule, the white noise can be seen as the overall most influential error source amongst the gyroscopes. This was concluded by analyzing the respective log-log plots in Section 4.3, which is why this error source is the most analyzed in this section.

The gyroscope axes were sorted by their respective calculated white noise error coefficients and gathered in Table 5.1.

Device	**Axis**	**White noise in** $(\mathrm{rad/s})/\sqrt{\mathrm{Hz}}$
ICM20948	z-axis	$5.2654 \cdot 10^{-5}$
BNO055	z-axis	0.0011311
BNO055	y-axis	0.0015144
BNO055	x-axis	0.0018760
ICM20948	y-axis	0.00200370
ICM20948	x-axis	0.0021258
LSM9DS1	z-axis	0.0027094
LSM9DS1	y-axis	0.0032936
LSM9DS1	x-axis	0.0033869
BMI088	x-axis	0.0059126
BMI088	y-axis	0.0059868
BMI088	z-axis	0.0089710

Table 5.1: Gyroscope axes sorted by their white noise error coefficients in ascending order

Table 5.1 shows the ICM20948 z-axis to be the least affected by the white noise, followed by all axes of the BNO055 gyroscope. It has to be noted that all gyroscope axes are gathered together in Table 5.1, with the ICM20948 being the only exception. This grouping of axes could stem from the fact that the axes of one gyroscope behave similarly to each other due to similar production procedures. Why the z-axis of the ICM20948 appears to be deviating from this can not be determined. The difference between the BMI088 and the BNO055 regarding their error coefficients must also be noted. Both originate from the same manufacturer and show similar characteristics [21d], [21c] which should indicate that. As a general device, the BNO055 gyroscope

shows the lowest white noise error coefficient over all three of its axes.

Contrary to the initial finding of the white noise being the most dominant error source in the gyroscope measurements, a similar analysis in [EHN08] concluded that the flicker noise or the quantization noise is the most prominent among the analyzed sensors. The sensors analyzed in [EHN08] are sorted by grading, which indicates certain robustness or accuracy for intended uses, such as navigation or tactical maneuvers.

While the four used gyroscopes are the most influenced by the white noise, this is not a universal finding for other gyroscopes, especially those with a given rating. It could be possible that the white noise is mainly found in cheaper sensors without a designated grading.

Magnetometers

The log-log plots in Section 4.3 revealed that the error coefficients with the highest accuracy appear to be the random walk or white noise and the flicker noise, which is why these error coefficients are the most analyzed in this section.

The devices and axes were sorted after the error coefficients calculated with the Allan Variance and based on the respective first recording. This is shown in Table 5.2.

Device	**Axis**	**White noise in µT/$\sqrt{\text{Hz}}$**	**Flicker noise in µT**
LIS3MDL	y-axis	0.27017	0.14360
LIS3MDL	x-axis	0.27599	0.14688
LSM9DS1	x-axis	0.27762	0.15262
LSM9DS1	y-axis	0.33568	0.16376
LSM9DS1	z-axis	0.39480	0.24484
LIS3MDL	z-axis	0.40829	0.24637
BNO055	z-axis	0.59239	0.015409
BNO055	y-axis	1.1557	0.098254
BNO055	x-axis	1.2057	0.048810

Table 5.2: Magnetometer axes sorted by their white noise and flicker noise coefficients in ascending order with the lowest error at the top

It can be observed in Table 5.2 that the separate axes of a device appear to behave similarly, with only the LIS3MDL z-axis deviating from this. The LIS3MDL overall appears to be the magnetometer with the lowest relevant error coefficients, and the

LSM9DS1 magnetometer follows this sensor. Both of these magnetometers stem from the same manufacturer ([15], [17b]), which might explain their similar behavior.

A direct comparison with other magnetometers characterized in other academic papers was not possible due to a lack of possible sources.

5.2.2 New sensor verification

The error coefficients were also calculated for a new set of sensors with the same conditions as previously described in Section 3.3.1, with the results gathered in Section 4.3. It could be seen that the most relevant error coefficients varied between two different sensors. The reason for this might be that the original sensor had been used before their long-term recording and later analysis. This prolonged usage might have damaged the sensors in some way. Additionally, changes in the environment might be the reason for the significantly higher deviation of the magnetometer error coefficients.

Table 5.2 also shows that two axes of one sensor usually tend to behave similarly in regards to their noise parameters. For example, the calculated values for the LIS3MDL y- and x-axis only deviate slightly from each other, considering both the white noise and the flicker noise. Considering the white noise, the BNO055 y- and x-axes appear similar. This is, however, not the case for the flicker noise. For the LSM9DS1, the x- and y-axes appear to be similar for the flicker noise; however, they deviate from each other for the white noise. A reason for this occurring phenomenon of one axes strongly deviating from two other axes could be caused by design. While the datasheets of the considered magnetometers do not provide full detail on this [21d], [15], [17b], the datasheet of the BMX055 [13] presents a block diagram, with the z-axis being visibly separated from the x-and the y-axes. Assuming that the considered sensors might be built similarly to the BMX055, this might explain why two axes tend to be closer to each other considering the error coefficient. However, as the specific datasheets can not verify it, further research and analysis would be necessary to confirm this.

5.3 Temperature experiments

To better compare the sensors and their susceptibility to temperature changes, the calculated drift data from the first temperature experiment in Section 4.4 was sorted by their absolute values in ascending order, with the lowest value on top. The results are gathered in Table 5.3. The depicted drift value is in °/s/°C for the gyroscopes and in µT/°C for the magnetometers.

Device	Sensor	Axis	Calculated drift
BNO055	Magnetometer	x-axis	-1.8049 $\cdot 10^{-15}$
BMI088	Gyroscope	x-axis	-3.4756 $\cdot 10^{-5}$
BMI088	Gyroscope	z-axis	-6.2771 $\cdot 10^{-5}$
BMI088	Gyroscope	y-axis	6.8768 $\cdot 10^{-5}$
ICM20948	Gyroscope	z-axis	0.00010184
BNO055	Gyroscope	x-axis	0.00037438
BNO055	Gyroscope	z-axis	0.00083141
BNO055	Gyroscope	y-axis	0.0030917
LSM9DS1	Gyroscope	z-axis	-0.0084739
ICM20948	Gyroscope	x-axis	-0.015330
BNO055	Magnetometer	y-axis	0.017442
ICM20948	Gyroscope	y-axis	-0.020091
LSM9DS1	Gyroscope	y-axis	0.046638
BNO055	Magnetometer	z-axis	-0.067986
LSM9DS1	Gyroscope	x-axis	0.074197
LSM9DS1	Magnetometer	z-axis	0.12907
LSM9DS1	Magnetometer	y-axis	0.20449
LSM9DS1	Magnetometer	x-axis	-0.29430
LIS3MDL	Magnetometer	x-axis	0.35118
LIS3MDL	Magnetometer	z-axis	-0.39834
LIS3MDL	Magnetometer	y-axis	-0.49300

Table 5.3: Sensors sorted in ascending order by the calculated drift values

A general trend can not be seen in Table 5.3, as the gyroscope tends to have a lower temperature drift, while the magnetometer appears to be more influenced by the temperature.

Out of the analyzed sensors, the BMI088 appears to be the least affected by temperature changes, while the BNO055 magnetometer appears to be the magnetometer with the lowest overall drift.

This uneven distribution, especially the differences in the magnetometer drifts, can not be fully determined. A probable explanation could be magnetic fields along specific axes, which may be induced due to higher temperatures.

5.4 Simulations

While some papers, such as [KK19] use Simulink for their sensor modeling, this thesis showed the limitations of the used Simulink model. Not all possible error coefficients could be integrated into this model, which is why the imuSensor implementation was preferred. This approach showed to be more accurate in terms of calculated error coefficients calculated by the Allan Variance.

The gyroscope simulations are listed in Table 5.4 by their difference in the white noise, which has been determined to be the most dominant error source for the gyroscopes.

Device	**Axis**	**White noise difference in** $(\mathrm{rad/s})/\sqrt{\mathrm{Hz}}$
ICM20948	z-axis	0.00001036
BNO055	x-axis	0.00014248
BNO055	z-axis	0.00027083
BNO055	y-axis	0.00049813
ICM20948	y-axis	0.00054881
ICM20948	x-axis	0.00058159
LSM9DS1	z-axis	0.00068492
LSM9DS1	x-axis	0.00082112
LSM9DS1	y-axis	0.00090586
BMI088	x-axis	0.001681
BMI088	y-axis	0.0017419
BMI088	z-axis	0.0025986

Table 5.4: Gyroscope axes sorted by their white noise error coefficients difference between the simulated and recorded data in ascending order

The order of the devices in Table 5.4, as well as most of the axes is similar to the order of the absolute value of the white noise error coefficient as shown in Table 5.1. This indicates that low error coefficients can be better simulated, as the deviation between the error coefficient calculated from the recorded and the simulated data appears to be small. Equivalently, higher error coefficients appear to be worse simulated as the deviation increases.

The differences between the real and simulated error coefficients of the random walk or white noise and flicker noise of the magnetometers were also sorted in a ascending order and can be found in Table 5.5.

Device	Axis	White noise difference in µT/$\sqrt{\text{Hz}}$	Flicker noise difference in µT
LIS3MDL	y-axis	0.045007	0.068797
LSM9DS1	y-axis	0.053782	0.096668
LIS3MDL	x-axis	0.060417	0.092772
LSM9DS1	x-axis	0.070241	0.075748
LSM9DS1	z-axis	0.1264	0.048929
LIS3MDL	z-axis	0.14311	0.12161
BNO055	z-axis	0.16833	0.0096697
BNO055	y-axis	0.32124	0.025564
BNO055	x-axis	0.35046	0.00022026

Table 5.5: Magnetometer axes sorted by their white noise and flicker noise coefficients differences between the simulated and recorded data in ascending order

This list is again almost entirely identical to the Table 5.2, which indicates that lower error coefficients can be simulated more accurately.

5.5 Calibration

As described in Section 3.5.3, a direct comparison between the used calibration methods was not possible due to the different underlying sensor models.

Section 4.6.1 showed that for a fixed scale matrix, the magcal algorithm appears to estimate the input bias closely. The same section also shows that the TWOSTEP can estimate the biases, even though its results deviate more from the given values. This algorithm does, however, correctly calculate the scale matrices throughout Section 4.6.1. This cannot be said for the magcal implementation, which calculates consistent values that deviate from the given scale matrix.

For a fixed bias, instead of a fixed scale matrix, it could be seen in Section 4.6.2 that the TWOSTEP deviates more from the given biases as well as the scale matrix. The scale matrices calculated by magcal also deviate from the given parameters. This, however, cannot be used for further analysis, as the scale matrices calculated by magcal showed a deviation for the whole Section 4.6.

A possible explanation for these deviations visible for the magcal method may be the underlying mathematical model as well as a different assumption on the magnetic field strength, as described in Section 3.5. This, however, does not explain why the TWOSTEP calculated deviating values in Subsection 4.6.1. The input scale matrix may

cause this deviation. This is, however, unlikely, as the bias calculated by the magcal method for the same input parameters appeared to be correct.

A final reason for this deviation by the TWOSTEP algorithm could not be found.

6 Conclusion

The above experiments show that the BNO055 gyroscope appears to be the most stable out of the considered sensors regarding the white noise, while the LSM9DS1 magnetometer seems to be the most stable both random walk or white noise and flicker noise. Next, the temperature drifts are compared agains each other. Considering all three axes, the most stable magnetometer appears to be the BNO055, while the most stable gyroscope is the BMI088. However, the BNO055 gyroscope is assumed to be the best simulated due to its low differences between the real and simulated error coefficients. Out of the magnetometers, the LSM9DS1 shows this behavior. The summarized findings are depicted in Table 6.1.

	Lowest Error coefficients	**Lowest temperature drift**	**Accurate Simulation**
Gyroscope	BNO055	BMI088	BNO055
Magnetometer	LSM9DS1	BNO055	LSM9DS1

Table 6.1: Summarized experiment results

Out of the analyzed sensors, the BNO055 is the best option for the ADCS of the MOVE-III CubeSat.

While this thesis lists numerous conducted experiments, further work is recommended to further the progress of the attitude determination.

The conducted temperature experiments mainly covered temperatures above room temperatures, and lower temperatures could only once be achieved in the TVAC for the BNO055. These experiments should be repeated to cement the decision of the BNO055 as the IMU for the ADCS. The internal temperature sensor can also be read out for this new iteration instead of an external temperature sensor.

Furthermore, the simulations implemented and characterized throughout this thesis have not been thus far integrated into the existing simulation of MOVE-II or newer simulations of MOVE-III. This integration should be conducted to test the sensor in a simulated environment further. Once integrated, the new sensor model can be used to evaluate used algorithms.

In case of available sun vector measurements from the sun sensors of the ADCS, attitude

determination can and should be performed alongside the BNO055 measurements to determine the overall accuracy of the sensor measurement as well as the subsequent attitude determination.

A final calibration algorithm for the magnetometer should be chosen so that the error of the BNO055 magnetometer can be reduced. The analysis performed in this thesis regarding magcal and the TWOSTEP algorithm suggests more focused research on available calibration methods and the following comparison.

7 Appendix

7.1 Digital appendix

The digital appendix of this thesis can be found under https://gitlab.lrz.de/ga62yoy/ba

7.2 Further Research in the Context of this Thesis

7.2.1 Balloon Flight

Practical Background

In order to integrate and test the whole system, the MOVE team conducts high-altitude balloon flights to reach a near-space environment. On the 16th of October 2021, the MOVE team conducted such a flight. The integrated system can be seen in Figure 7.1[1].

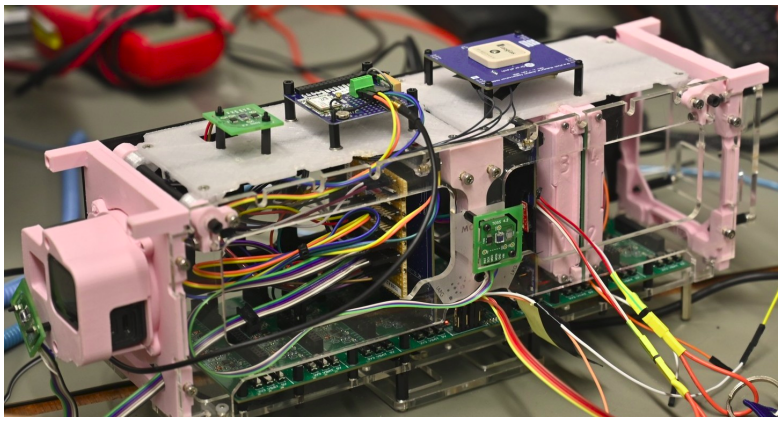

Figure 7.1: Integrated System for the Balloon Flight on the 16th of October 2021

The ADCS board hosted the BNO055 and recorded around 90 minutes of flight data before a power outage of the system caused the board to shut down. Additionally, the ADCS also hosted the BME680 sensor [21a] and six in-house developed sun sensors. The board can be seen integrated in Figure 7.1 as the closest board to the viewer.

[1]Picture provided by Zeyu Zhu

Besides the sensors integrated on the ADCS board, an onboard camera was also integrated, as well as a UART-Logger [Sei] for logging all recorded data.

Evaluation

This section visualizes the data recorded by the BNO055 gyroscope and magnetometer during the high-altitude balloon flight on th 16th of October 2021. This visualization can be found in Figures 7.2 and 7.3. The concrete setup can be seen in Section 7.2.1.

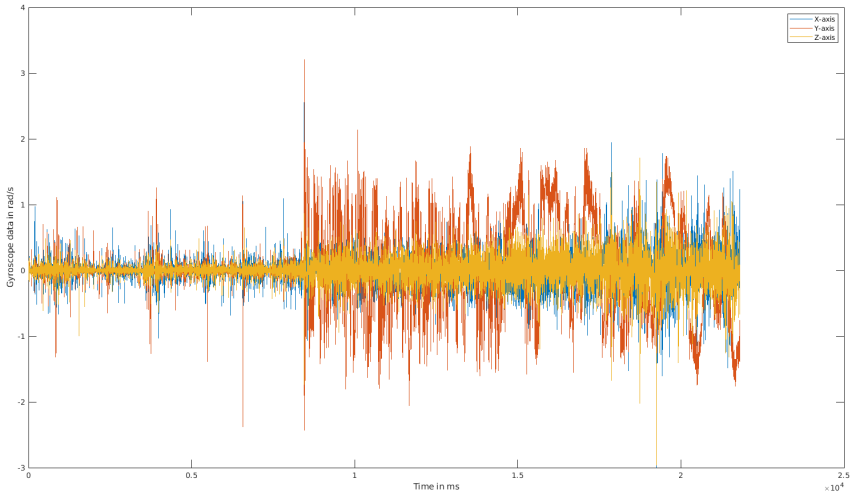

Figure 7.2: Recorded flight data from the BNO055 gyroscope

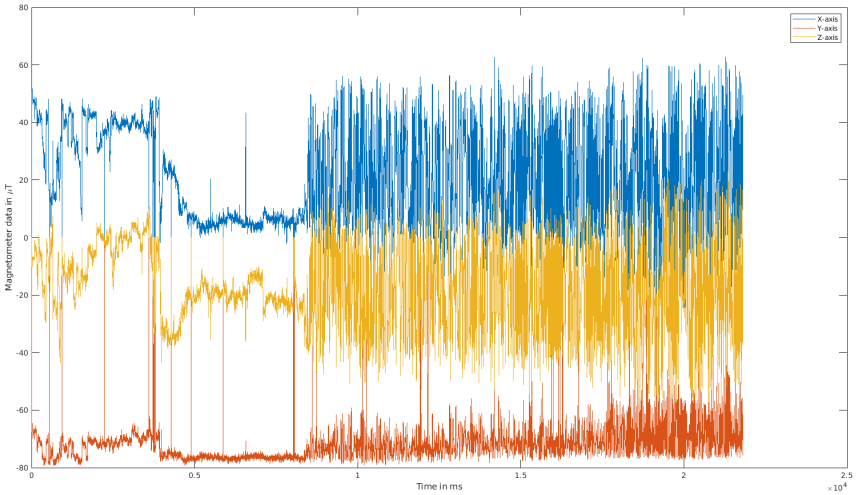

Figure 7.3: Recorded flight data from the BNO055 magnetometer

At around 0 ms to 1000 ms and 1000 ms to 2000 ms, a stabilization of the magnetometer data in Figure 7.3 is observed. In between these two time periods, both the magnetometer and the gyroscope measurements in Figure 7.2 indicate a rotation of the whole system. At around 2000*ms*, the system seems to spin. Both magnetometer and gyroscope indicate this deduction as their respective measurements are heavily oscillating from this point in time. Additionally, the onboard camera verified that the system was spinning at an almost constant rate.

A more in-depth attitude determination has not been performed yet on these measurements. This missing determination is because standard attitude determination algorithms, such as the TRIAD algorithm, require a secondary vector, such as the sun position [MC14]. While there were six integrated sun sensors on the balloon flight in October 2021, they did not calculate a sun position vector, and instead, they measured the light input through photodiodes. The design of the ADCS also plans on using different sun sensors than the ones flown on the balloon, which is why no further resources have been allocated to calculate the sun position vector from the sun sensor measurements recorded during the flight.

List of Figures

List of Tables

Bibliography

[13] *BMX 055 Small, versatile 9-axis sensor module*. BST-BMX055-DS000-01. Rev. 1.0. BOSCH. Oct. 2013.

[15] *LSM9DS1 iNEMO inertial module: 3D accelerometer, 3D gyroscope, 3D magnetometer*. 025715. Rev. 3. STMicroelectronics. Mar. 2015.

[17a] *ICM20948 World's Lowest Power 9-Axis MEMS MotionTracking™ Device*. DS-000189. Rev. 1.3. TDK InvenSense. Feb. 2017.

[17b] *LIS3MDL Digital output magnetic sensor: ultra-low-power, high-performance 3-axis magnetometer*. 024204. Rev. 6. STMicroelectronics. May 2017.

[20a] *STM32 Nucleo-144 boards (MB1137)*. UM1974. Rev. 8. STMicorelectronics. Aug. 2020.

[20b] *STM32L4R5xx STM32L4R7xx STM32L4R9xx*. DS12023. Rev. 5. STMicorelectronics. Jan. 2020.

[21a] *BME680 Low poer gas, pressure, temperature & humidity sensor*. BST-BME680-DS001-17. Rev. 1.7. BOSCH. Dec. 2021.

[21b] *BMG250 Low noise, low power triaxial gyroscope*. BST-BMG250-DS000-05. Rev. 1.5. BOSCH. Oct. 2021.

[21c] *BMI088 6-axis Motion Tracking for High-performance Applications*. BST-BMI088-DS000-17. Rev. 1.7. BOSCH. Nov. 2021.

[21d] *BNO055 Intelligent 9-axis absolute orientation sensor*. BST-BNO055-DS000-18. Rev. 1.8. BOSCH. Oct. 2021.

[21e] *MTi-7*. accessed on 09.01.2022. X-sens. June 2021.

[AS03] R. Alonso and M. Shuster. "Complete Linear Attitude-Independent Magnetometer Calibration." In: *The Journal of the Astronautical Sciences* 50 (Oct. 2003), pp. 477–490. DOI: 10.1007/BF03546249.

[Bol+12] H. Bolandi, M. Haghparast, F. Saberi, B. Vaghei, and S. Smailzadeh. "Satellite Attitude Determination and Contol." In: *Measurement and Control* 45.5 (June 2012), pp. 151–157. DOI: 10.1177/002029401204500505.

[Che11] S. Chen. "The Space Debris Problem." In: *Asian Perspective* 35.4 (2011), pp. 537–558. DOI: 10.1353/apr.2011.0023.

[Con] U. of Concerned Scientists. *UCS Satellite Database*. URL: https://www.ucsusa.org/resources/satellite-database. (accessed: 30.01.2022).

[Cra] J. L. Crassidis. *Index of / johnc/space_book/chapter6*. URL: http://www.acsu.buffalo.edu/~johnc/space%5C_book/chapter6/. (accessed: 15.01.2022).

[Dir] eoPortal Directory. *ARMADILLO (Attitude Related Maneuvers And Debris Instrument in Low (L) Orbit)*. URL: https://directory.eoportal.org/web/eoportal/satellite-missions/a/armadillo. (accessed: 30.01.2022).

[Doc20] S. Documentation. *Simulation and Model-Based Design*. 2020.

[Dou13] B. Douglas. *A simple MEMS gyro model using MATLAB / Simulink*. 2013. (accessed: 08.02.2022).

[Dra+14] K. Draganová, F. Kmec, J. Blažek, D. Praslička, J. Hudák, and M. Laššák. "Noise Analysis of Magnetic Sensors Using Allan Variance." In: *Acta Physica Polonica A* 126.1 (July 2014), pp. 394–395. DOI: 10.12693/aphyspola.126.394.

[EHN08] N. El-Sheimy, H. Hou, and X. Niu. "Analysis and Modeling of Inertial Sensors Using Allan Variance." In: *IEEE Transactions on Instrumentation and Measurement* 57.1 (Jan. 2008), pp. 140–149. DOI: 10.1109/tim.2007.908635.

[EMC] EMCORE. *Glossary of inertial sensing terms*. URL: https://gladiatortechnologies.com/glossary/. (accessed: 10.02.2022).

[GKL12] K. Gamble, H. Kjellberg, and G. Lightsey. "In-Situ Sub-Millimeter Space Debris Detection Using CubeSats." In: vol. 144. Feb. 2012.

[Hei+09] A. Heidecker, M. Schlotterer, S. Theil, and M. Hallmann. "ATTITUDE DETERMINATION AND CONTROL OF THE ASTEROIDFINDER MISSION." In: Oct. 2009.

[HL06] B. Huitema and S. Laraway. "Autocorrelation." In: Aug. 2006.

[KK19] E. Kapeel and A. Kamel. "Modeling and Simulation of Low Cost MEMS Gyroscope Using MATLAB (SIMULINK) for UAV Autopilot Design." In: Aug. 2019.

[Lam+03] Q. Lam, N. Stamatakos, C. Woodruff, and S. Ashton. "Gyro Modeling and Estimation of Its Random Noise Sources." In: *AIAA Guidance, Navigation, and Control Conference and Exhibit*. American Institute of Aeronautics and Astronautics, June 2003. DOI: 10.2514/6.2003-5562.

[Mata] MathWorks. *MATLAB&SIMULINK*. URL: https://de.mathworks.com/help/pdf%5C_doc/simulink/simulink%5C_ref.pdf. (accessed: 07.02.2022).

[Matb] Matlab. *allanvar*. URL: https://de.mathworks.com/help/nav/ref/allanvar.html%5C#mw%5C_47037cad-f666-4a62-a2e1-4a15ef4dd70d. (accessed: 09.01.2022).

[Matc] Matlab. *dsp.ColoredNoise*. URL: https://de.mathworks.com/help/dsp/ref/dsp.colorednoise-system-object.html. (accessed: 12.01.2022).

[Matd] Matlab. *imuSensor*. URL: https://de.mathworks.com/help/nav/ref/imusensor-system-object.html. (accessed: 12.01.2022).

[Mate] Matlab. *Inertial Sensor Noise Analysis Using Allan Variance*. URL: https://de.mathworks.com/help/fusion/ug/inertial-sensor-noise-analysis-using-allan-variance.html. (accessed: 09.01.2022).

[Matf] Matlab. *magcal*. URL: https://de.mathworks.com/help/nav/ref/magcal.html. (accessed: 08.01.2022).

[Matg] Matlab. *Magnetometer Calibration*. URL: https://de.mathworks.com/help/fusion/ug/magnetometer-calibration.html. (accessed: 16.01.2022).

[Math] Matlab. *polyfit*. URL: https://de.mathworks.com/help/matlab/ref/polyfit.html. (accessed: 24.01.2022).

[MAT21] MATLAB. *R2021a*. Natick, Massachusetts: The MathWorks Inc., 2021.

[MC14] L. Markley and J. Crassidis. *Fundamentals of Spacecraft Attitude Determination and Control*. Jan. 2014. ISBN: ISBN: 978-1-4939-0802-8. DOI: 10.1007/978-1-4939-0802-8.

[MD09] S. Montenegro and F. Dannemann. "RODOS - real time kernel design for dependability." In: *DASIA 2009 - DAta Systems in Aerospace* 669 (2009), p. 66.

[Mes+17] D. Messmann, T. Grübler, F. Coelho, T. Ohlenforst, J. Bruegge, F. Mauracher, M. Doetterl, S. Plamauer, P. Schnierle, T. Kale, M. Seifert, A. Fuhrmann, E. Karagiannis, A. Ulanowski, T. Lausenhammer, A. Meraner, and M. Langer. "Advances in the Development of the Attitude Determination and Control System of the CubeSat MOVE-II." In: July 2017.

[Mih+16] C. Mihai, A. Nilgesz, F. Birouas, and R. Tarca. "Hard iron distortion compensation for 3 axis magnetometer." In: *Recent Innovations in Mechatronics* 3 (Sept. 2016). DOI: 10.17667/riim.2016.1-2/5..

[NAR08] C. NARANJO. "Analysis and Modeling of MEMS based Inertial Sensors." In: (Jan. 2008).

[NASa] NASA. *Space Debris and Human Spacecraft*. URL: https://www.nasa.gov/mission%5C_pages/station/news/orbital%5C_debris.html. (accessed: 30.01.2022).

[NASb] NASA. *Sputnik and the Dawn of the Space Age*. URL: https://history.nasa.gov/sputnik.html. (accessed: 30.01.2022).

[PNS21] K. Papafotis, D. Nikitas, and P. P. Sotiriadis. "Magnetic Field Sensors' Calibration: Algorithms' Overview and Comparison." In: *Sensors* 21.16 (Aug. 2021), p. 5288. DOI: 10.3390/s21165288.

[Qui+12] A. G. Quinchia, C. Ferrer, G. Falco, E. Falletti, and F. Dovis. "Analysis and modelling of MEMS inertial measurement unit." In: *2012 International Conference on Localization and GNSS*. IEEE, June 2012. DOI: 10.1109/icl-gnss.2012.6253129.

[Qui+13] A. Quinchia, G. Falco, E. Falletti, F. Dovis, and C. Ferrer. "A Comparison between Different Error Modeling of MEMS Applied to GPS/INS Integrated Systems." In: *Sensors* 13.8 (July 2013), pp. 9549–9588. DOI: 10.3390/s130809549.

[Rüc+19] S. Rückerl, D. Messmann, N. Appel, J. Kiesbye, F. Schummer, M. Faehling, L. Krempel, T. Kale, A. Lill, G. J. Reina Kiperman, P. Schnierle, S. Würl, M. Langer, and M. Lülf. "First Flight Results of the MOVE-II Satellite." In: Aug. 2019.

[Rüc+21] S. Rückerl, M. Ukkola, S. Würl, and M. Faehling. "Distributed Computing for Modular & Reliable Nanosatellites." In: *2021 IEEE Aerospace Conference (50100)* (2021), pp. 1–10.

[Sei] N. Seidle. *Datasheet*. URL: https://github.com/sparkfun/OpenLog/wiki/Datasheet. (accessed: 08.02.2022).

[Tec] G. Technologies. *DEFINITIONS*. URL: https://emcore.com/glossary-inertial-sensing-terms/. (accessed: 10.02.2022).

[Val21] S. Valencia. "Analyses of the Russian antisatellite ASAT missile test on Kosmos-1408 and its impact on space sustainability." In: (Nov. 2021).

[Vec] Vectornav. *3.1 IMU SPECIFICATIONS*. URL: https://www.vectornav.com/resources/inertial-navigation-primer/specifications--and--error-budgets/specs-imuspecs. (accessed: 07.01.2022).

[Vil+19] T. Villela, C. A. Costa, A. M. Brandão, F. T. Bueno, and R. Leonardi. "Towards the Thousandth CubeSat: A Statistical Overview." In: *International Journal of Aerospace Engineering* 2019 (Jan. 2019), pp. 1–13. DOI: 10.1155/2019/5063145.

[WZD21] X. Wu, C. Zhang, and W. Du. "An Analysis on the Crisis of "Chips shortage" in Automobile Industry ——Based on the Double Influence of COVID-19 and Trade Friction." In: *Journal of Physics: Conference Series* 1971 (July 2021), p. 012100. DOI: 10.1088/1742-6596/1971/1/012100.